Studying Short-Range Correlations with the $^{12}\mathrm{C}(e, e'pn)$ Reaction

A dissertation submitted

to Kent State University in partial

fulfillment of the requirements for the

degree of Doctor of Philosophy

by

Ramesh Raj Subedi

December, 2007

Dissertation written by

Ramesh Raj Subedi

B.Sc., Tribhuvan University, 1988

M.Sc., Tribhuvan University, 1994

Ph.D., Kent State University, 2007

Approved by

Dr. John W. Watson ,	Co-chair, Doctoral Dissertation Committee
Dr. Douglas W. Higinbotham ,	Co-chair, Doctoral Dissertation Committee
Dr. Bryon D. Anderson,	Member, Doctoral Dissertation Committee
Dr. George Fai,	Member, Doctoral Dissertation Committee
Dr. Christopher J. Woolverton,	Member, Doctoral Dissertation Committee

Accepted by

Dr. Bryon D. Anderson,	Chair, Department of Physics
Dr. Jerry Feezel,	Dean, College of Arts and Sciences

Table of Contents

List of Figures

List of Tables

Acknowledgement

This dissertation would not have been possible without help from various people. First and foremost, I wish to express my deep gratitude to my advisors John W. Watson and Douglas W. Higinbotham for giving me inspiration and guidance during my research work. They are also thankful for investing a lot of time and energy in my education. I would also like to thank other members of my dissertation committee: Bryon Anderson, George Fai, and Christopher Woolverton for their valuable comments on this dissertation.

I would like to thank John for supporting me financially, giving me a unique opportunity by sending me to Jefferson Laboratory and allowing me to stay there throughout my research, giving me a great deal of freedom in my work but never lacking when help was needed. Whenever he came to Jefferson Laboratory, he used to say, "You are making a good progress; I am happy with that." That used to be a great compliment and boost to my confidence. I am also grateful to him for carefully editing my horribly written dissertation and turning it into a readable document.

I respect Doug's superb ability to supervise students by always encouraging them, being available to them, and taking care of them like a guardian. No matter how silly you are, he always used to say, "Don't worry; you will know it eventually." Well-versed in accelerator and Hall A equipment, he is a source of ideas in designing and instrumenting experiments, and extracting the physics. I learned a lot from you; thank you Doug.

I am grateful to Shalev Gilad, who always had well thought and balanced comments, for driving the physics results to a meaningful conclusion. Thanks also to Eli Piasetzky, who always has a hardworking nature- "Do it now, don't wait until tomorrow" - has been the leading driving force for the whole analysis, pushing us to extract the main physics results as quickly as possible.

I had a wonderful experience working with my fellow graduate students on this experiment: Peter Monaghan and Ran Shneor. Your help in many aspects, including data analysis, has been unabated; Peter used to be my next door neighbour whom I could ask for help that I needed, including editing my English in numerous documents. Thank you both of you.

It was Olivier Gayou who inspired and encouraged me to learn computer programming and always believed in my work. Thank you Olivier. Robert Feuerbach and Steve Wood were always ready to help me in computer programming and used to be my resource person for troubleshoooting any computer hardware/software problems that I used to have. Their suggestions on physics analysis were excellent. Thank you both of you.

Several other people at Jefferson Laboratory and abroad with whom I worked closely, spent significant time discussing various issues, and whose help in computer programming, electronics hardware, and detector assembling was instrumental in my learning are: Ole Hansen, Ru Igarashi, Eddy Jans, Vahe Mamyan, Kathy McCormick, Bob Michaels, Bryan Moffit, Tigran Navasardyan, Yi Qiang, Bodo Reitz, Brad Sawatzky, Albert Shahinyan, Paul Ulmer, Larry Weinstein, and Bogdan Wojtsekhowski. I thank you all.

A sincere thanks goes to Hall A engineering staff (Paul, Al, Joyce, Susan, and Ravi) for their support while preparing the experiment, accelerater people for providing a high quality beam, Hall A technical staff (Ed, Jack, Mark, Gary, Heidi, Scott, and Todd) for their support during the experiment running time, Hall A staff scientists (Jian-Ping Chen, Eugene Chudakov, Javier Gomez, Ole Hansen, Douglas Higinbotham, Kees De Jager, John LeRose, Bob Michaels, Sirish Nanda, Arun Saha, and Bogdan Wojtsekhowski) and the Hall A collaboration for the help they provided various ways and, in particular, taking shifts during the data taking period of the experiment.

Back at Kent State, I am grateful to the Physics Department faculty (Bryon Anderson, George Fai, Jim Gleeson, Satyendra Kumar, Michael Lee, Mark Manley, Elizabeth Mann, Makis Petratos, Khandker Quader, and John Watson) for giving me a world class education, to the staff for providing sufficient administrative support, and my fellow graduate students for their valuable friendship. Thank you Kim, Cindy and Loretta by helping me various ways and, particularly, answering my numerous emails without delay.

I wish to thank my family, specially my mother, for raising me and showing ways to get to this point of my life. Finally, I wish to thank my children (Anu and Soniya) for their patience throughout this work, and my loving wife Nirmala for her infinite selfless support.

August 17, 2007.

Chapter 1

Introduction

Nuclei are made of protons and neutrons, called collectively "nucleons"; the standard notation is p, n, and N, respectively. Electron scattering off a single particle predominately exchanges a single virtual photon. The particle can be a whole nucleus, a group of nucleons, one nucleon, or even a single quark, depending upon the amount of energy and momentum transferred in the process. At sufficiently low energy and momentum transfer, scattering occurs leaving the whole nucleus intact and in its ground state. This is called elastic scattering. Elastic scattering is considered to be a surface reaction and no detailed information is obtained related to the interior of the nucleus.

As the energy and momentum transfer increase, the constituent nucleons are resolved and the scattering can occur elastically from a nucleon. This is called quasi-elastic (or quasi-free) scattering. The cross-sectional peak is smeared due to the Fermi motion of nucleons. Further increases in the energy and momentum transfer allow for the excitation of nucleons to various resonances. For example, a proton, having interacted with the scattered electron, becomes a Δ particle which then decays into a pion and a baryon. For high enough energy and momentum transfer, the interaction probes an individual quark. This is deep-inelastic scattering.

Electron scattering is a well established process and a powerful tool for studying nuclear structure. The Thomas Jefferson National Accelerator Facility (Jefferson Laboratory) is an ideal place for electron-scatterring studies through coincidence experiments, due to the availability of a continuous-wave electron beam.

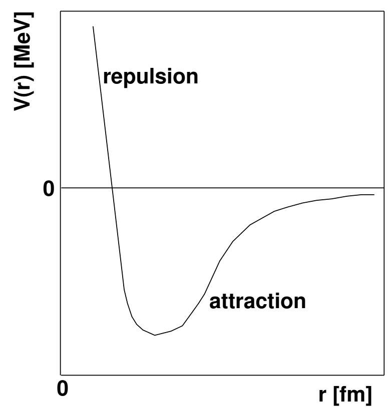

Fig. 1.1: A qualitative sketch of the NN-interaction potential (V) versus the NN separation distance (r).

The nucleon-nucleon (NN) interaction, an overview of the experiment, and related previous work for the E01-015 experiment will be presented in this chapter. The theoretical background is described in Chapter 2. Chapter 3 contains the detailed description of the experimental setup, including description of various apparatuses used in this experiment. Chapter 4 contains the discussion of how the neutron-detection efficiency was obtained. Chapter 5 and Chapter 6 contain the description of the data analysis, with Chapter 6 focusing on events with detected neutrons. Finally, Chapter 7 contains results, discussion, and conclusions.

1.1 The Nucleon-Nucleon Interaction

The important features of the NN-interaction [2] are attraction at large distance and the strong repulsion at short distance. These features are indicated qualitatively [3] in Fig. 1.1. When the inter-nucleon distance is less than about 1 fm (10^{-15} m), the NN-interaction is repulsive, while at distances larger than about 1 fm, the interaction becomes attractive.

1.1.1 The Shell Model in General

The independent-particle shell model[1] assumes that each nucleon moves independently from the others in the attractive mean field created by all the other nucleons. Neutrons and protons have independently-defined shell-model states. Even though the shell model is a phenomenological model, it not only gives a good description of nuclear ground states, but also predicts the sequence, quantum numbers, and relative positions of excited states.

Considering the nucleus of A nucleons as a non-relativistic quantum-mechanical system with two-body interactions between the nucleons, the Hamiltonian (H) of the system is given in terms of kinetic energy (T) and the iteraction potential (v) as

$$H = T + \sum_{i<j=1}^{A} v(i,j). \tag{1.1}$$

Introducing a one-body potential $V(i)$, the mean field, in which the ith nucleon is moving, we can rewrite the above equation as

$$H = T + \sum_{i=1}^{A} V(i) + \sum_{i<j=1}^{A} v(i,j) - \sum_{i=1}^{A} V(i). \tag{1.2}$$

With the notation of the shell-model Hamiltonian as H_{sm} and the residual interaction as V_{res}, we get

$$H = H_{sm} + V_{res} \tag{1.3}$$

[1]There are many nuclear models that use the shell structure of nuclear states. We donote the "independent particle shell model" as simply the "shell model" henceforth.

where

$$H_{sm} = T + \sum_{i=1}^{A} V(i) \tag{1.4}$$

and

$$V_{res} = \sum_{i<j=1}^{A} v(i,j) - \sum_{i=1}^{A} V(i) \tag{1.5}$$

The main assumption of the shell model is the neglect of the residual interaction.

1.1.2 The Shell Model for ^{12}C

Figure 1.2 shows the nucleon states for the ^{12}C nucleus in its ground state. There are two shell-model states in ^{12}C in its ground state: 1s and 1p; 1s is completely filled while 1p is partially filled. The subshell $1p_{\frac{1}{2}}$ is empty and the subshell $1p_{\frac{3}{2}}$ is filled. In this scheme, the possible shell-model configurations of the NN-pairs in the ^{12}C nucleus can be $(1p_{3/2})^2$, $(1p_{3/2}, 1s_{1/2})$, and $(1s_{1/2})^2$.

1.1.3 Beyond the Shell Model

The research described in this dissertation was a quest to observe physics beyond the shell model. The primary assumption of the shell model is that the nucleons undergo *independent* motion in the nuclear mean field which is a reflection of the attractive part of the NN interaction. What we were seeking in this project was to observe and quantify, where possible, *correlated* motion. In particular, we were looking for pairs of nucleon with roughly equal and opposite ("back-to-back") momenta, due to interaction through the short-range repulsive part of the NN interaction. These short-range correlated pairs are called short-range correlations (SRCs).

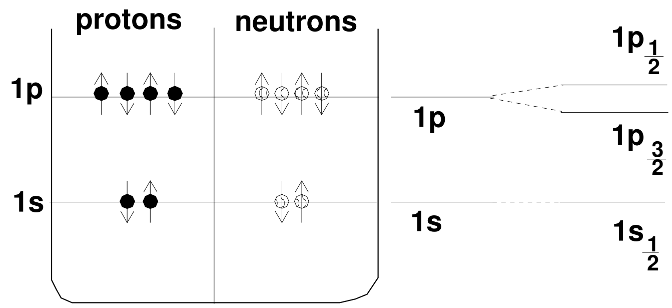

Fig. 1.2: A generic shell-model diagram for the ^{12}C nucleus. Neutrons and protons have independently-defined shell-model states. There are two shell-model states in ^{12}C in its ground state: 1s and 1p; 1s is completely filled while 1p is partially filled. The subshell $1p_{\frac{1}{2}}$ is empty and the subshell $1p_{\frac{3}{2}}$ is filled.

1.2 Experiment Overview

The present investigation was performed at the Thomas Jefferson National Accelrator Facility in Newport News, VA, in experimental Hall A. The experiment, number E01-015, was a study of short-range correlations between two nucleons in carbon nuclei using the $^{12}\mathrm{C}(e, e'pn)$ reaction. Fig. 1.3 shows a reaction diagram for such a reaction. The short-range correlations that we are investigating are initial-state correlations (i.e. the short-range correlations in the ground state of the target nucleus). When strongly repulsive interactions between two nucleons at small inter-nucleon distances occur, they introduce initial-state correlations and these correlations cause a promotion of nucleons to states above the Fermi surface by generating high[2] nucleon momenta.

Before a virtual photon couples to the n-p, p-p, or n-n pair, the partner nucleons of the pair have momenta roughly equal in size but opposite in direction. As soon as the virtual photon couples to one of the partner nucleons of the strongly-correlated pair and removes it from the nucleus, the residual nucleus is likely to be left in a state with large excitation energy and large momentum. As a result the second nucleon, which lost its partner, is likely to be emitted with a momentum equal to its initial-state momentum. The emission of both nucleons occurs simultaneously. In this work, mainly data for n-p correlations will be discussed.

Experiment E01-015 uses a technique of electron-induced two-nucleon knockout[3] from a carbon nucleus with the goal of being sensitive to and studying short-range correlations. The remarkable feature of the electron-hadron interaction is that one can probe the hardron dynamics with a virtual photon whose energy can be tuned as desired, turning a "Q^2-knob" where Q^2 is the negative of the square of the four-momentum transfer to the target nucleon. In the present experiment Q^2 was about 2 (GeV/c)^2, which in terms of length scale (λ), was about 0.14 fm, as dictated by the relation $\lambda \sim c\hbar/Q$, assuring that we were in the proper length scale for studying short-range correlations of nucleons in a nucleus. Due to the short wavelength (high Q^2), the initial interaction must affect only a small part of the nucleus, not the whole system. This means that the emitted n-p pair must have come from within the nucleus when the constituents of the pair were extremely close, in order that both be emitted simultaneously.

---

[2]Here "high" means higher than the Fermi momentum for a nucleon in the nucleus (e.g., for a carbon nucleus the Fermi momentum for a nucleon is about 221 MeV/c) [4].

[3]In this dissertation, in the context of SRCs, the meaning of 'two-nucleon knockout' (or the knockout of the correlated pair) is the knockout of the struck proton followed by the emission of a recoiling nucleon.

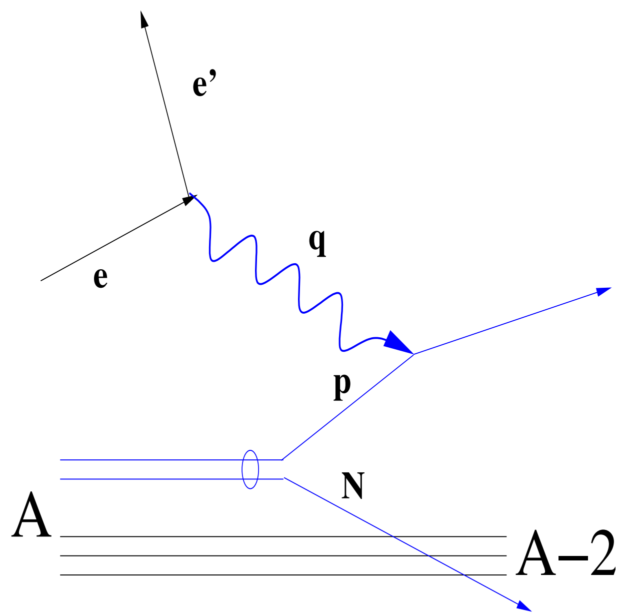

Fig. 1.3: A simple reaction diagram for nucleon knockout in the A$(e, e'pN)$ reaction. The small oval represents the interaction of a proton and a nucleon at small seperation, producing a correlated pair. The wavy line represents the virtual photon, which couples to the correlated proton.

In order to access small inter-nucleon distances for a correlated pair, both nucleons should be in a state of high relative momentum, $\vec{p}_{rel} = (\vec{p}_n - \vec{p}_m)/2$, compared to the Fermi momentum. Here $\vec{p}_m$ and $\vec{p}_n$ are the momenta of the initial-state proton, and the recoil (partner) neutron, respectively. In this definition of relative momentum, the recoil neutron momentum is approximately equal to the the relative momentum. Furthermore, assuming that the virtual photon couples to the proton of the n-p pair, the momentum of the ejected neutron and the reconstructed initial-state momentum of the proton will be approximately equal and opposite. Such a relative momentum forms the signature of NN short-range correlations. The angle between the momentum directions of these two correlated partners can be reconstructed and the value of this angle turns out to be about 180°. This is, so to speak, the back-to-back nature of the momenta of the correlated nucleons in the pair. Small deviations from equal and opposite momenta of the correlated partners

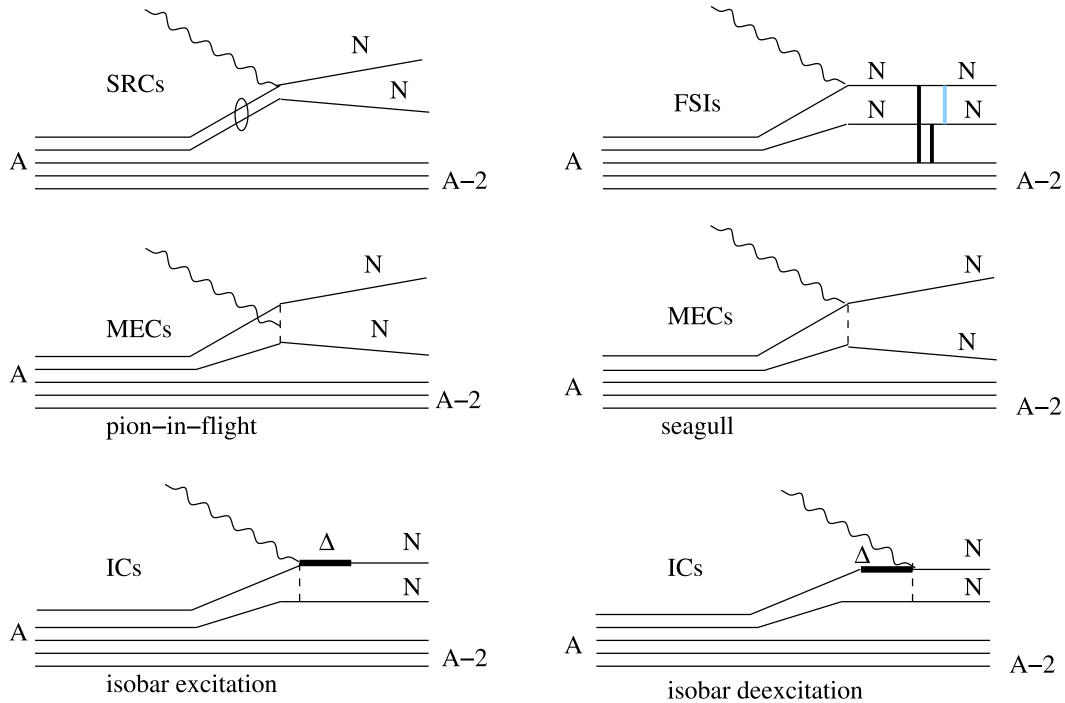

Fig. 1.4: Diagrams for SRCs and two-body processes.

are attributable to the motion of the center-of-mass of the pair within the target nucleus.

The virtual photon can couple to the carbon nucleus via different processes. It may be absorbed by one nucleon through a one-body hadronic current, or by many nucleons through many-body hadronic currents. We detect the emitted two high-momentum nucleons in the study of SRCs in this investigation. Because the virtual photon couples to only one member of the SRC pair, the SRC is a one-body process, even though it leads to the emission of two nucleons (see the top left diagram in Fig. 1.4). On the other hand, all two-body processes (see Fig. 1.4), such as meson-exchange currents (MECs), isobar currents (ICs), and final-state interactions (FSIs), lead to the emission of two high energy nucleons. Hence the SRC must compete with these two-body processes.

Though the complete elimination of MECs, ICs, and FSIs is impossible, they are expected to be suppressed at high Q^2 (Q^2 is the negative of the square of the 4-momentum transfer, see Sect. 2.1 for detail) and high Bjorken x (denoted as x_B) [5]. For this reason, the kinematics of the present experiment are chosen in such a way that it has high Q^2 (2 GeV^2/c^2) and high x_B (1.2). We choose anti-parallel kinematics to minimize FSIs between the two outgoing nucleons.

1.3 Previous Work

There have been numerous attemts to explore SRCs using either one-nucleon emission methods, or two-nucleon emission methods. The one-nucleon knockout experiments of the type A$(e, e'p)$ have recently been investigated at Jefferson lab in both Hall A [6, 7], and Hall C [8], and show strong evidence for the existence of SRCs. The Hall C result, as reported in [8] for the ^{12}C$(e, e'p)$ reaction, shows that the strength of the spectral function matches a theoretically predicted spectral function which included the contribution of SRCs.

There were also many investigations of SRCs using two-nucleon emission reactions of the type A$(e, e'pN)$ via triple-coincidence experiments, for example, at NIKHEF [9, 10, 11, 12, 13, 14], and at Jefferson Lab Hall B [15, 16, 17]. Also at Brookhaven National Laboratory (BNL), the Eva collaboration studied the ^{12}C(p, ppn) reaction [18, 19, 20] at beam momenta from 6-10 GeV/c.

The present investigation received inspiration from the experiment performed at BNL by the Eva collaboration. One of the main findings from that project [20] is shown in Fig. 1.5 for the ^{12}C(p, ppn) reaction. Shown in the figure is the cosine of angle γ between the reconstructed momentum of the struck proton and the momentum of the recoiling neutron, versus the neutron momentum p$_n$. The interesting finding is that below the Fermi momentum k_F (0.221 GeV/c for carbon [4]) the distribution

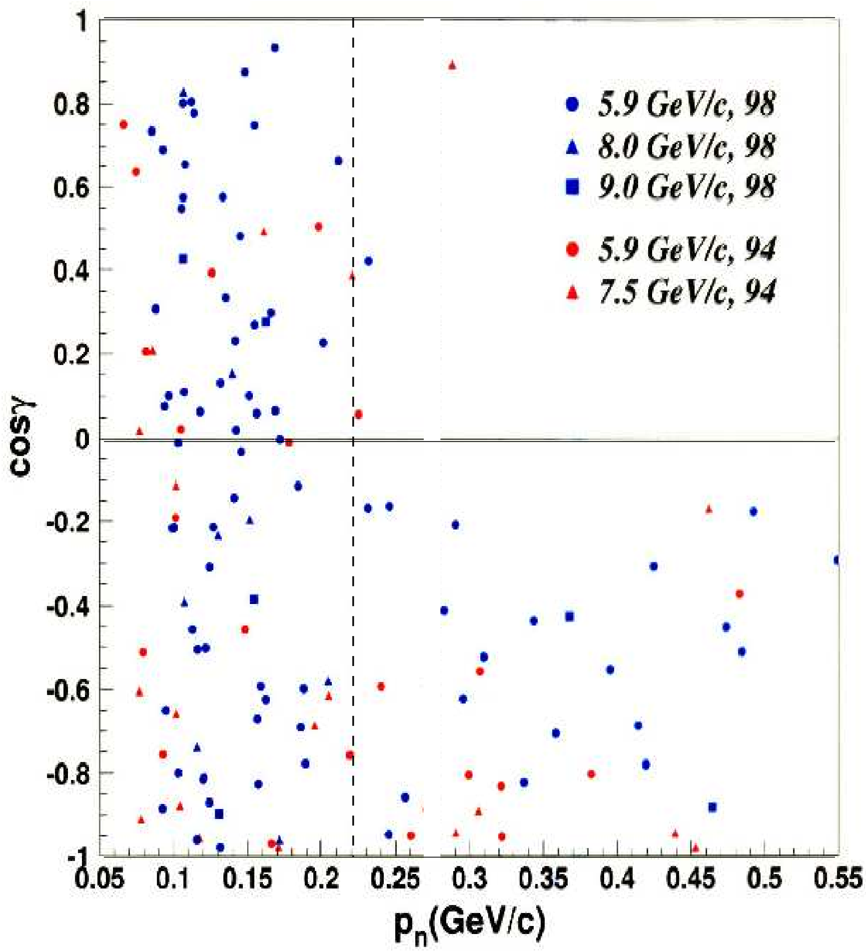

Fig. 1.5: BNL Eva collaboration result for the ^{12}C(p, ppn) reaction. Description provided in the text.

of cosγ is random while above the Fermi momentum the distribution peaks at cosγ = -1 (i.e. γ = 180°). This peaking at cosγ = -1 for $p_n > k_F$ clearly demonstrates that the struck proton and the recoil neutron have momenta in opposite directions. This back-to-back aspect of the correlated partner′s momenta is a strong signature of SRCs.

Chapter 2

Theory

A brief theoretical introduction of short-range correlations is given in this chapter by starting in the first section with the description of kinematic variables. In the later sections, a brief conceptual introduction to SRCs is given, followed by descriptions of reactions sensitive to SRCs. The mathematical formulation of SRCs, which is beyond the scope of this thesis, is quite involved and is still in a developing stage. There are many mathematical approaches, e.g., self-consistent Green's function theory, the correlated-basis-function approach [21, 22], variational technique [23], the Ghent-model [24], etc., to describe the NN-interaction in ways which ultimately lead to the same physics in the SRC regime.

2.1 Kinematic Variables

For the A$(e, e'p)$ reaction, see Fig. 2.1 for a kinematic diagram, let $q \equiv q^\mu = (\omega, \vec{q})$ denote the four-momentum transfer by the virtual photon to the target nucleon, where ω is the energy transfer and $\vec{q}$ is the three-momentum transfer. The four-momentum-transfer squared, using natural units ($\hbar = c = 1$), is given as

$$q^2 = q_\mu q^\mu = (\omega, -\vec{q}).(\omega, \vec{q}) = \omega^2 - \vec{q}^{\,2}, \tag{2.1}$$

where the incident electron of energy E has four-momentum $K = (E, \vec{K})$, the scattered electron of energy E' with scattering angle θ has four-momentum $K' =$

$(E', \vec{K}')$. These transfer quantities can also be written as

$$q = K - K', \qquad \omega = E - E', \qquad \vec{q} = \vec{K} - \vec{K}'. \tag{2.2}$$

Since we are dealing with an ultrarelativistic[1] electron, we can ignore the electron mass, m_e, compared to its energy. Hence $E = |\vec{K}|$ and $E' = |\vec{K}'|$, and as shown in reference [25]

$$q^2 = 2m_e^2 - 2\vec{K}.\vec{K}' \simeq -2\vec{K}.\vec{K}' = -4EE'sin^2(\frac{\theta}{2}). \tag{2.3}$$

The missing energy (E_m) and missing momentum ($\vec{p}_m$) of the $(A-1)$ system, using conservation of energy and three-momentum, are given as

$$E_m \;=\; \omega - T_p - T_{A-1}, \tag{2.4}$$

$$\vec{p}_m = \vec{p}_p - \vec{q}, \tag{2.5}$$

where T_p and T_{A-1} denote kinetic energy of scattered proton and recoiling $(A-1)$ nucleus, respectively; $\vec{p}_p$ is the momentum of struck proton after it was struck. It is also important to note that the magnitude and direction of $\vec{p}_m$ coincide with the momentum $(\vec{k})$ of the scattered proton before it was struck, i.e., $\vec{p}_m = \vec{k}$. (Unless otherewise noted, the quantitiy k is $|\vec{k}|$.) Implicit in this statement is the "impulse approximation", where we assume that the absorption of the virtual photon and removal of the proton does not disturb or rearrange the A-1 system on the time scale of the reaction. Another important point here is that the kinematics diagram

[1]A particle of mass m, momentum $\vec{p}$ and energy E holding a relation $E = \sqrt{\vec{p}^2 + m^2}$ is said to be relativistic if $m \sim |\vec{p}|$ and ultrarelativistic if $m \ll |\vec{p}|$.

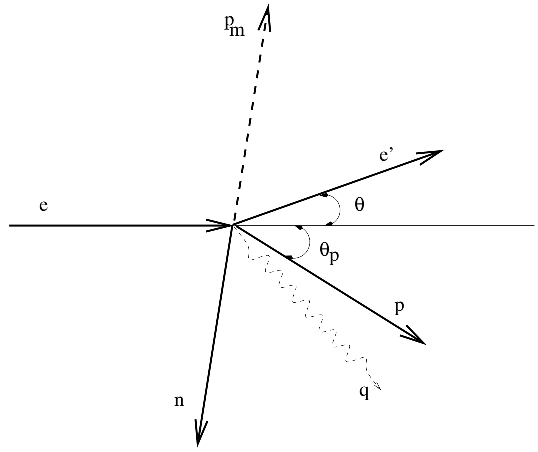

Fig. 2.1: The kinematic layout for defining variables. A reaction diagram for this figure is shown in Fig. 1.3. The wavy dashed line represents the momentum transfer $\vec{q}$ by the virtual photon. Solid lines represented by e, e', p and n represent the incident electron, scattered electron, scattered proton and the recoiling neutron respectively. The dashed line represents $\vec{p}_m$ $(= \vec{k})$.

shown in Fig. 2.1 is in almost anti-parallel kinematics[2]. Also

$$T_p = \sqrt{\vec{p}_p^2 + M_p^2} - M_p, \tag{2.6}$$

$$T_{A-1} = \sqrt{\vec{k}^2 + M_{(A-1)}^2} - M_{(A-1)}, \tag{2.7}$$

where M_p and $M_{(A-1)}$ are the mass of proton and the mass of the $(A-1)$ system respectively. Another useful variable is the Bjorken scaling variable x defined below for a nucleon (x_N) and for a nucleus (x_B) [26].

$$x_N = \frac{Q^2}{2p.q} = \frac{Q^2}{2\omega M_N}, \tag{2.8}$$

$$x_B = \frac{Q^2}{2(\frac{P}{A}).q}, \tag{2.9}$$

[2] A kinematics is said to be parallel, perpendicular or anti-parallel if the angle between the direction of momentum of the struck nucleon before it was struck and $\vec{q}$ (i.e., the angle between $\vec{k}$ and $\vec{q}$ in this case) is 0°, 90° and 180° respectively. In the present experiment they form an angle about 130°, hence it is almost anti-parallel kinematics.

where M_N is the mass of a struck nucleon, P is four-momentum of nucleus, and p is four-momentum of a nucleon. Since $q^2 \leq 0$, it is customary to define a positive quantity $Q^2 = -q^2$. Here $0 \leq x_N \leq 1$ and $0 \leq x_B \leq A$.

For the two-nucleon emission A$(e, e'pn)$ reaction the above notation also holds true. The missing energy (E_{2m}) and missing momentum ($\vec{p}_{2m}$) of $(A-2)$ system, conserving both energy and three-momentum, are given as

$$E_{2m} = \omega - T_p - T_n - T_{A-2}, \tag{2.10}$$

$$\vec{p}_{2m} = \vec{k} + \vec{p}_n = \vec{p}_{A-2}, \tag{2.11}$$

where T_n (T_p), T_{A-2}, and $\vec{p}_n$ are the kinetic energy of the recoiling neutron (proton), the kinetic energy of recoiling $(A-2)$ system, and the momentum of the recoiling neutron, respectively. E_{2m} is the excitation energy of the $(A-2)$ system and p_{2m} is its momentum. Also, p_{2m} is equal in magnitude (but opposite in direction) to the center-of-mass momentum of the correlated n-p pair for the ^{12}C$(e, e'pn)$ reaction, and ideally it is very small if not zero.

The angle γ between the vectors $\vec{p}_n$ and $\vec{p}_m$ can be obtained using

$$cos\gamma = \frac{\vec{p}_n . \vec{p}_m}{p_n p_m}. \tag{2.12}$$

Note that γ is the angle between the momenta of the correlated neutron and proton of the n-p pair in their *initial states*.

2.2 Short-Range Correlations

The shell model describes many basic features of nuclear structure. According to this model, because both neutrons and protons are spin $\hbar/2$ particles, and obey the Pauli principle, the states below the Fermi-sea are fully occupied and the states above it are totally empty. This is not what has been observed in A$(e, e'p)$ experiments, where the occupancy number below the Fermi-sea ranges approximately from 55 to 75% [27, 28, 29, 30], see Fig. 2.2 for example. The possible explanation for this shortcoming of the shell model, is the absence of nucleon-nucleon (NN) correlations in the model. The main effect of NN correlations is to deplete states below the Fermi level and make states above the Fermi level partially occupied.

Correlations in nuclei, i.e. deviation from independent-particle behaviour, are generally classified into two types: long-range correlations (LRCs) due to the long-range, attractive part of the NN interaction, and SRCs dominated by the short-range, repulsive part of the NN interaction. LRCs are generally believed to produce corrections and/or minor modifications to the shell-model picture of nuclear structure. SRCs generally lead to physics beyond the shell model.

The carbon nucleus is a quantum many-body system. In such a system interactions between constituent nucleons play an important role in binding the nucleus. The interparticle distance between nucleons inside the nucleus is of the order of the nucleon size ($\sim$1 fm). Short-range correlations are caused by hard collisions due to a strong repulsive core of the NN interactions when nucleons are at distances less than the nucleon size. In this case the strong short-range and tensor components of NN interactions induce short-range correlations into the nuclear wave function. These correlations give rise to an enhancement in the momentum distribution at higher momenta when compared to the mean field description of the nucleus. This is depicted in Fig. 2.3 where the nucleon momentum distribution, n(k), for ^{12}C is plotted as a function of momentum (k). Although the concept of SRCs was introduced in late 1950s by Gottfried [32], and intensive research was carried out in 1980s and 1990s [33, 34, 28, 35, 36, 9, 37], SRCs are still an active field of research.

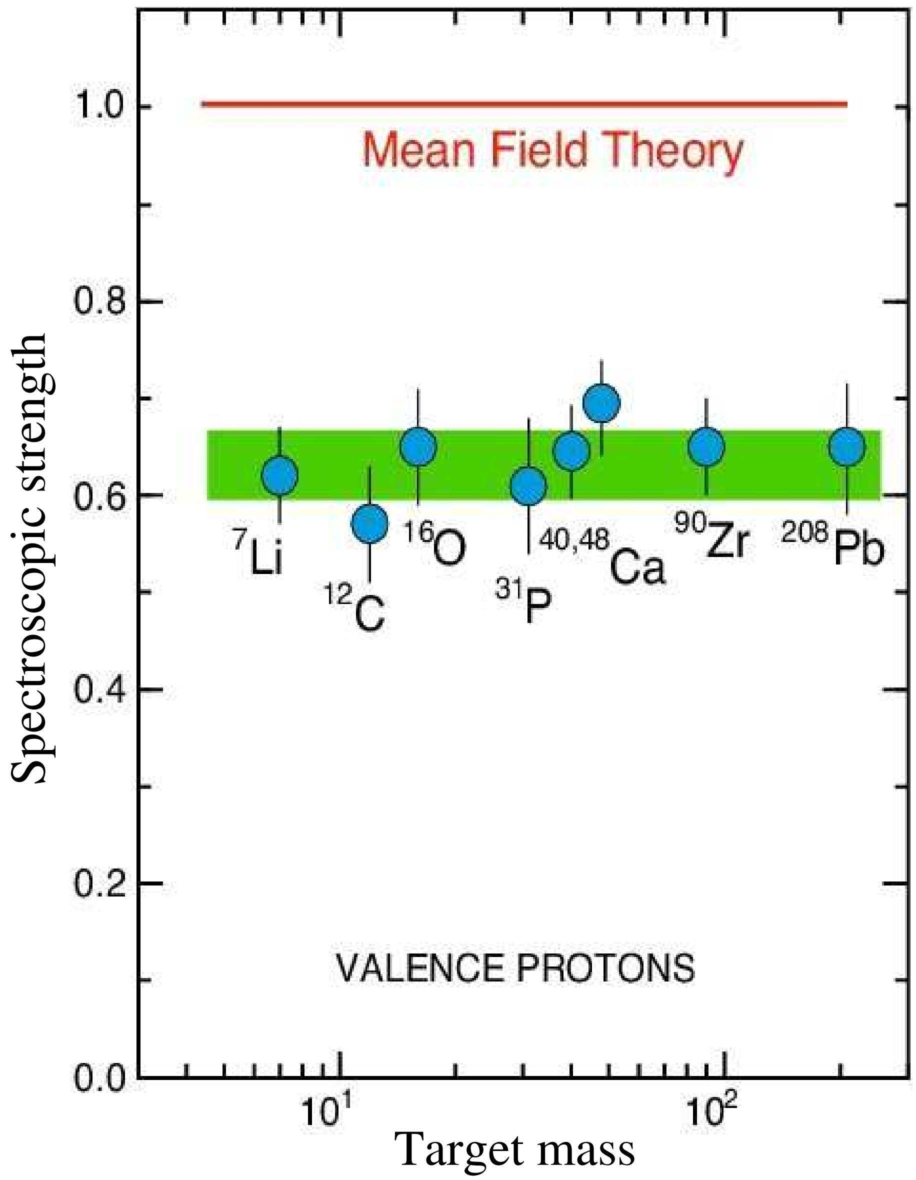

Fig. 2.2: Spectroscopic strength from the A$(e, e'p)$ reaction indicating that the shell model only accounts for 55-70% of the ground-state wave functions of various targets. The spectroscopic strength is the ratio of the experimental cross section to the theoretical cross section. This figure is reproduced from [27].

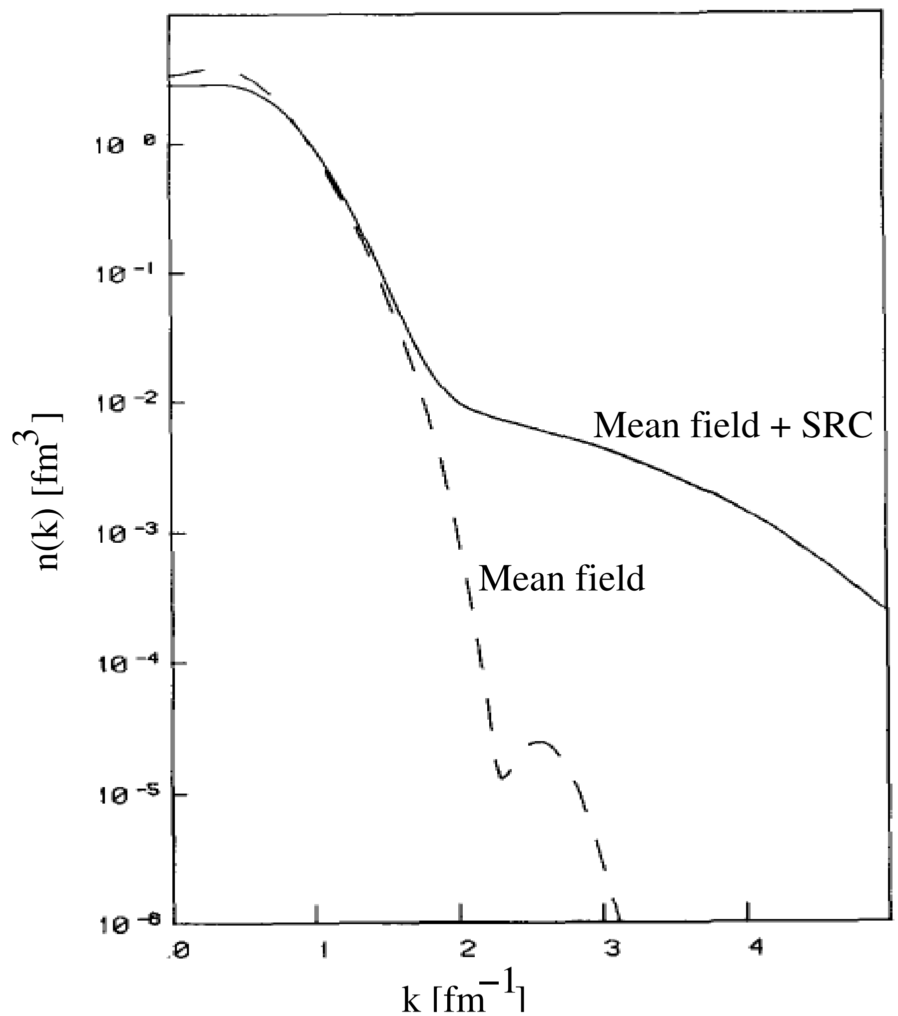

Fig. 2.3: Theoretical nucleon-momentum distributions in ^{12}C. The solid curve is the nucleon many-body momentum distribution having mean-field and SRC effects. The dashed curve has only the mean-field-approximation part. This plot is reproduced from [31].

Studying correlations manifestly reveals the structure of nuclei since the inclusion of such effects modifies the shape of the spectral function[3] and changes the spectroscopic factor. Here are a few points worth-noting.

1. The effects of short-range correlations should be independent of the nuclear system, as these correlations are very localized and not sensitive to the global structure of the whole nuclear system. For this reason the effects of short-range correlations should be similar for the nuclei ^{4}He and ^{208}Pb.

2. The momentum distribution $n(k)$ is probe-independent. Hence whatever probe we use, γ-rays, electrons, or protons, etc., we should be getting the same physics. The form of the theoretical expressions for extracting the cross-sections remain the same.

3. The long-range two-nucleon correlations arising from pion exchange, on the other hand, could be sensitive to the whole nuclear system and exhibit different results for different nuclei.

In the correlated-basis-function approach (for details see [38]) the correlated wave functions $\bar{\psi}$ are constructed using the many-body correlation operator $\widehat{\mathcal{G}}$, acting on the uncorrelated wave function ψ obtained from a mean-field potential such that

$$|\bar{\psi}>= \frac{\widehat{\mathcal{G}}|\psi>}{\sqrt{<\psi|\widehat{\mathcal{G}}^{\dagger}\widehat{\mathcal{G}}|\psi>}}. \tag{2.13}$$

The correlation operator is given as

$$\widehat{\mathcal{G}} = \widehat{\mathcal{S}}\big[\Pi_{i<j=1}^{A}\sum_{p} f^p(\vec{r}_{ij})\widehat{O}_{ij}^{p}\big], \tag{2.14}$$

[3]See Sect. 2.2.2 for definitions of the spectral function and spectroscopic factor.

where $\widehat{\mathcal{S}}$ is a symmetrization operator, f is correlation function, and $\vec{r}_{ij} = \vec{r}_i - \vec{r}_j$. Here $\vec{r}_i$ refers to the coordinates of the ejected nucleon, and $\vec{r}_j$ refers to the coordinates of any of the remaining nucleons to which the ejected nucleon is correlated. The following operators are usually retained in $\widehat{\mathcal{G}}$:

$$\widehat{O}_{ij}^{p=1} = 1, \qquad \widehat{O}_{ij}^{p=4} = (\vec{\sigma}_i.\vec{\sigma}_j)(\vec{\tau}_i.\vec{\tau}_j),$$
$$\widehat{O}_{ij}^{p=2} = \vec{\sigma}_i, \qquad \widehat{O}_{ij}^{p=5} = \widehat{S}_{ij},$$
$$\widehat{O}_{ij}^{p=3} = \vec{\tau}_i.\vec{\tau}_j, \qquad \widehat{O}_{ij}^{p=6} = \widehat{S}_{ij}(\vec{\tau}_i.\vec{\tau}_j),$$

where $\widehat{S}_{ij} = [\frac{3}{r_{ij}^2}(\vec{\sigma}_i.\vec{r}_{ij})(\vec{\sigma}_j.\vec{r}_{ij}) - \vec{\sigma}_i.\vec{\sigma}_j]$ is the tensor operator, $\vec{\sigma}_i$ are Pauli matices and $\vec{\tau}_i$ are the isospin version of the Pauli matices. It is believed [23, 24, 39] that the three components in $\widehat{\mathcal{G}}$ corresponding to $p = 1, 4$ and 6, which correspond to the central (also called Jastrow), the spin-isospin, and the tensor components, respectively, cause the biggest correlation effect, although compared to the central correlations the spin-isospin and the tensor correlations are weak. In any event, all such central, tensor or spin-isospin parts contribute their shares to the short-range correlation effect. Hence, to a good approximation, the correlation operator can be constrained to the central, tensor, and spin-isospin terms only, which is given as

$$\widehat{\mathcal{G}} = \widehat{\mathcal{S}}\big[\Pi_{i<j=1}^{A}\big(f_c(\vec{r}_{ij}) + f_{t\tau}(\vec{r}_{ij})\widehat{S}_{ij}\vec{\tau}_i.\vec{\tau}_j + f_{\sigma\tau}(\vec{r}_{ij})\widehat{S}_{ij}\vec{\sigma}_i\vec{\sigma}_j\vec{\tau}_i.\vec{\tau}_j\big)\big]. \tag{2.15}$$

The correlation function f_c accounts for the strong repulsion that the two nucleons experience when they approach each other. The two smaller correlation functions, $f_{t\tau}$ and $f_{\sigma\tau}$, account for the tensor and the spin-isospin correlations, respectively. Plots of these functions [38] are shown in Fig. 2.4, both in coordinate space and momentum space. The meaning of P_{12} in the figure is the same as k in our notation. We shall return to the roles of these three functions in Chapter 7.

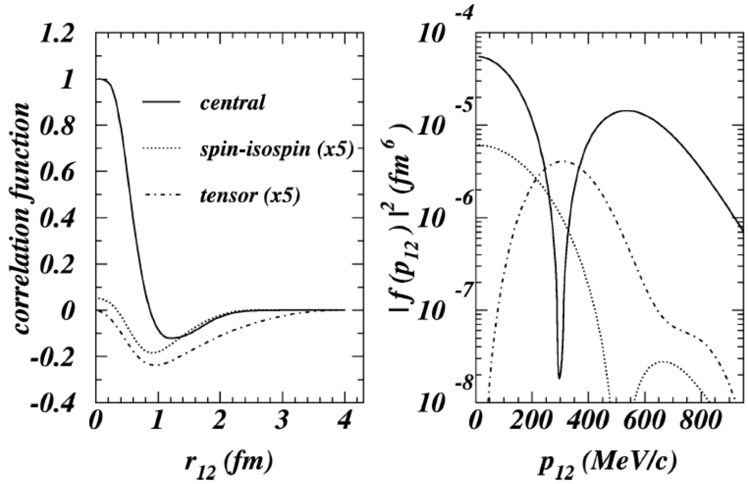

Fig. 2.4: Plots of correlation functions in coordinate space and momentum space: central (solid line), spin-isospin (dotted line) and tensor (dot-dashed line). For clarity the spin-isospin and the tensor correlation functions in coordinate space only are multiplied by a factor of five. The label P_{12} here is same as k for missing momentum in our notation in the text. This plot is reproduced from [38].

2.2.1 Short-Range Correlations from A(e, e')

The reaction A(e, e') is an inclusive one where only the scattered electron is detected. The differential scattering cross section for this reaction is given as [40, 41]

$$\begin{aligned} \frac{d^3\sigma}{d\Omega dE'} &= \sigma_M\big[(\frac{Q^2}{\vec{q}^{\,2}})^2 R_L(\vec{q}, w) \\ &+ (\frac{1}{2}(\frac{Q^2}{\vec{q}^{\,2}}) + tan^2(\frac{\theta}{2}))R_T(\vec{q}, w)\big], \end{aligned} \tag{2.16}$$

where σ_M is Mott cross section, and $R_L(\vec{q}, w)$ and $R_T(\vec{q}, w)$ are longitudinal and transverse response functions, respectively. The terms longitudinal and transverse refer to the couplings of the hadronic current to the longitudinal and transverse polarization components of the virtual photon. The Mott cross section [25] is written as

$$\sigma_M = \frac{Z^2\alpha^2(c\hbar)^2}{4E^2}\frac{cos^2\frac{1}{2}\theta}{sin^4\frac{1}{2}\theta} \tag{2.17}$$

where α is the *fine structure constant.* The integrated strength of $R_L(\vec{q}, w)$ is given by the Coulomb sum rule [41] $S_L(\vec{q})$ such that

$$S_L(\vec{q}) = \frac{1}{Z}\int_{w_{el}^{+}}^{\infty} d\omega S_L(\vec{q}, \omega), \tag{2.18}$$

with

$$S_L(\vec{q}, \omega) \equiv \frac{R_L(\vec{q}, \omega)}{|G_{Ep}(\vec{q}, \omega)|^2}, \tag{2.19}$$

where Z is the number of protons in the nucleus and G_{Ep} is the electric form factor (a function describing the charge distribution) of the proton. The lower limit ω_{el}^{+} of the integration simply excludes the elastic electron-nucleus scattering contribution. In the large momentum transfer limit (i.e., $|\vec{q}| \to \infty$), $S_L(\vec{q}) \to 1$. It is believed [42, 43] that $S_L(\vec{q})$ is sensitive to short-range correlations due to NN-interactions.

The nucleon momentum distribution (see Figs.2.3 and 2.5) has been always an interesting quantity for understanding SRCs. Inclusive electron-scattering experiments (SLAC data [44], and Jefferson Laboratory Hall C data [45]) have been performed, covering a wide $|\vec{q}|$-range appropriate for probing the nucleon momentum distribution in the nucleus with the goal of observing y-scaling. The idea of y-scaling is the following. In a quasielastic A(e, e') scattering, the nuclear response function $S(\vec{q},\ \omega)$, which generally depends on both momentum ($\vec{q}$) and energy (ω) transfers, exhibit scaling; i.e., it can be related to a function $f(y)$ of only one kinematical variable $y(\vec{q},\ \omega)$ such that $f(y) = (|\vec{q}|/M)S(\vec{q},\ \omega)$ [47]. Here y $(= \vec{k}.\vec{q}/|\vec{q}|)$ is the minimum momentum of the struck nucleon along the direction of the virtual photon and M is the nucleon mass. Knowledge of $f(y)$ can be used to obtain the

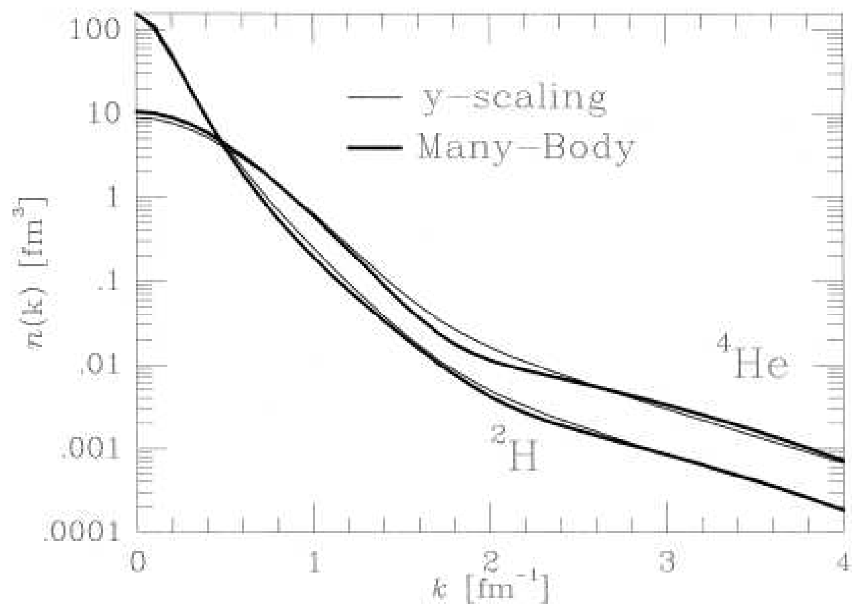

Fig. 2.5: Theoretically extracted nucleon momentum distributions for ^{2}H and ^{4}He using y-scaling, compared with that obtained using the AV14 (many-body) interaction. This figure is reproduced from [46].

necleon momentum distribution $n(k)$ by using the relation (see for detail in [46])

$$n(k) = -\frac{1}{2\pi y}\frac{df(y)}{dy}, \qquad |y| = k. \tag{2.20}$$

Fig. 2.5 depicts the use of Eqn. (2.20), and compares this result with $n(k)$ obtained from the standard AV14 interaction developed at Argonne National Laboratory.

Recently, Jefferson Laboratory Hall B data [48] using the A(e, e') reaction also show the observation of NN, and even 3N SRCs as shown in Fig. 2.6. The cross section ratios for ^{56}Fe, ^{12}C, and ^{4}He to ^{3}He as a function of x_B for Q^2 >1.4 (GeV/c)^2 are plotted in the figure. The dashed lines show the scaling regions, and as discussed in [48], this scaling may be sensitive to NN and 3N SRCs.

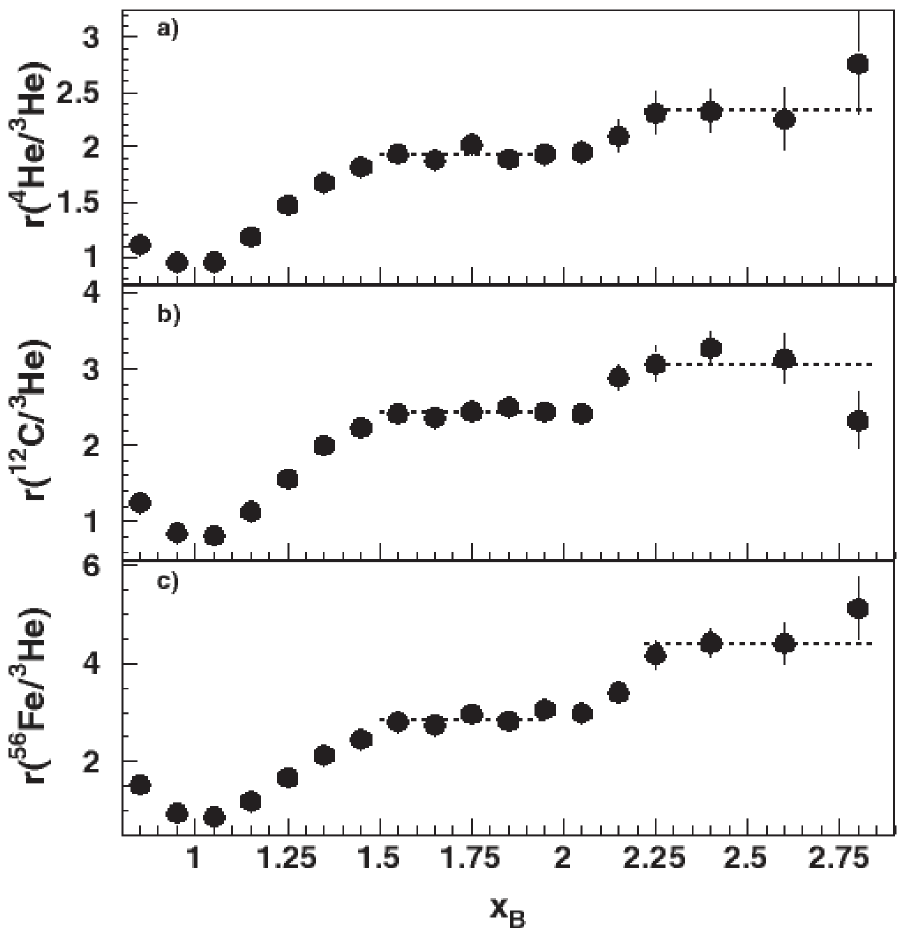

Fig. 2.6: SRC results from Hall B at Jefferson Laboratory. Shown are the cross section ratios of ^{56}Fe, ^{12}C, and ^{4}He to ^{3}He as a function of x_B for Q^2 >1.4 (GeV/c)^2. The horizontal dashed lines indicate the scaling regions for NN (1.5< x_B <2) and 3N (x_B >2.25) SRCs. This figure is reproduced from [48].

2.2.2 Short-Range Correlations from A$(e,e'p)$

The reaction A$(e,e'p)$ is a semi-exclusive one in the sense that the scattered electron and the knocked out proton are detected in coincidence, while the recoiling nucleus is not detected. The A$(e,e'p)$ reaction is potentially a rich source of information about SRCs. For the present experiment (E01-015), data from the ^{12}C$(e,e'p)$ channel are being analyzed by another student [49].

The six-fold differential cross section, $\sigma(E_m,k)$, of the semi-exclusive reaction ^{12}C$(e,e'p)$ is given as [38]

$$\begin{aligned}\sigma(E_m,k) &= \frac{d^6\sigma}{d\Omega_{e'}d\Omega_p dE' dT_p}(e,e'p) \\ &= \int d\Omega_p dE_{A-2}\frac{d^9\sigma}{dT_p d\Omega_p dT_p d\Omega_p dE' d\Omega_{e'}}(e,e'pp) \\ &+ \int d\Omega_n dE_{A-2}\frac{d^9\sigma}{dT_n d\Omega_n dT_p d\Omega_p dE' d\Omega_{e'}}(e,e'pn). \end{aligned} \tag{2.21}$$

The measurement of the cross section for the ^{12}C$(e,e'p)$ reaction can involve the contribution from two-nuclon knockout, i.e. ^{12}C$(e,e'pN)$, which needs a triple-coincidence measurement to be well charaterized, and is not the scope of the A$(e,e'p)$ experiment. Nevertheless two-nucleon-knockout information is already implicit in the A$(e,e'p)$ measurement. Also here in the notation (E_m,k) both quantities E_m and k refer to the initial state quantities [50] (i. e., before being struck by a virtual photon) of the struck proton; in the impulse approximation they are the missing energy and missing momentum of the A$(e,e'p)$ reaction, respectively.

The differential cross section for the A$(e,e'p)$ reaction can also be written as

$$\sigma(E_m,k) = \frac{d^6\sigma}{d\Omega_{e'}dE'd\Omega_p dT_p}(e,e'p) = K_c\sigma_{ep}S(E_m,k) \tag{2.22}$$

where K_c is a kinematical factor, σ_{ep} is an off-shell (bound) electron-proton cross section (in the prescription of T. de Forest [51]) and $S(E_m, k)$ is the spectral function which gives the joint probability of finding a proton with missing energy E_m and missing momentum k ($\equiv |\vec{p}_m|$) inside the nucleus. The spectral function contains the physics of the nuclear-structure information. There may be included a spectroscopic factor in S so as to match the theoretical cross section to the experimental cross section. Rewriting Eqn. (2.22) in a slightly different way, we get an expression for the spectral function

$$S(E_m, k) = (\frac{1}{K_c \sigma_{ep}}) \frac{d^6\sigma}{d\Omega_{e'} dE' d\Omega_p dT_p}(e, e'p). \tag{2.23}$$

The spectral function $S(E_m, k)$ consists of two parts [28] given as

$$S(E_m, k) = S_0(E_m, k) + S_1(E_m, k) \tag{2.24}$$

where $S_0(E_m, k)$ is the mean-field part and $S_1(E_m, k)$ is the remainder (not including the mean-field part). Another useful quantity is the momentum distribution $n(k)$ and can be written as [28]

$$n(k) = 4\pi \int_{E_{min}}^{\infty} dE_m S(k, E_m) \tag{2.25}$$

with

$$n(k) = n_0(k) + n_1(k) \tag{2.26}$$

in a similar manner to Eqn. (2.24). A typical nucleon momentum distribution was shown in Fig. 2.3. The integral of the nucleon momentumvdistribution function in the entire missing-momentum range is called the spectroscopic strength N. This N

can also have two parts in reasoning similar to equation (2.26) such that

$$N = N_0 + N_1. \tag{2.27}$$

In general, N is unity; from the A$(e, e'p)$ experiments such as [27] (see Fig. 2.2), N_0 is about 0.7 which accounts for the mean-field part and N_1 is about 0.3 which accounts for correlations, a major part of which comes from SRCs.

2.2.3 Short-Range Correlations from A$(e, e'pN)$

The reaction A$(e, e'pN)$ is also a semi-exclusive one in the sense that the scattered electron, the knocked-out proton and the recoiling nucleon are detected in coincidence. The experiment performed in this way is a triple-coincidence experiment. Due to the requirement that the three particles be detected at the same time, the cross section is exceedingly small for triple-coincidence measurements.

The concepts presented in Sect.2.2.2 apply here also after modifying the expression for the spectral function as given below:

$$S(E_m, k) = (\frac{1}{K_c \sigma_{epN}}) \frac{d^9\sigma}{d\Omega_{e'} dE' d\Omega_p dT_p d\Omega_N dT_N}(e, e'pN) \tag{2.28}$$

where the notation is obvious. Although there has been considerable effort spent in studying two-nucleon knockout reactions, as mentioned in Sect. 1.3, for example, see references [7-18], the understanding of SRCs is still in a slowly-developing phase.

The missing-energy (E_{2m}) and the missing-momentum (p_{2m}) distributions as defined in equations (2.10) and (2.11), respectively, can give an indication of the knockout of the correlated pair. Such a distribution for the missing energy for the ^{12}C$(e, e'pp)$ reaction is shown in Fig. 2.7 which is reproduced from [9]. The figure

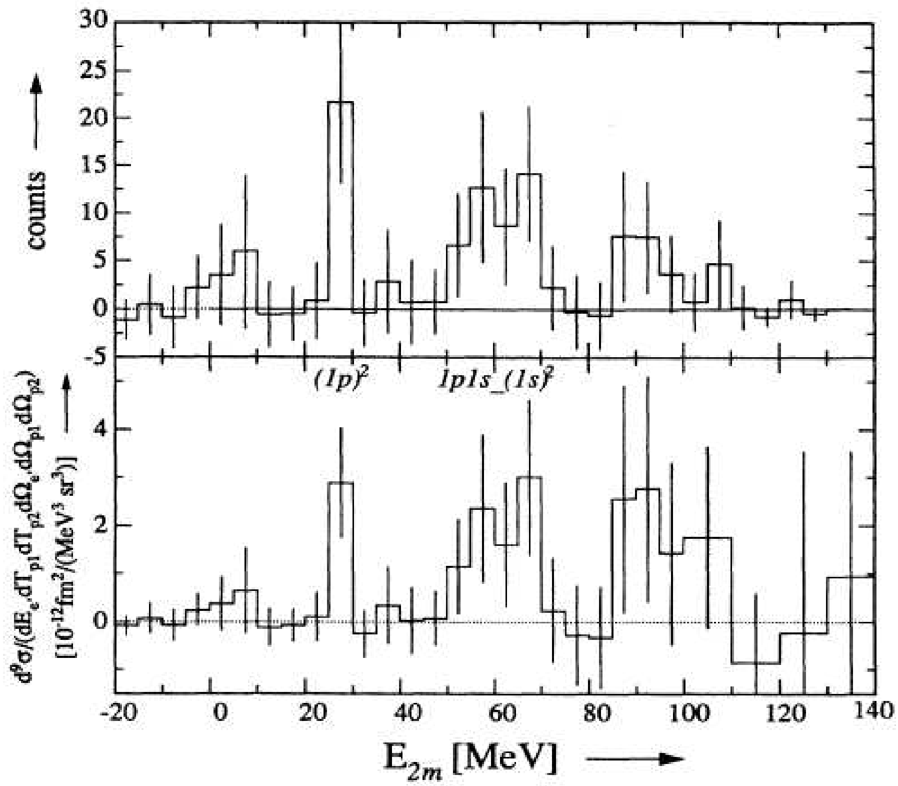

Fig. 2.7: Missing energy (E_{2m}) distribution from the ^{12}C$(e, e'pp)$ reaction, the figure is reproduced from [9].

clearly shows the $(1p)^2$ final state and an indication of either $(1p1s)$ or $(1s)^2$ states of the residual nucleus. Given sufficient statistics, one could also find, in principle, the missing-momentum (p_{2m}) distribution in an E_{2m}-range for a particular final state only. Such a distribution can describe the physics of different types of final states of the residual nucleus obtained from the two-nucleon knockout process.

The present experiment E01-015 has some unique features. It investigates NN SRCs through three channels: ^{12}C$(e, e'p)$, ^{12}C$(e, e'pp)$, and ^{12}C$(e, e'pn)$ measured simultaneously. In the latter two channels, both of the emitted correlated nucleons are detected. It is relatively high-energy experiment with $x_B > 1$, and with high four-momentum-transfer squared.

In the present investigation we neither calculate any spectral function nor extract any cross sections for the $^{12}\mathrm{C}(e,e'p)$ or $^{12}\mathrm{C}(e,e'pn)$ reactions. Instead we work with the cross section ratio of the 9-fold differential cross section for the $^{12}\mathrm{C}(e,e'pn)$ reaction to the 6-fold differential cross section for the $^{12}\mathrm{C}(e,e'p)$ reaction. Also we give the cross section ratio of the 9-fold differential cross section of the $^{12}\mathrm{C}(e,e'pn)$ reaction to the 9-fold differential cross section of the $^{12}\mathrm{C}(e,e'pp)$ reaction where the 6-fold differential cross section for the $^{12}\mathrm{C}(e,e'p)$ reaction for both cases remains the same. By working with ratios, many of the factors that contribute to the uncertainties of cross section determinations are eliminated from the final results.

Chapter 3

Setup of the Experiment

Experiments that require coincidence measurements at high momentum resolution, involving processes at high momentum transfer, are generally low cross section measurements which result in low count rates. Obtaining adequate count rates generally requres a high luminosity[1] and moderately large-acceptance detectors. Jefferson Laboratory Hall A is a unique facility that fulfills these criteria for the coicidence experiments due to the presence of two high-resolution spectrometers (HRSs). Experiment E01-015, also known as the "SRC experiment", is a triple-coincidence experiment. It ran from January through April 2005. The main aim of the experiment was to study simultaneously the ^{12}C$(e, e'p)$ reaction and the ^{12}C$(e, e'pp)$ and ^{12}C$(e, e'pn)$ reactions, as a tool to measure short-range nucleon-nucleon correlations [52].

The primary equipment in Hall A [53] is two HRSs designed specifically for A$(e, e'p)$ measurements at beam energies of several GeV. Generally the left HRS (HRSL) is instrumented for electron detection and the right HRS (HRSR) is instrumented for proton, or other heavy charged particle (π, K, ^{2}H, etc.) detection. Details on the two HRSs are given in Sect.3.4

We used both HRSs in a coincidence mode to record data for the ^{12}C$(e, e'p)$ reaction; singles data from each spectrometer were also recorded in the datastream. To measure protons or neutrons in coincidence with ^{12}C$(e, e'p)$ events, we employed

[1]The luminosity is a property of both the beam as well as the target material [25]. If L is the luminosity, $\frac{dN}{dt}$ the number of incoming beam particles per second, n the target particle density in the scattering material, and d the target thickness, then $L = nd\frac{dN}{dt}$. The unit of L is $cm^{-2}s^{-1}$.

the newly comissioned third spectrometer consisting of the “BigBite” dipole magnet [54, 55] along with its detector package, and a large neutron detector array.

For the production runs at 4.6275 GeV beam, the scattered electrons and struck protons were detected in the HRSL and HRSR, respectively, whereas the recoiling protons (neutrons) were detected in the BigBite detector (neutron detector). Both the BigBite detector and the neutron detector, as described in Sect.3.6 and 3.7, respectively, were made up of highly segmented layers of plastic scintillator detectors. Also for calibration purposes, data from hydrogen and deuterium were taken. How the experiment was set up will be described in this chapter.

3.1 Kinematic Settings

In the present experiment we had a variety of kinematical settings for three purposes: (a) commissioning of the neutron detector, (b) commissioning of the BigBite spectrometer, and (c) producing different sets of production runs. They are summarized in Table 3.1, in which only the kinematics that were used in the data analysis of this dissertation work are given. Following is a short description of these various kinematical settings:

1. LH: Liquid hydrogen (4 cm target) elastic runs with 2-pass (2.345 GeV) beam with electrons detected in the left HRS and protons detected in the neutron detector array at -50° angle located 15 meters from the target. This kinematics was dedicated to neutron-detector calibration.

2. LDK0: Liquid deuterium (15 cm target) runs with 2-pass beam where electrons were detected in the right HRS and protons in the left HRS. In all other following kinematics the HRSs' polarity was opposite relative to this kinematics and the incident electron beam was 4-pass (4.6275 GeV).

Kine-matics	E [GeV]	E' [GeV]	θ [deg]	ω [GeV]	Q^2 [(GeV/c)^2]	x_B	θ_p [deg]	$\mid \vec{q} \mid$ [GeV/c]	k [GeV/c]
LH	2.3452	1.8370	27.0	0.5082	0.9391	0.985	-	-	-
LDK0	2.3452	1.8875	-17.197	0.4577	0.3958	0.461	53.89	0.778	0.237
LDK1	4.6275	3.7612	19.5	0.8663	1.9966	1.229	-40.1	1.657	0.297
LDK2	4.6275	3.7612	19.5	0.8663	1.9966	1.229	-40.1	1.657	0.297
LDK3	4.6275	3.7232	19.5	0.9043	1.9765	1.165	-32	1.672	0.494
CK1a	4.6275	3.7612	19.5	0.8663	1.9966	1.229	-40.1	1.657	0.297
CK1b	4.6275	3.7232	19.5	0.9043	1.9765	1.165	-40.1	1.672	0.308
CK2	4.6275	3.7232	19.5	0.9043	1.9765	1.165	-35.8	1.672	0.413
CK3	4.6275	3.7232	19.5	0.9043	1.9765	1.165	-32	1.672	0.523

Table 3.1: Nominal values of spectrometer settings, beam energies and other kinematic parameters for different kinematics. The definition of variables are described in Sect.2.1.

3. LDK1: Liquid deuterium (15 cm target) runs at lower missing momentum (297 MeV/c).

4. LDK2: Liquid deuterium (4 cm target) runs at lower missing momentum (297 MeV/c).

5. LDK3: Liquid deuterium (4 cm target) runs at higher missing momentum (494 MeV/c).

6. CK1a: Carbon runs with slightly lower missing energy and with lower missing momentum (297 MeV/c).

7. CK1b: Carbon runs at lower missing momentum (308 MeV/c).

8. CK2: Carbon runs at medium missing momentum (413 MeV/c).

9. CK3: Carbon runs at higher missing momentum (523 MeV/c).

Kinematics CK3 is the most significant one for the physics results of this dissertation. Only about a week towards the end of the run-period was spent in taking data in this kinematic setting.

3.2 Jefferson Lab Hall A

Shown in Fig. 3.1 is a schematic layout of the Jefferson Laboratory accelerator site and Hall A. The electron beam is produced at the injector, then accelerated and recirculated for the desired number of passes, and directed to any of the experiment halls A, B, and C. The description of the Hall A detectors, along with the specific detectors dedicated to this experiment, is presented in the following sections. The schematic diagrams of the Jefferson Laboratory accelerator site and Hall A are shown in Fig. 3.1, while the the detector setup is shown in Fig. 3.2.

3.3 The Target System

The configuration of the target system for the E01-015 experiment is given in Table 3.2. The slanted carbon target was used for production runs, while the liquid hydrogen and liquid deuterium targets were used for calibration runs. The production carbon target was slanted because the expected recoiling particles in this experiment were relatively low energy (less than 200 MeV) protons and neutrons. In order to reduce the distance these recoiling particles had to travel in the target we placed this carbon foil at an angle of 70° with respect to the incident electron beam (see Fig. 3.3).

This experiment was the commissioning experiment for the BigBite spectrometer. Part of the new equipment for use with BigBite was a specially designed target chamber with exit windows matching the acceptances of both the HRSs and BigBite. This chamber has an extra high window to match the large vertical acceptance of the BigBite magnet in addition to the nominal window for the HRSL (the HRSR

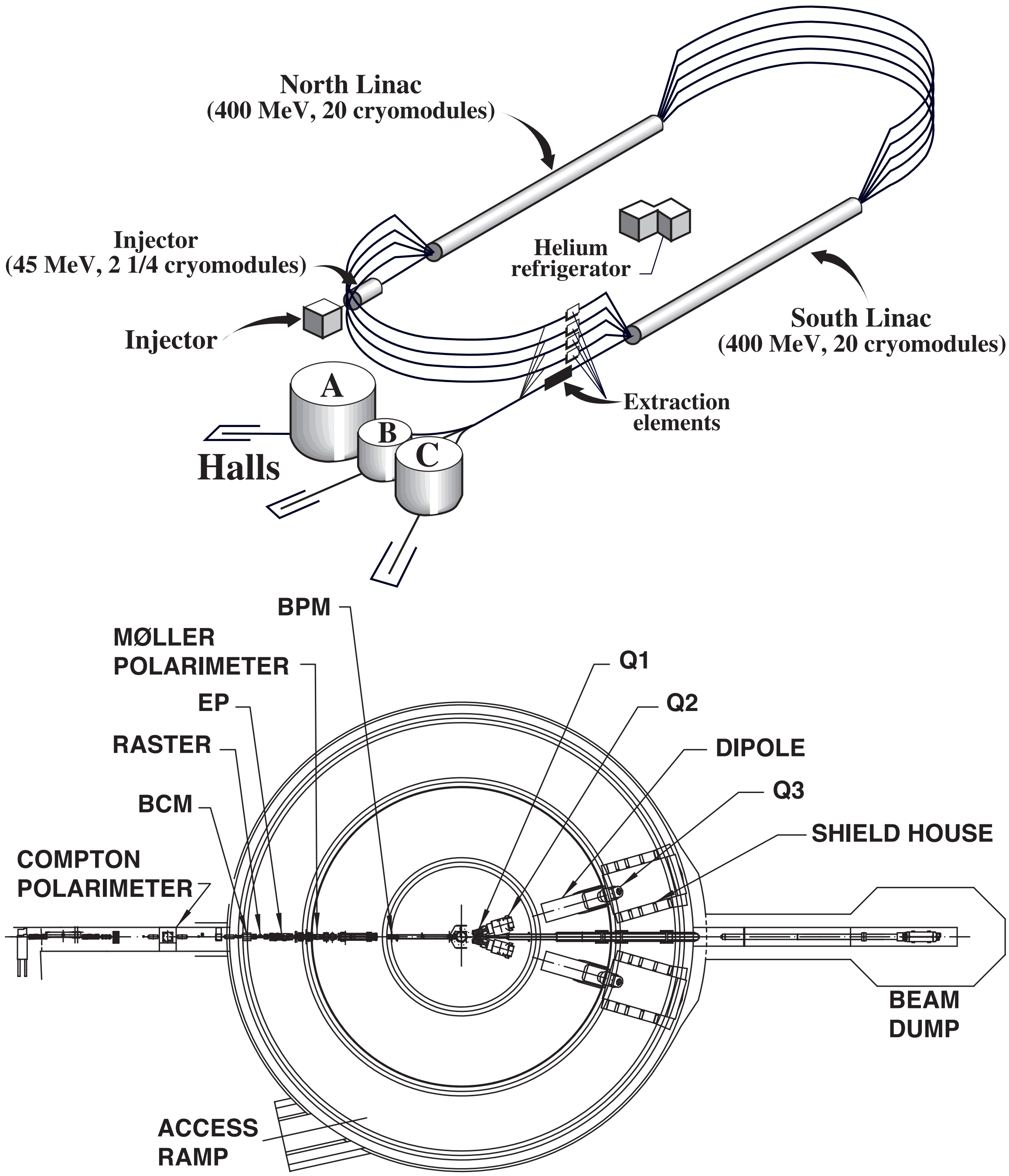

Fig. 3.1: Schematic diagrams of the Jefferson Laboratory accelerator site (top) and Hall A (bottom). The symbolic labels in the bottom figure for Hall A represent the following: BPM, BCM, and EP are beam-position monitor, beam-current monitor, and electro-proton energy measuring device, respectively; Q1, Q2, and Q3 are quadrupole magnets. These figures are taken from [53].

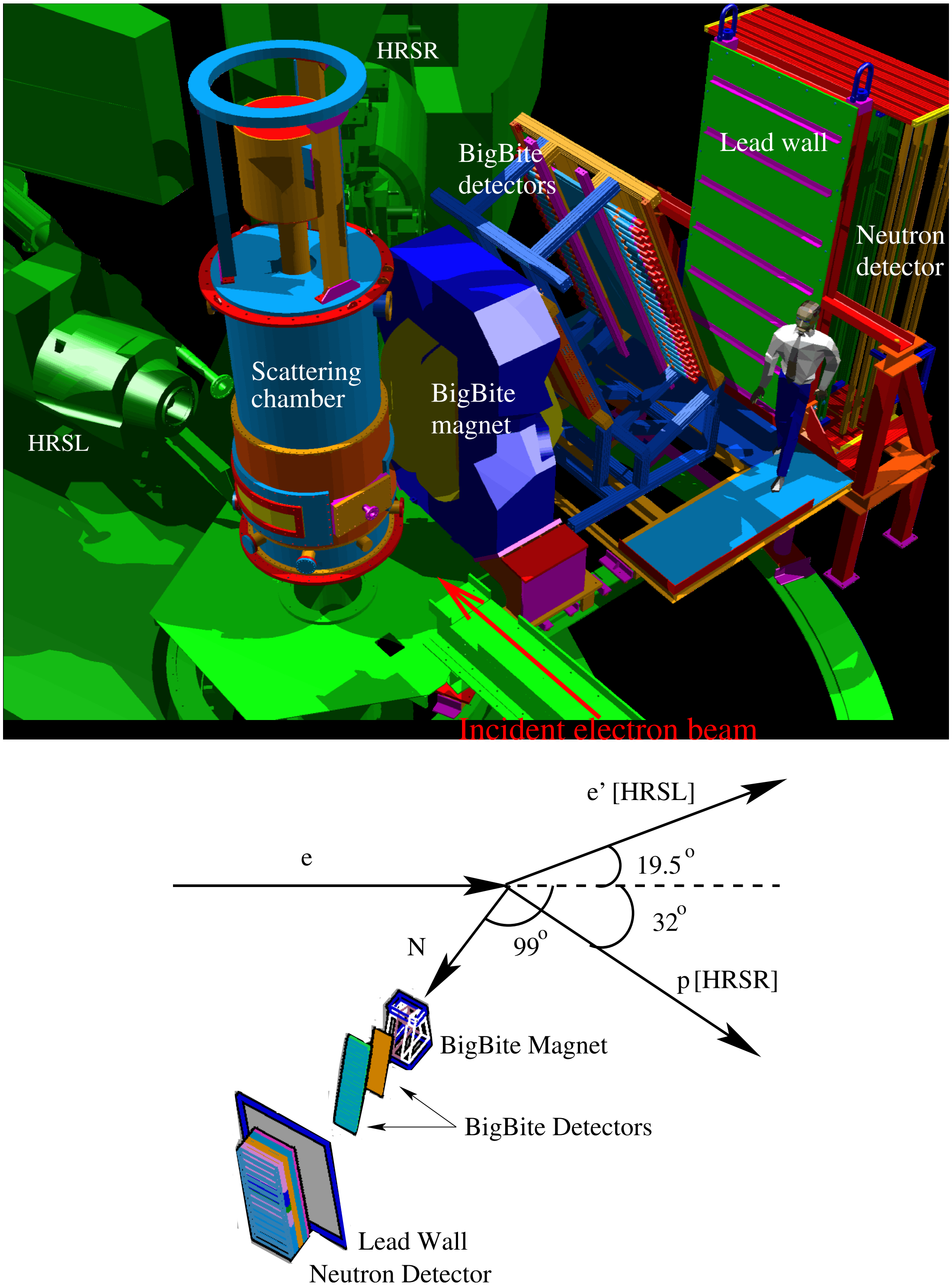

Fig. 3.2: Detector setup for experiment E01-015. At the top is a CAD (Computer Aided Drawing) picture (picture courtesy: Alan Gavalya) and at the bottom is a schematic layout for a typical kinematics.

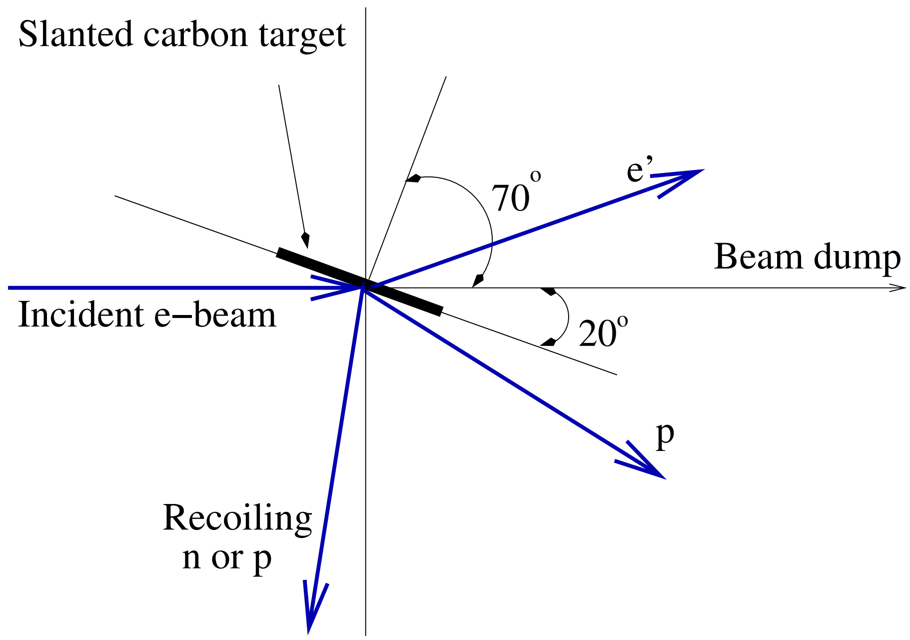

Fig. 3.3: The slanted Carbon Target showing its tilt with respect to the beam.

Position	Target	Material	Thickness (mm)	Thickness (mg/cm^2)
Slanted C	Carbon	C 99.8%	0.25	42.2±0.11
Regular C	Carbon	C 99.8%	1	173.0±1.0
Optics	Seven C foils	C 99.8%	1	173.0±1.0
BeO	BeO viewer	BeO	1	-
Loop1 4 cm	4 cm LD2	Deuterium	40±0.5	-
Loop1 15 cm	15 cm LD2	Deuterium	150±0.5	-
Loop2 4 cm	4 cm LH2	Hydrogen	40±0.5	-
Loop2 15 cm	15 cm LH2	Hydrogen	150±0.5	-
4 cm dummy	±2 cm Al foils	Al 7075	40±0.5	-
15 cm dummy	±7.5 cm Al foils	Al 7075	150±0.5	-
Empty	-	-	-	-

Table 3.2: Configuration of the target ladder for the E01-015 experiment. The target ladder can be moved vertically (both up and down) remotely and can be positioned in a desired location.

shared the same window as BigBite). The beam exit window towards BigBite had vertical height of 38.1 cm while that for HRS was half this height. The window was 0.081 cm thick and made of 2024 T6 aluminium.

3.4 The High Resolution Spectrometers

Hall A has two high resolution spectrometers as shown schematically in Fig. 3.4 (top). The magnetic elements of the HRSs consist of three superconducting quadrupoles (Q1, Q2, and Q3) and a super conducting dipole (D) in a QQDQ arrangement, see Fig. 3.4 (bottom). Quadrupole Q1 focuses in the vertical plane whereas both Q2 and Q3 provide vertical defocusing. The 6.6 m long dipole, providing a vertical bend of 45°, has focussing entrance and exit polefaces and includes additionanl focussing from the field gradient in the dipole. For details about the magnetic elements and design of the HRSs see [53].

In this experiment, for the most of the production runs, HRSL was used as the electron spectrometer and HRSR was used as the proton spectrometer. In some of the kinematics, dedicated for calibration runs, we reversed their roles. In other calibration runs, HRSR was not used at all.

The detector package in each spectrometer is housed within a shielding hut and is located on top of the HRS structure immediately after Q3. The detector package configuration is very flexible. What detector configuration to use, which detector elements to add, keep or remove depends upon the need of the individual experiment. In this experiment, in addition to two vertical drift chambers (VDC) in both HRSs, the spectrometers had the following detector packages (schematic layout shown in Fig. 3.5). The left HRS had scintillator planes S1 and S2, a Gas Cherenkov detector, and a shower detector functioning as a pion rejector. The Gas

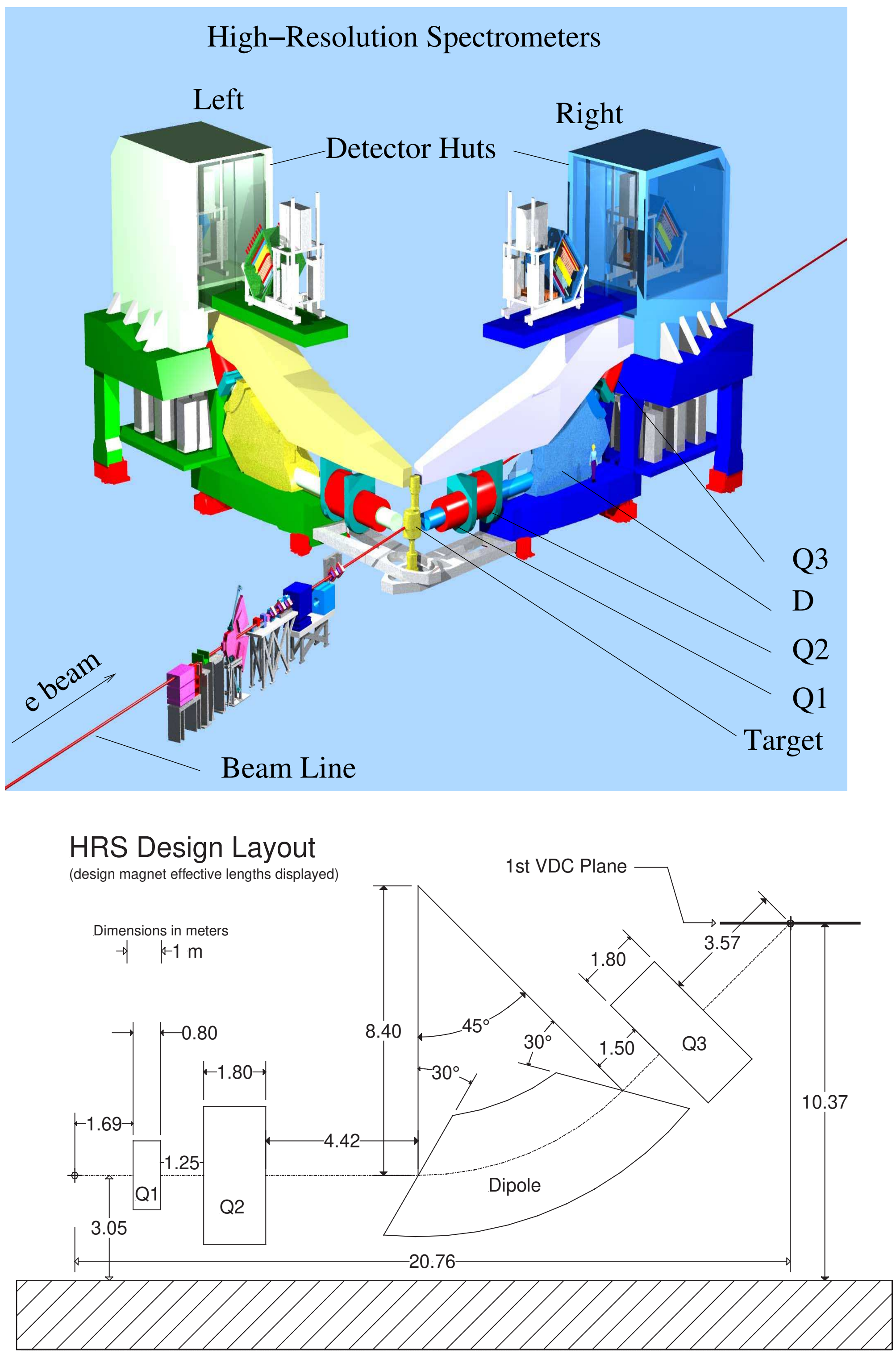

Fig. 3.4: The high-resolution spectrometers in Hall A, figures are taken from [56](top) and [53](bottom). The symbols Q1, Q2 and Q3 represent different quadrupole magnets; D represents a dipole magnet.

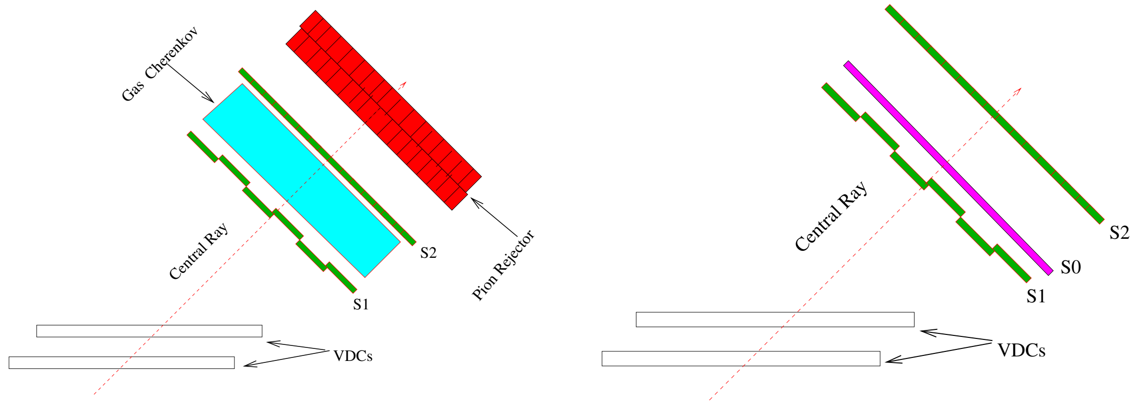

Fig. 3.5: Schematic layout of the detectors (not to scale) for the HRSs. The left sketch shows the detectors in the left HRS and the right sketch shows the same in the right HRS.

Cherenkov detector was physically removed from the left HRS detector stack during the middle of the CK3 kinematics in order to make room for a RICH (Ring Imaging Cherenkov) detector for a later experiment. The right HRS had only the S0, S1 and S2 scintillator planes; S0 was placed between S1 and S2.

3.4.1 The Vertical Drift Chambers

The vertical drift chambers (VDCs) in the HRSs are well established, reliable and standard detector packages for particle tracking, providing precise determination of the positions and angles of incident charged particles passing through them. Each HRS has a pair of VDCs; their schematic layout is shown in Fig. 3.6. The two VDCs are identical and stay parallel to each other and also parallel to the hall floor. Each chamber is approximately 240 cm long, 40 cm wide, and 10 cm high, covering an active area of 211.8 x 28.8 cm^2. The chambers are seperated by 33.5 cm.

Furthermore, each VDC has two orthogonal wire planes which are parallel to each other. These planes are also inclined at an angle of 45° with respecct to the dispersive and non-dispersive directions. The central particle trajectory crosses the wire planes at an angle of 45°. There are 368 gold plated tungsten sense-wires, spaced 4.24 mm apart, strung in each wire plane. When a charged particle passes through one of the chambers, it ionizes gas atoms in the chamber and produces a trail of electrons and ions. There is a uniform electric field between a wire plane set at ∼1.9 kV and a gold-plated Mylar cathode plane set at -4 kV. The liberated electrons are attracted to the nearest sense-wire. There is one multihit time-to-digital convertor (TDC) channel for each sense-wire. The sense-wire signal goes to a multihit TDC and the main trigger for the HRS provides the common stop. By detecting which wire was hit by the particle, the position is acurately determined. A typical track generates signals in about five wires per plane. For VDC details see [57].

3.4.2 The Scintillator Planes

In order to provide the main event triggers and time-of-flight information, there were S1 and S2 scintillator planes in both of the spectrometers. How the main triggers are formed from the signals from the scintillator planes is described in Sect.3.5. By knowing the time-of-flight of a particle between the two scintillator planes, and the distance between them, we can calculate β for the particle where $\beta = v/c$, c being the speed of light in vacuum and v the particle's speed. For the HRSR we used β for particle identification (PID) since we did not have any other PID detectors installed in that arm for this experiment.

The S1 and S2 planes had the same design in both HRSs. The S1 plane had six plastic scintillator paddles of dimensions 0.5 cm x 29.3 cm x 36 cm whereas S2 had sixteen paddles of dimensions 5.08 cm x 13.97 cm x 43.18 cm. The paddles in S1 were overlapping by about 0.5 cm whereas the paddles in S2 were tightly stacked

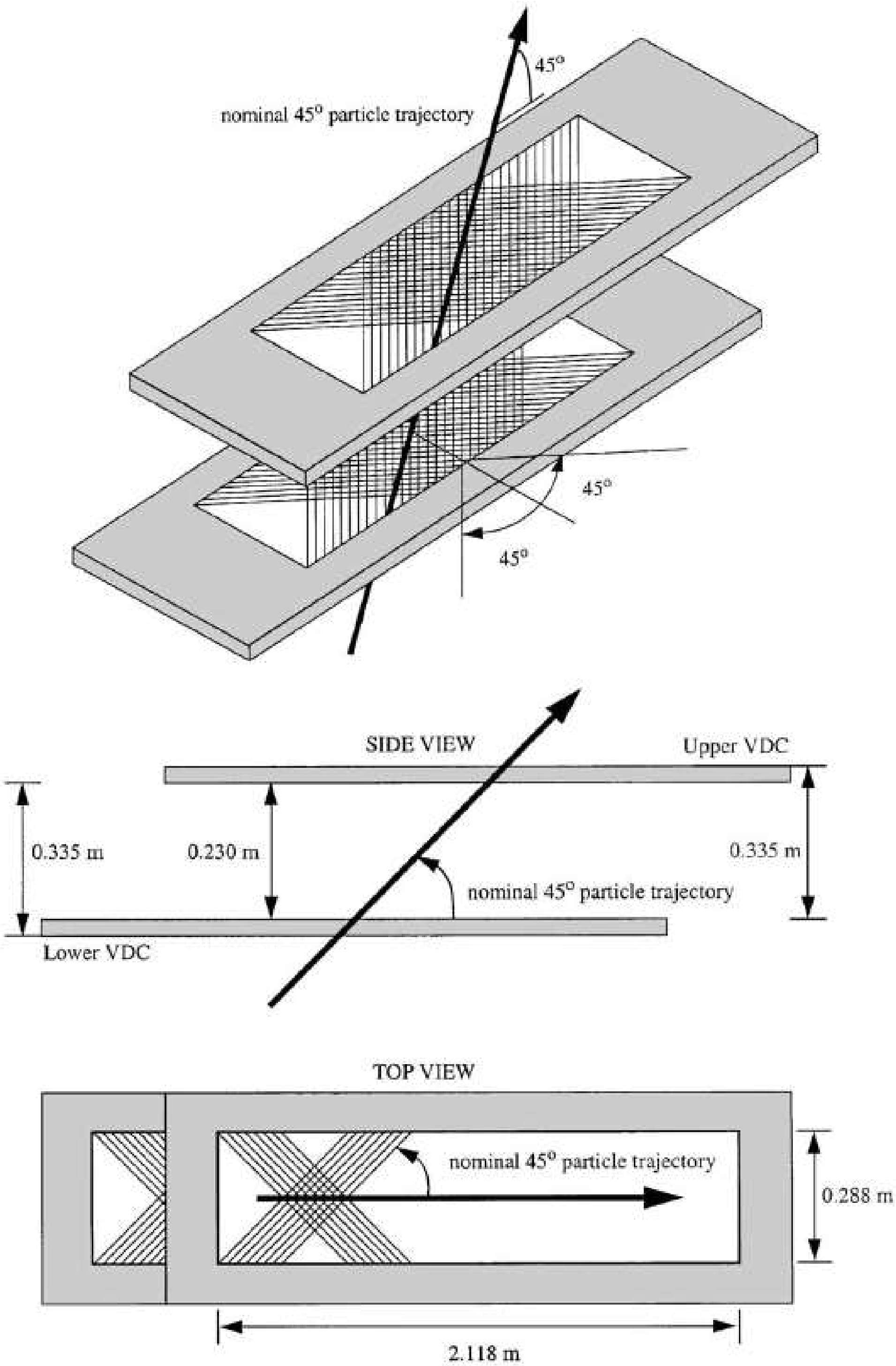

Fig. 3.6: Schematic layout of the VDCs (Fig. from [57]).

without any overlap. Each paddle was viewed by two phototubes attached at its ends. HRSR had an additional S0 plane consisting of a single paddle of dimensions 0.5 cm x 25 cm x 176 cm. The distance between S1 and S0 was 43.5 cm while that between S1 and S2 was 202.2 (181.5) cm in the right (left) HRS.

3.4.3 The Gas Cherenkov Detector

The gas Cherenkov detector provides excellent particle identification for electrons, by rejecting pions. The idea is to choose a certain gas such that it does not emit Cherenkov radiation by pions of the momentum range of interest. Cherenkov light is emitted when a charged particle in a material medium moves faster than the speed of light in that medium. The speed of light in the medium is

$$v = c/n \tag{3.1}$$

where n is the index of refraction. In order to emit Cherenkov light one should have

$$v = \beta c \geqslant c/n \tag{3.2}$$

where βc is v, the speed of the particle. In this situation light is emitted in a well-defined cone of half angle θ given by (see [58])

$$cos\theta = \frac{1}{\beta n}. \tag{3.3}$$

The Hall A gas Cherenkov tank utilezes CO_2 gas at atmospheric pressure with an index of refraction 1.00041. It has ten mirrors arranged in two rows, and each mirror is viewed by one phototube. For details see [59] and for the position of the Cherenkov detector in the detector stack see Fig. 3.5.

For electrons ($\beta \simeq 1$), $n = 1.00041$ translates to half-cone angle of 1.64 degrees, hence the light is emitted in the forward direction. In order to calculate the threshold momentum (p_{th}) for Cherenkov light emission, we use the threshold relation from Eqn.(3.2) by replacing βc with $\frac{c}{n}$ in the following equation

$$E = \gamma mc^2 = \sqrt{m^2c^4 + p^2c^2} \tag{3.4}$$

where $\gamma = 1/\sqrt{1-\beta^2}$ and obtain

$$p_{th} = \frac{mc}{\sqrt{n^2 - 1}} \tag{3.5}$$

For electrons we find p_{th} = 17.84 MeV/c, hence in experiment E01-015, electrons always produced Cherenkov light since HRSL was always set for electron energies > 1 GeV. On the other hand, for pions we find p_{th} = 4888.51 MeV/c, hence pions never produced Cherenkov light because the central momentum settings for the spectrometers were never more than 3800 MeV/c.

In this experiment, although the electron signal from the Cherenkov detector was very clean, any residual pion contamination was removed using the shower detectors described in the next section.

3.4.4 The Pion Rejector

The pion rejector, consisting of a pair of shower detectors, is another PID detector, and is a miniature form of an electromagnetic calorimeter. An electromagnetic calorimeter measures the energy deposited by charged particles when they travel through it. Shower detectors are generally made of high Z materials, since the probability of forming an electromagnetic shower is a strong function of Z. The pion rejector is made of lead glass.

When the energetic electrons are incident on a shower detector, an electromagnetic shower consisting of electrons (e^-), positrons (e^+), and photons is formed. Formation of such a cascade continues until the energy of the particles falls below about 100 MeV, at which point dissipative processes, such as ionization and excitation, occur. In principle, the energetic charged particles produce an electromagnetic shower, and the photons in the shower appear as Cherenkov light which is collected in the phototubes of the shower dector.

The absorption length or the mean-free path (the mean distance traveled before a collision) of an electron is not the same as that of a pion . For example, a 15 cm thick lead-glass is good enough for absorbing electrons while this thickness is too short for pions since they have a long absorption length. The result is that we can find a large energy deposition by electrons and only a small energy deposition by pions.

The pion rejector was present only in the HRSL. It was made up of two layers of lead glass blocks. Each layer had 34 blocks, making a stack of seventeen rows, each row having two blocks of dimensions 15 cm x 15 cm x 30 cm and 15 cm x 15 cm x 35 cm. Each block was viewed by one phototube on one end only. The two individual blocks in a row were separately wrapped in aluminized mylar and the pair was wrapped in black paper to ensure the system was not exposed to external photons. The black paper was wrapped in such a way that the ends which did not have phototubes attached would face each other. The blocks were assembled in a plane as shown in Fig. 3.7. The relative positioning of this detector is shown in Fig. 3.5. For more details see [53].

Fig. 3.7: Schematic layout of the HRSL pion rejector (not to scale). The left figure shows one detector plane (front view) and the right figure shows the stacking of two such planes as a single detector stack (side view).

3.5 Trigger

With the addition of the BigBite spectrometer and the neutron detector to the complement of Hall A equipment, a new readout package, with a new trigger system, had to be designed for this experiment. The electronics readout system for the BigBite detector and the neutron detector was located on the hall floor on the right side (while viewing the beam dump from the target) of the beam line. In order to protect the electronics from possible radiation damage, a large concrete shield was constructed between the electronics area and the target. Though the HRS detector readout electronics was sitting in the detector huts, and all readout controllers were also in the huts, all individual HRS triggers, the BigBite detector trigger and the neutron detector trigger were set up in a trigger supervisor module that was sitting in the BigBite electronics racks on the hall floor.

In the following definitions of "T" triggers, it is assumed that when a scintillator plane generates a signal, that signal was obtained from a logical OR of all of its individual bar signals. The individual bar signal is a coicidence signal between the two phototubes on a bar. The following triggers were registered into the datastream when the following conditions were fulfilled.

- T1 trigger: both scintillator planes in the HRSR have signals in a timing window of about 100 ns.

- T2 trigger: in HRSR, either the S1 or S2 scintillator plane has a signal and the S0 scintillator plane has a signal.

- T3 trigger: both scintillator planes in HRSR have signals in a timing window of about 50 ns.

- T4 trigger: in HRSL, only one of the scintillator planes and the Gas Cherenkov detector have signals.

- T5 trigger: the logical AND of T1 and T3 in a timing window of about 100 ns, and made earlier by 60 to 80 ns compared to all other triggers.

- T6 trigger (for detail see section 3.6.1): the trigger from the BigBite detector, but not recorded in the datastream due to a very high rate in this trigger.

- T7 trigger (for detail see section 3.7): trigger from the neutron detector, but not recorded in the datastream due to a very high rate for this trigger.

The Hall A data aquisition (DAQ) system can handle event rates up to about 2 kHz. In the E01-015 experiment, the DAQ system had event rate below 500 Hz, in order to keep the electronic deadtime below 20%. A trigger determines whether an event should be recorded by the DAQ system. This experiment had the seven T triggers (defined above) and one timing trigger. There were only three main physics triggers, namely T1, T3 and T5. The event trigger T3 provided gates to the ADCs (Analog-to-Digital Convertors) of the BigBite detector as well as to the ADCs of the neutron detector. In addition, T3 also provided a common start to the TDCs (Time-to-Digital Convertors) of the BigBite detector and a common stop to the TDCs of the neutron detector. The triggers T2 and T4 were used to check the inefficiency of the scintillators in the HRSs.

Although T6 and T7 were not recorded in the datastream, they were useful to check whether the timing for the signals in the BigBite detector and in the neutron detector were reasonably correct. Irrespective of T6 and T7, all ADCs and TDCs from both the BigBite detector and the neutron detector were read out in the datastream.

All triggers were sent to scalers before they were sent to the Trigger Supervisor. The Trigger Supervisor provides the interface between the trigger hardware and the computer DAQ system. It synchronizes the readout crates, administers the deadtime logic of the entire system and prescales the T triggers (T1,T2,...,etc.). A prescale factor of N is applied independently to each trigger type. A prescale factor of N for a trigger type i means that the Trigger Supervisor reads out every Nth event of type i.

3.6 The BigBite Spectrometer

E01-015 experiment was one of the "major installation" experiments in Hall A and successfully commissioned the BigBite spectrometer. The BigBite spectrometer consists of a large acceptance dipole magnet followed by the BigBite detector package. Unlike the focusing QQDQ magnet-system in HRSs, the BigBite spectrometer is non-focusing. The nominal momentum acceptance of this spectrometer is 200 to

900 MeV/c [54, 55] and the angular acceptance when the magnet is 1.1 m from the target is 96 msr. The horizontal and vertical openings of the magnet are 25 cm and 148 cm, respectively, which define the horizontal and vertical acceptances, respectively. Figure 3.8 (and Fig. 3.2 as well) shows a schematic layout of this spectrometer followed by the neutron detector, and Fig. 3.9 is a CAD rendering of BigBite and its detector package. Figure 3.10 shows the photograph of these detectors in place for the experiment.

There is a flood of proposals that wish to utilize BigBite. A partial list of Hall A experiments that use or plan to use the BigBite spectrometer (though not necessarily the SRC detector package) are listed here:

1. E01-015, This SRC experiment, BigBite detecting protons [52].
2. E02-013, G_E^n experiment, BigBite detecting electrons [60] (completed data taking).
3. E04-007: π^0 threshold experiment, BigBite detecting protons [61].
4. E05-009: Resonance experiment, BigBite detecting K^+s [62].
5. E05-102: $^3He(e,e'd)$ experiment, BigBite detecting deuterons [63].
6. E06-010: Transversity experiment, BigBite detecting electrons [64].
7. E06-014: d_2^n, BigBite detecting electrons [65].
8. E12-06-122: A_1^n at 12 GeV, BigBite detecting electrons [66].
9. E07-006: second generation SRC experiment, BigBite detecting protons [67].

Any charged particle entering into the BigBite magnetic field is deflected by the magnetic field. Before and after the magnetic field, the particle trajectory is a

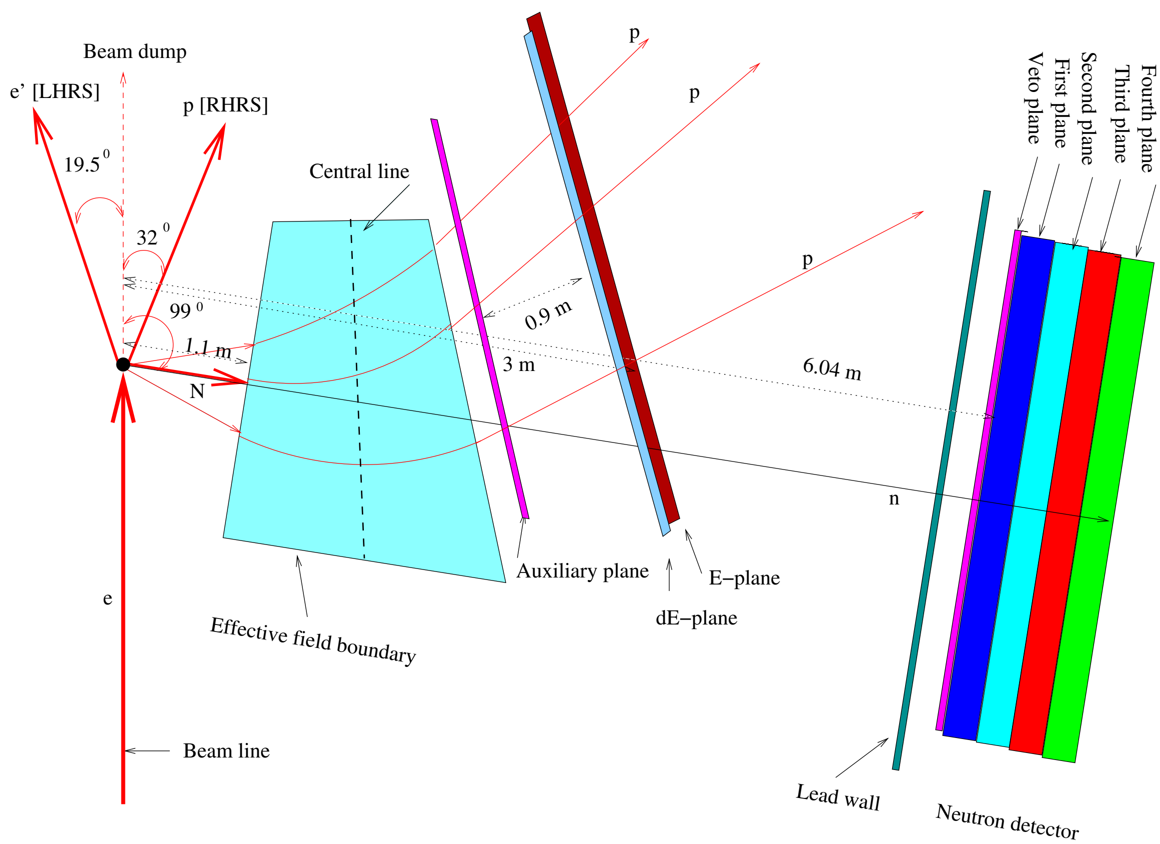

Fig. 3.8: Layout of the BigBite spectrometer and the neutron detector with respect to the beam line (not to scale). BigBite and the neutron detector are rotated by 90°, vertically, in this drawing.

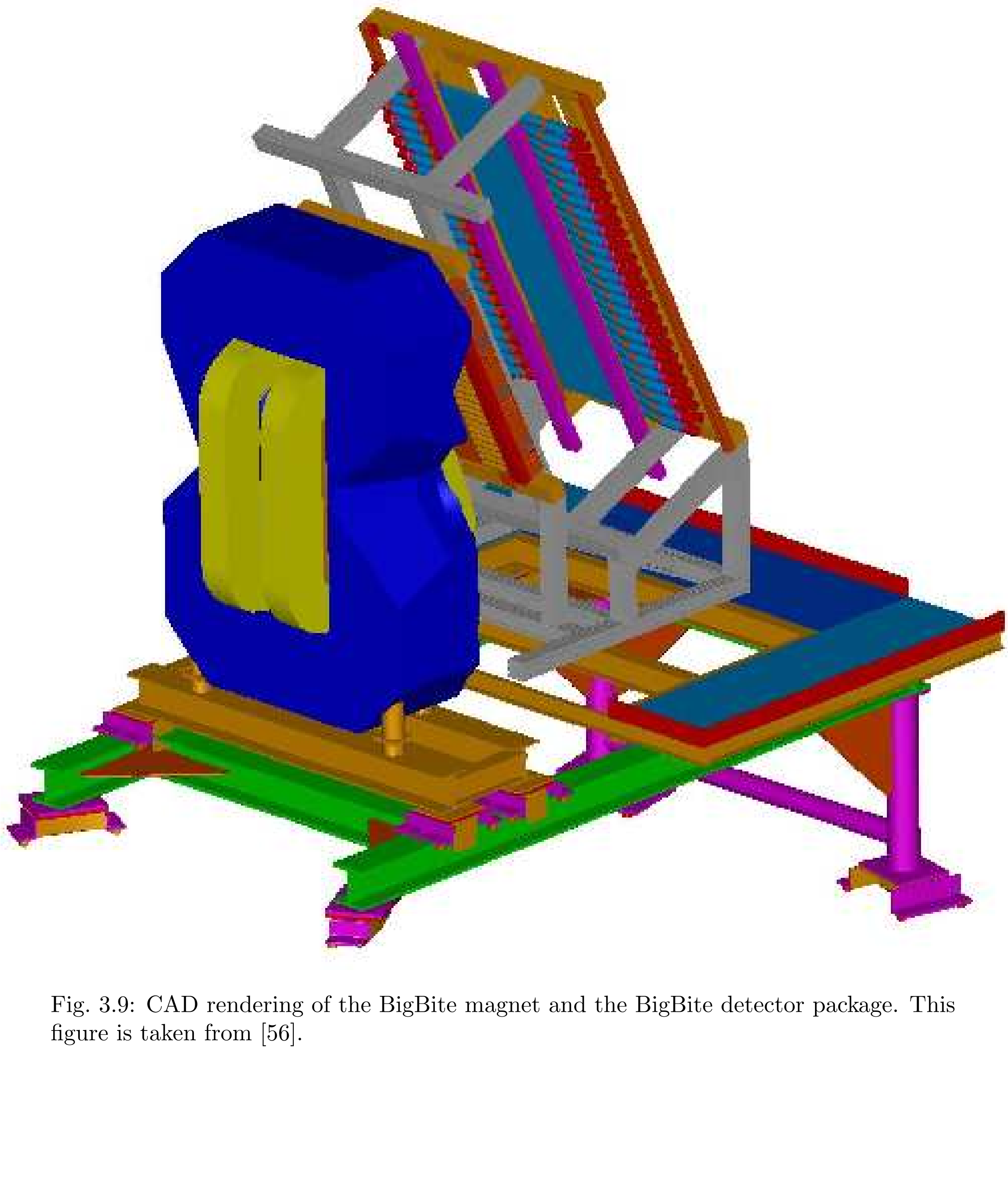

Fig. 3.9: CAD rendering of the BigBite magnet and the BigBite detector package. This figure is taken from [56].

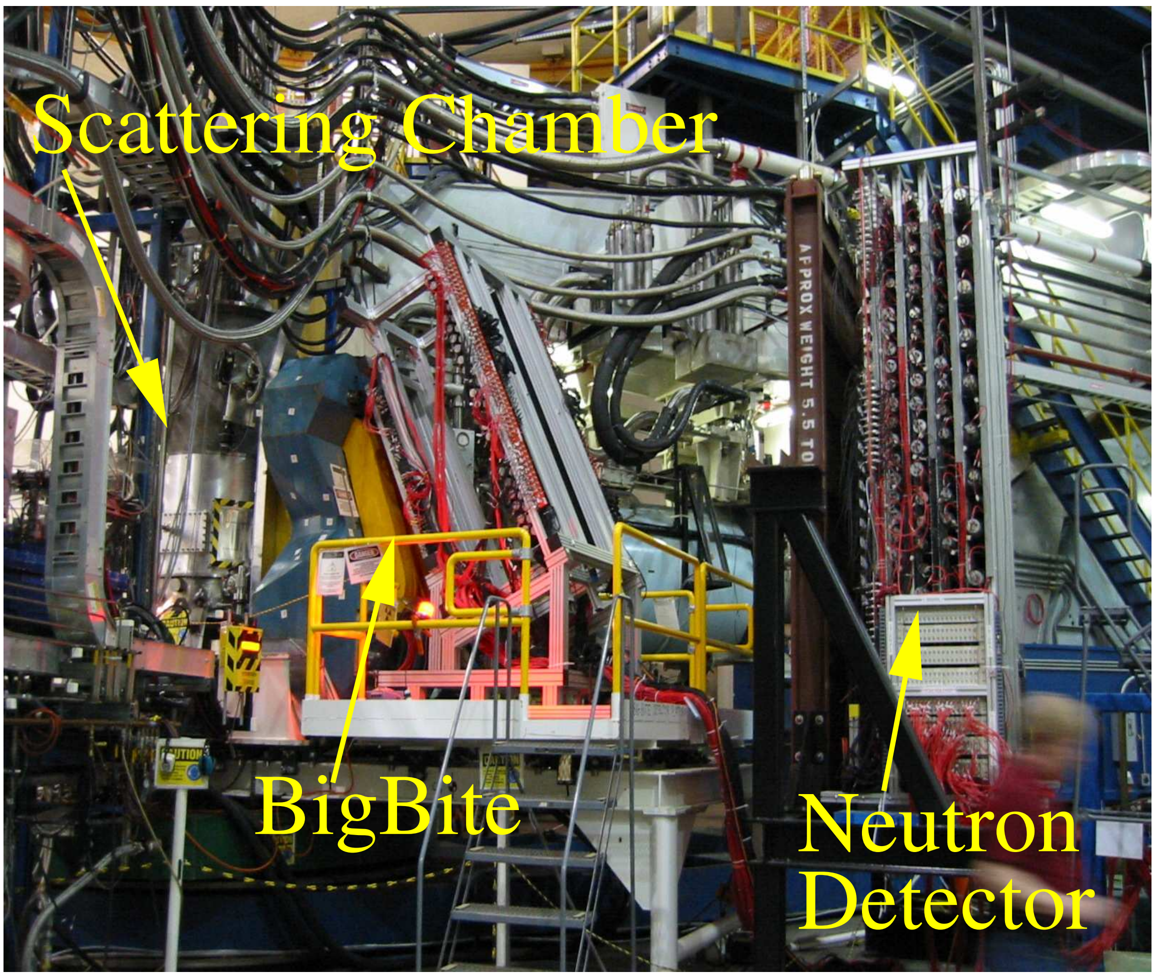

Fig. 3.10: Photograph of the BigBite spectrometer and the neutron detector as they were configured during the experiment (figure courtesy: Peter Monaghan).

straight line, while inside the field it is circular (see Fig. 3.8). The circular motion is described by the equation $\vec{F} = q\vec{v}$ **x** $\vec{B}$ where $\vec{F}$ is Lorentz force experienced by a particle of charge q with velocity $\vec{v}$ in the magnetic field of strength $\vec{B}$.

A field strength of 0.93 T was used during the E01-015 experiment; the current drawn by the BigBite magnet for this field was 518 A. Protons were deflected upwards inside the field and swept into the BigBite detector system. Neutrons passing through BigBite were not affected by the BigBite field, and followed a straight line path to the neutron detector.

The BigBite spectrometer was located at 99° right of the beam line during all production runs. The distance between the target and the entrance to the BigBite magnet was always 1.1 m.

3.6.1 The BigBite Detector Package

The BigBite detector package (see details in [68, 69]) consisted of three scintillator planes: the auxiliary plane, the dE-plane and the E-plane as shown in Fig. 3.8 (and also in Fig. 3.9). The auxiliary plane had 56 thin scintillator paddles of dimensions 2.5 mm x 25 mm x 350 mm, each paddle being viewed by one phototube on one end.

The dE- and E-planes both had 24 scintillator paddles, each 50 cm long and 8.6 cm wide. The thickness of a dE-counter was 3 mm while that of an E-counter was 30 mm. Each counter in the dE- and E-planes was viewed by two phototubes. The dE-bars were thin so that protons lost only a negligible amount of energy, whereas the E-bars were thick so that all or most of the proton kinetic energy was lost there. The combination of the dE- and E-planes was called the trigger plane because they formed the trigger for the particles (protons) to be detected by the BigBite detector.

The electronics block diagram for reading out each scintillator and sending the signals to the DAQ system, is shown in Fig. 3.11. The phototube signals were first amplified ten times using amplifiers giving two identical outputs. One output is delayed by 500 nanoseconds and sent to the ADC module which digitizes the charge accumulated over a specific interval (the time period of the gate). The other output was sent without delay to a discriminator to produce a logic pulse. Again two outputs were produced by the discriminator. One output was sent to form a trigger (T6) for the BigBite detector. The other output was delayed by 500 nanoseconds and sent to a CAMAC module which again produced two outputs. One output was sent to a scaler module (VME) and the remaining output was sent to the TDC module (VME).

The purpose of the high segmentation of each plane was to accomodate the high count rates that were expected in these planes, and also to get better position and momentum resolutions by track reconstruction. We utilized two methods for track reconstructions. One method involved finding the time-of-flight between the auxiliary plane and the trigger plane, where there is no magnetic field. The other method involved finding the time-of-flight between the target and the trigger plane, where the bending of the trajectory of the proton in the magnetic field is used. The distance between the target and trigger plane was about 3 m whereas that between auxiliary plane and the trigger plane was about 0.9 m. Details of the analysis of proton events in the BigBite spectrometer can be found in [69].

3.7 The Neutron Detector

In the setup for production runs at high energy (4.6275 GeV), the neutron detector was sitting downstream of the BigBite spectrometer. From a survey report [70] (see also in internal report from P. Monaghan [71] for E01-015 experiment),

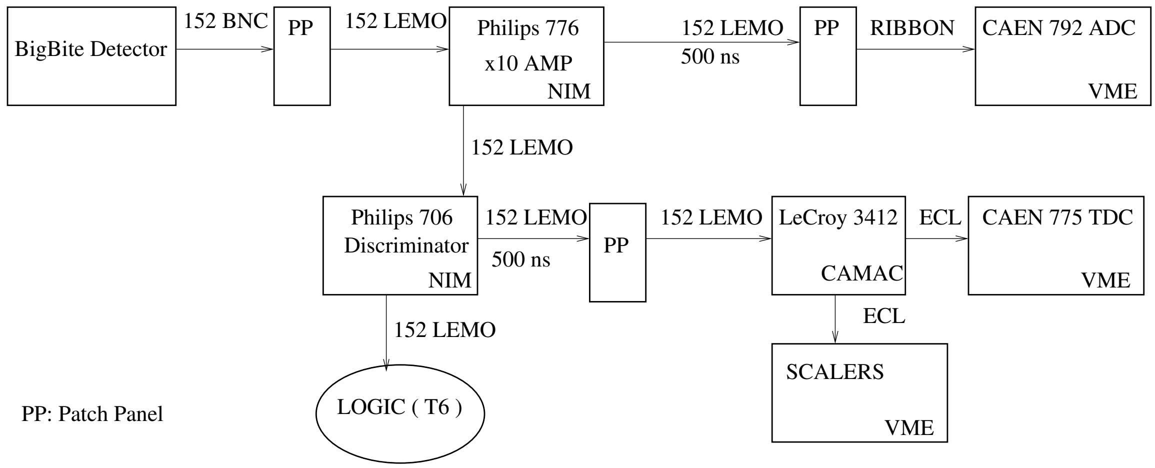

Fig. 3.11: Electronics block diagram for the BigBite detector. Here PP refer to patch pannel.

the distance between target and front of the first plane of the neutron detector was 6.04 m. During calibration runs, the neutron detector was 15 m from the target at 50° right of the beam line. See Fig. 3.8 for a relative postion of the neutron detector in the hall for a typical production run kinematics. There were four scintillator planes in the neutron detector (see Fig. 3.12), each plane consisting of a different number of scintillators of various dimensions.

Neutrons do not interact directly in plastic scintillator material since they are electrically neutral. For this reason their detection process usually involves substantial background. In order to increase the neutron detection efficiency a large neutron detector consisting of 88 plastic scintillator bars in four layers, each layer being 10 cm thick, 100 cm wide and about 300 cm high, was constructed for this experiment. There was a variety of sizes, particularly in the height of the scintillators in the neutron detector. The scintillators were acquired from several different institutions: Kent State University, Tel Aviv University, Indiana University Cyclotron Facility, Hampton University, Jefferson Laboratory Hall C, and Yerevan Physics Institute.

With four layers of scintillator bars, each 10 cm thick, the effective volume of the

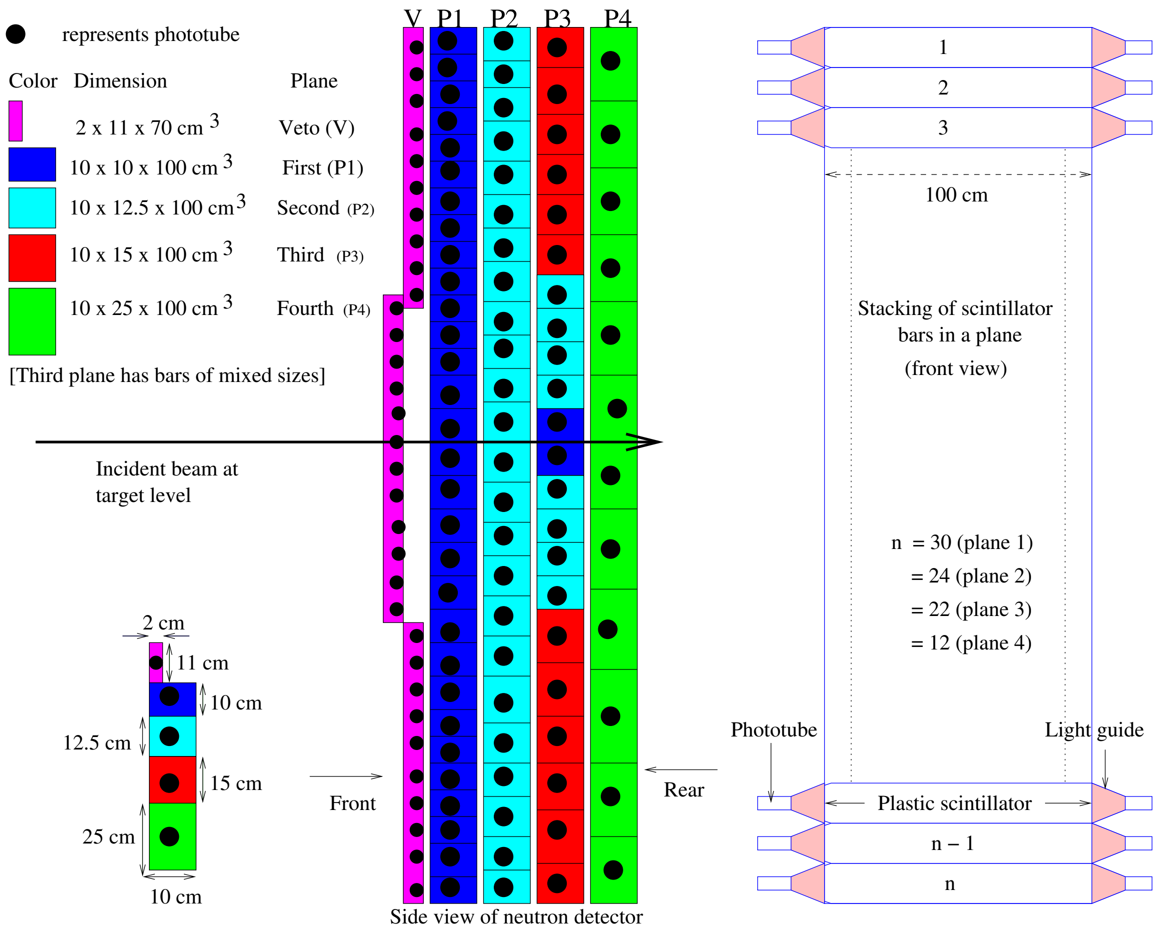

Fig. 3.12: Neutron detector configuration.

neutron detector (excluding the veto layer) was 300 cm (height) x 100 cm (width) x 40 cm (thickness). The physical size was 317 cm in height and 59 cm in thickness due to spacing between the scintillator bars as well as between the layers. The in-plane acceptance of this detector was about $\pm 5°$ while the out-of-plane acceptance was about $\pm 15°$ when the neutron detector was sitting at 6.04 m from the target. Each scintillator bar was viewed by two phototubes, one on each end.

3.7.1 The Neutron Detector Planes

Below is a description of how each plane was stacked in the neutron detector. The basic guideline for designing each plane was matching of acceptance of the neutron detector to the acceptance of the BigBite magnet.

Each plane had bars of length 100 cm and thickness 10 cm. The height was variable. The first plane had 30 bars of height 10 cm each. Second plane had 24 bars of height 12.5 cm each and the fourth plane had 12 bars of height 25 cm each. The third plane had 22 bars of mixed heights. Two bars in the middle had heights of 10 cm each, another eight bars had heights of 12.5 cm each, and the remaining 12 bars had heights of 15 cm each.

3.7.2 The Veto plane

In order to identify charged particles that hit the neutron detector, we used a 2 cm thick "veto" layer in front of the neutron detector. Veto detectors are generally thin since a charged particle can easily deposit energy in a thin plastic scintillator. A neutral particle, on the other hand, can pass through without depositing any noticeable energy in a thin plastic scintillator. The veto layer used in the present experiment had 64 paddles in 32 rows, each row having two paddles with a 30 cm overlap between them, see Fig. 3.13 for the overlapping scheme. The length, width and thickness of each paddle was 70 cm, 11 cm, and 2 cm, respectively.

All of the veto paddles were newly made at Jefferson lab shortly before the E01-015 experiment. The plastic scintillator paddles were first cleaned using water. One end of each paddle was glued to a light guide, and the other end of the light guide was glued a phototube (XP2972/02 from Photonis). The gluing was done with an ultraviolet (UV) light curable epoxy. The advantage of this glue was that

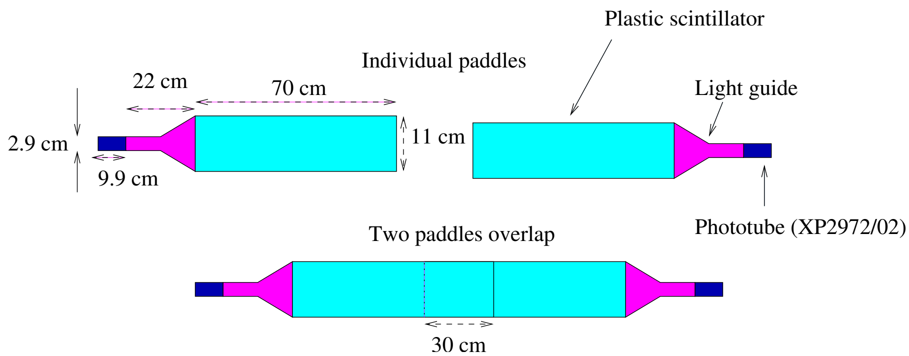

Fig. 3.13: Veto paddles (front view).

the glue would set as soon as it was exposed to the UV light. The paddle was then ready for wrapping.

Each veto paddle was wrapped with aluminized mylar with its non-conducting surface towards the surface of the paddle. Each paddle was then wrapped with heavy black PVC plastic of thickness 0.5 mm to make the paddle light tight so that no photons would enter the system from outside. Each paddle was then carefully tested for light-tightness.

Light-tightness was tested by measuring the dark current of the phototube. The dark current was measured at a high voltage (HV) of about 1.5 kV. This HV was higher than the intended HV (1.1 kV) for the experiment for these paddles. Generally, the higher the HV, higher the dark current. It was observed that the dark current was almost always less than 40 nA. If the dark current was of the order of 100 nA then the paddle was subject to a further investigation. The problem could be in the wrapping, the gluing or both. There were several glued joints in each paddle: the joint between scintillator and the light guide, between the light guide and phototube, and even between the two parts (trapezoidal and cylindrical) of the light guides. The dark current was also measured by covering the paddle with a heavy thick black cloth on different positions of the paddle to see if there was any variation before and after covering.

3.7.3 Electronics

The electronics block diagram for reading out the signals from each scintillator bar, and sending those signals to DAQ system is shown in Fig 3.14. Below is described how the electronics circuitry was setup. Each phototube signal, after being delayed by 237 ns, was first amplified by a factor of ten, using an amplifier giving two copies of the output. One copy was delayed by 500 nanosecond and sent to a FASTBUS 1881 ADC module[2]. Another copy was sent to a LeCroy 4413 (CAMAC) discriminator which was capable of giving two copies of its output. One copy was sent to a VME scaler module and the remaining copy, after a 500 nanosecond delay, was sent to a FASTBUS 1877 TDC module. In order to make the trigger (T7) from the neutron-detector scintillators, the signal from the summing module was sent to another LeCroy 4413 (CAMAC) discriminator with a threshold of 300 mV and the output from this discriminator was fed into a logic unit forming the T7 trigger.

The FASTBUS 1887 TDC modules had a time-per-channel of 0.5 ns and were operated in a common-stop mode. In this mode, an event such as a signal from the neutron detector, started the timing in the TDCs. The TDC timing was stopped by the T3 trigger for this event, and subsequently the event was readout in the datastream. The FASTBUS 1881 ADC modules in this experiment were gated by a gate period of 200 ns, and that gate was also provided by the T3 trigger.

[2] Before arriving at the ADC module, the signal went through two additional modules viz. a summing module, and a filter before the delay. These modules were part of the setup for another experiment (G_E^n) [60], with which we shared electronics. They had no impact on our signal processing.

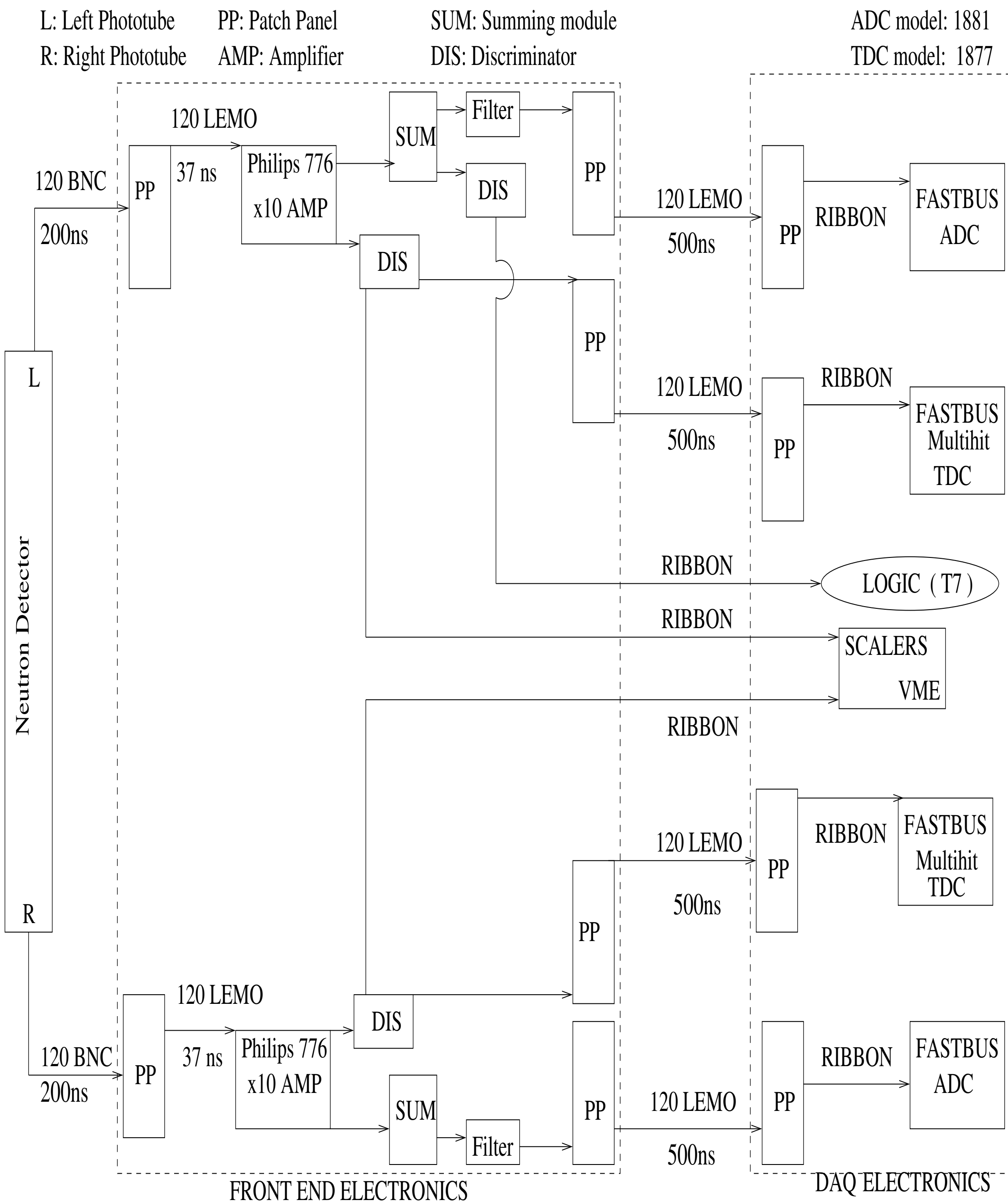

Fig. 3.14: Electronics block diagram for the neutron detector.

Chapter 4

Neutron-Detection Efficiency

The neutron-detection efficiency of a neutron detector is a crucial quantity for interpreting signals obtained from the neutron detector. If the efficiency is ϵ, and the signal without efficiency correction is S, then the signal with efficiency correction will be S/ϵ. Our primary determination of the neutron-detection efficiency was exprimental. We used the $^2\mathrm{H}(e, e'p)n$ reaction in what is commonly called "the associated particle" method. The $^2\mathrm{H}(e, e'p)$ measurement with the two HRSs is "kinematically complete," meaning that the direction and momentum of the associated neutron is determined for each e-p coincidence, from conservation of energy and momentum. The LDK0, LDK1, LDK2, and LDK3 kinematics were dedicated to these associated-particle efficiency measurements.

The efficiency data from the $^2\mathrm{H}(e, e'p)n$ reaction measurements were of only modest statistical accuracy in the neutron momentum range of interest. Therefore we developed a model simulation of the efficiency that we adjusted to provide a good description of the measured efficiency data. The basis of the simulation was a Monte-Carlo neutron-detection efficiency code [72] developed at Kent State University by R. Cecil, et al. The key parameter for extracting the efficiency from the code is the pulse-height (light production) thresholds for the scintillator bars making up the detector. Because our electronic signal processing did not correspond to the assumptions in the Cecil code, we determined "effective thresholds" for the simulation that provided a good description of our efficiency data. The simulation then gave us a smooth curve of efficiency versus neutron momentum that we used for the data analysis and interpretation.

The process of arriving at the final simulation is described in this chapter.

4.1 The Discriminator Thresholds

The neutron-detection efficiency depends on the discriminator thresholds for phototube signals, which are set in the electronics. The descriminator thresholds determine the minimum light output of the scintillator bars that is detectable. The lower the threshold the higher the efficiency.

The following plot (Fig. 4.1) was used to extract the thresholds corresponding to each scintillator bar in the various planes of the neutron detector. We used elastic runs on the hydrogen target as well as cosmic ray data in order to produce this plot (the procedure for obtaining these thresholds is described in Appendix A.1). Figure 4.1 shows that the first plane had an average threshold of 5.3 MeVee[1], the second had an average threshold of 4.4 MeVee, the third 4.7 MeVee, and the last plane had an average threshold of 7.1MeVee.

From the ^{2}H$(e,e'p)n$ reaction at low energy (2.345 GeV), we know kinematically that once the struck proton goes to the HRS, the recoil neutron must go to the neutron detector. On the other hand, this is not the case for the ^{12}C$(e,e'pn)$ reaction, since in addition to a recoiling neutron, there are additional reactions to share the available momentum and energy. Hence we can only expect a small count rate in the neutron detector from the ^{12}C$(e,e'pn)$ reaction. For this reason, we set different[2] hardware thresholds for the neutron-detector discriminators for different run periods.

[1]MeVee: unit for light production in a scintillator; ee stands for "electron equivalent." For example, 10 MeVee means light production equivalent to a 10 MeV electron. Electrons are used as a standard, because the relationship between energy loss and light production is linear for electrons. For protons and heavier particles it is non-linear, and unique to the particle species.

[2]The hardware threshold for the low energy ^{2}H$(e,e'p)n$ reaction runs was -100 mV, and that for all other production runs was -50 mV. The higher the magnitude of the hardware threshold, the lower the count rate.

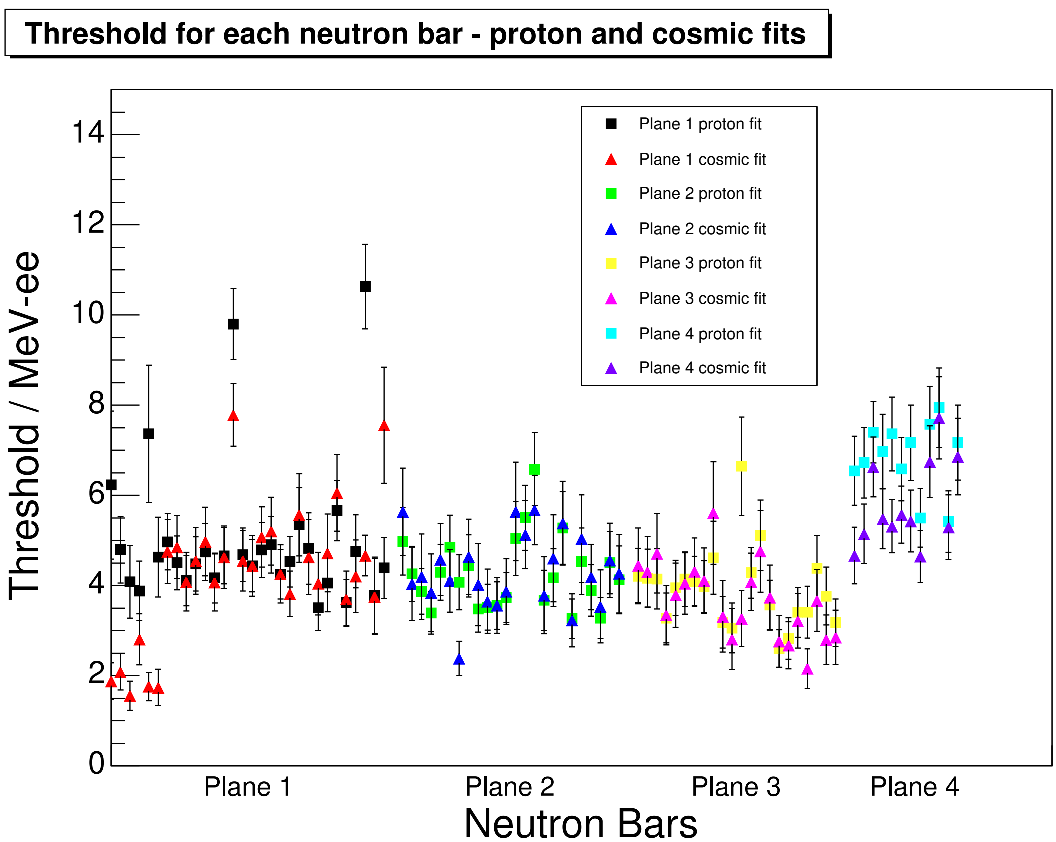

Fig. 4.1: Threshold plot for the Neutron Detector bars (figure courtesy: Peter Monaghan). The "proton fit" is data obtained from elastic runs on the hydrogen target, and the "cosmic fit" is data obtained from cosmic ray data. The two results agree in general. See Appendix A for a discussion of how these were obtained

All high energy (4.627 GeV) data had the neutron-detector discriminator threshold at -50 mV. The thresholds in MeVee mentioned above and plotted in Fig. 4.1 belong to this part of the experimental data. All low energy (2.345 GeV) data on liquid deuterium target were taken with a -100 mV hardware threshold.

4.2 Efficiency

We used a computer simulation code developed by R.Cecil et al [72] to model the neutron-detection efficiency of a scintillator bar. Note that the neutron-detection efficiency from the simulation assumes that the neutron flux is incident on the neutron counter without any attenuation. But in the actual experiment we had various materials between the target, where the neutrons are produced, and the neutron detector. Hence we had to consider two things in order to use the simulation code to get the efficiency: (1) neutron-detection efficiency with no transmittance correction and (2) the neutron transmittance for the materials present between the target and the neutron counter. In practice, these two quantities are multiplied together to give the overall neutron-detection efficiency.

When we ran the Cecil code [72] and considered the output corresponding to the average thresholds discussed in Sect.4.1, the simulated efficiencies were substantially larger than the measured ones. This is not surprizing, since the discriminator thresholds do not really correspond to what is in the computer model. The problem comes from the length of the scintillator bars. The light attenuation length in the plastic scintillator is on the order of a couple of meters. This means that a small signal near one end of a bar may produce a signal above threshold at that end, but not at the other end. No such mechanisim is built in the Cecil code, which assumes that all events “above threshold” produce recorded events. In practice, the Kent

State group has found that a software data replay threshold on the ADC signals, close to twice the hardware thresholds, is required for measured detection efficiencies to agree with calculated ones.

When comparing our measured efficiencies from the $^{2}\mathrm{H}(e, e'p)n$ reaction with those calculated with the Cecil code, we found that good agreement was obtained when "effective thresholds" were 80% larger than the hardware thresholds, and that is what we have chosen to use. Thus the effective thresholds are 9.5, 7.9, 7.6, and 12.8 MeVee for planes 1, 2, 3, and 4 of the neutron detector, respectively.

Shown in Fig. 4.2 are typical efficiency plots obtained from the simulation code for the effective thresholds. What is plotted here is the efficiency of a scintillator bar versus the kinetic energy of the neutrons. The efficiency indicates how many neutrons are detected out of the total incident neutron flux on the scintillator bar. The peak between 40 to 60 MeV for the plots in Fig. 4.2 indicates the onset of reactions on carbon. Below the peaks n-p elastic scattering dominates the efficiency while above the peak ^{12}C reaction channels open up and dominate the efficiency. Note that the code does not care about the history of the neutron flight before it hits the counter. This means that in order to know the history, for example, what fraction of the neutrons were removed from the flux due to an absorbing material present in front of the scintillator bar, one has to know the neutron transmittance of the absorber as described below.

4.3 Transmittance

Determining how many neutrons are headed towards the neutron detector depends upon what fraction of the neutrons are absorbed or scattered in the material between the target and the neutron detector. The transmittance (T) of the neutron

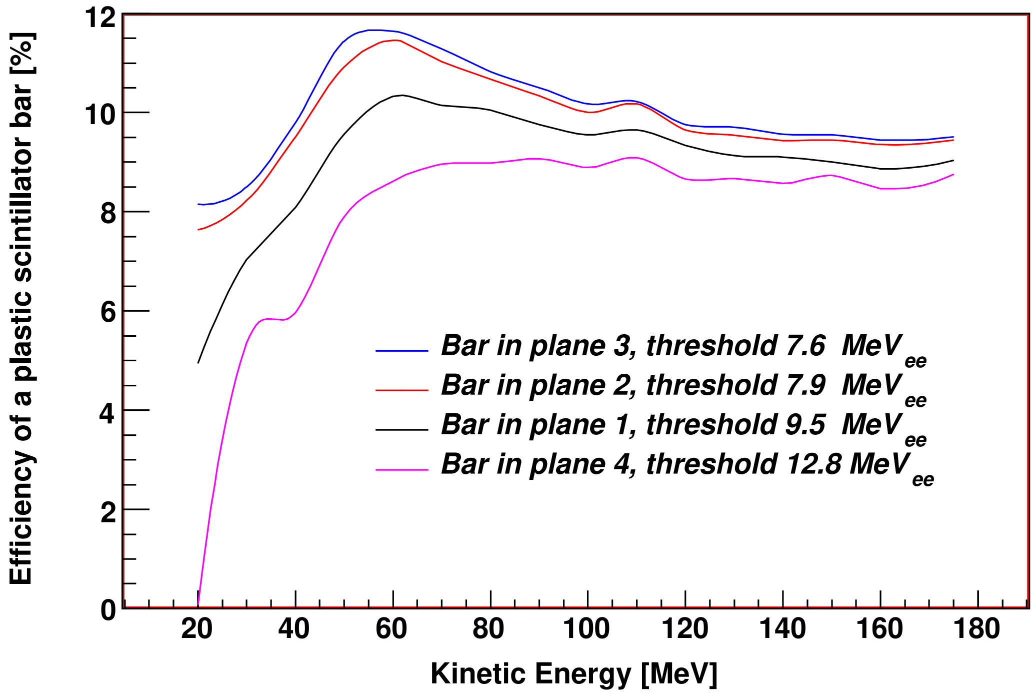

Fig. 4.2: Efficiency versus kinetic energy plots for the plastic scintillator bars (data for this plot are given in Table A.1 in Appendix A.2).

flux through a specific material is given by the expression:

$$T = e^{-\sigma n L} \tag{4.1}$$

where σ is removal cross section for a neutron in that material, n is number density of the material, which is $N.\rho/A$, and L is the thickness of the material. Here N is Avogadro number, ρ is density of the material, and A is atomic weight of the material .

The "removal cross section" is the probability that a neutron will be removed from the flux, i.e., the neutron will not be detected by the neutron detector. Removal cross sections cannot be obtained directly from a cross section table since the probability for removal depends on the distance of the detector from the target and the intervening medium which can remove neutrons from the beam. If the medium is close to the target and far from the detector then the total cross section can contribute to the removal cross section. By contrast the space between the back face of lead wall and the front face of neutron detector was only 56 cm and the neutron detector was sitting 6.04 m from the target. Thus the total cross section for neutrons in lead wall did not contribute to the removal cross section.

The total cross section is given as the sum of the elastic cross section and the non-elastic cross section. The non-elastic cross section is not an inelastic cross section in that it includes all the reaction channels. The elastic cross section peaks strongly near 0° about the beam direction.

We define the removal cross section as the "non-elastic" cross section plus a fraction of the elastic cross section appropriate to the location of a specific material between the target and the detector. If the material is close to the detector (like the lead wall) then almost all elastically scattered neutrons will strike the detector,

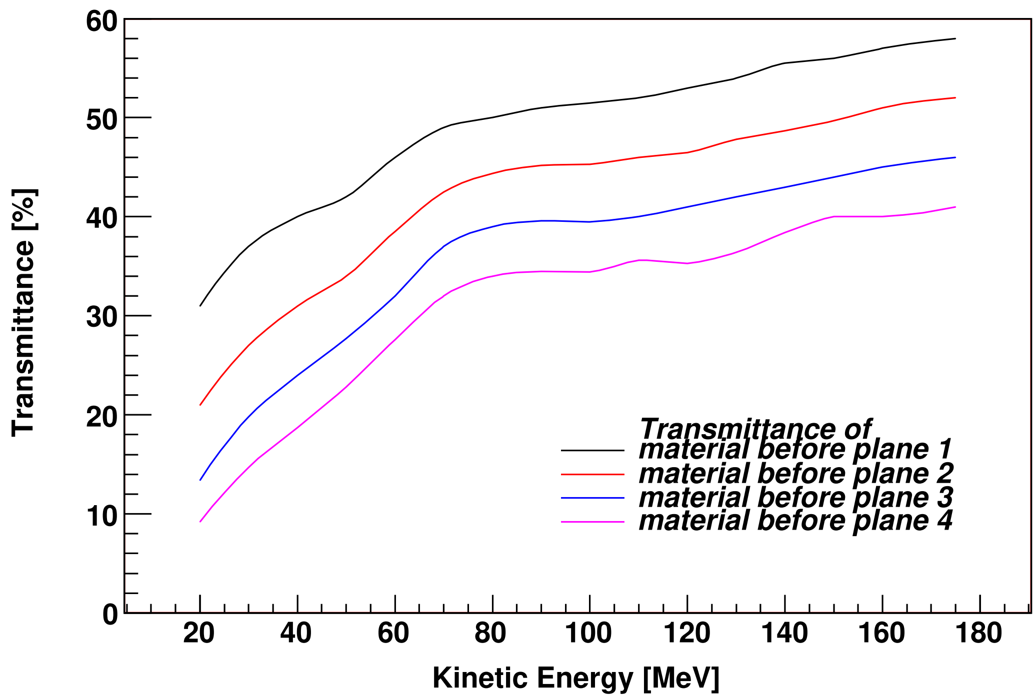

Fig. 4.3: Neutron transmittance versus kinetic energy for different material combinations (data for this figure are given in Table A.4 in Appendix A.2).

because the elastic cross section peaks sharply around 0°. But if the material is far from the detector, then some fraction of the elastically scattered neutrons will miss the detector.

The non-elastic cross section can be obtained from a cross-section table [73] . For hydrogen, the non-elastic cross section involves pion production or Δ excitation and decay, and radically changes the neutron energy. We defined the removal cross section for hydrogen as two third of the total cross section. We needed hydrogen cross sections to determine the transmittance of plastic scintillator which is made up of hydrogen and carbon in the H to C ratio 1.104. The removal cross section data used in this analysis are shown in Table A.2 in Appendix A.2.

We had 600 cm of air, 4 cm of veto counters (the overlap of two 2 cm paddles), 3.55 cm of BigBite plastic scintillators and 9.08 cm of lead wall (made up of 4 cm thick iron and 5.08 cm thick lead) between the target and the front face of the first plane of the neutron detector. We assumed that the total cross section of none of these materials contributed to the removal cross section. To calculate the total transmittance of neutrons we use the following relation.

$$T_{total} = e_{air}^{-\sigma nL} \; . \; e_{plastic}^{-\sigma nL} \; . \; e_{Fe}^{-\sigma nL} \; . \; e_{Pb}^{-\sigma nL} \tag{4.2}$$

We assumed that the uncertainty $\Delta\sigma$ in a given removal cross section was

$$\triangle\sigma = \sigma/4. \tag{4.3}$$

We then find the error in T_{total}, assuming no error in nL, as

$$\triangle T_{total} = T_{total} \, \frac{1}{4} \, \sqrt{(\sigma nL)^2_{air} + (\sigma nL)^2_{plastic} + (\sigma nL)^2_{Fe} + (\sigma nL)^2_{Pb}} \tag{4.4}$$

Shown in Fig. 4.3 are typical plots showing the total transmittance of the various materials between the target and the front face of different planes of the neutron detector. The error in transmittance is about ± 5% due to an uncertainty of ±25% [74] in the removal cross sections.

4.4 Detection Efficiency

We define a product of Transmittance (T) and the calculated (Monte-Carlo code [72]) efficiency (ε_b) of a scintillator bar in a plane of the neutron detector as the neutron-detection efficiency (ε_p) for that plane :

$$\varepsilon_p = \varepsilon_b \, T, \tag{4.5}$$

with uncertainty

$$\triangle\varepsilon_p = \varepsilon_p \, . \, \sqrt{(\frac{\triangle\varepsilon_b}{\varepsilon_b})^2 + (\frac{\triangle T}{T})^2}. \tag{4.6}$$

When we add this quantity for all four planes, this will be the neutron-detection efficiency (ϵ) for the entire neutron detector:

$$\epsilon = \varepsilon_{p1} + \varepsilon_{p2} + \varepsilon_{p3} + \varepsilon_{p4} \tag{4.7}$$

with uncertainty

$$\triangle\epsilon = \sqrt{\varepsilon_{p1}^2 + \varepsilon_{p2}^2 + \varepsilon_{p3}^2 + \varepsilon_{p4}^2} \tag{4.8}$$

Shown in Fig. 4.4 as a green curve is detection efficiency of the neutron detector as a function of neutron kinetic energy. The other curves are the efficiencies for the individual planes. Data for this figure are presented in Table A.5 in Appendix A.2. The procedure for calculation of detection efficiency as shown in Fig. 4.4 is the

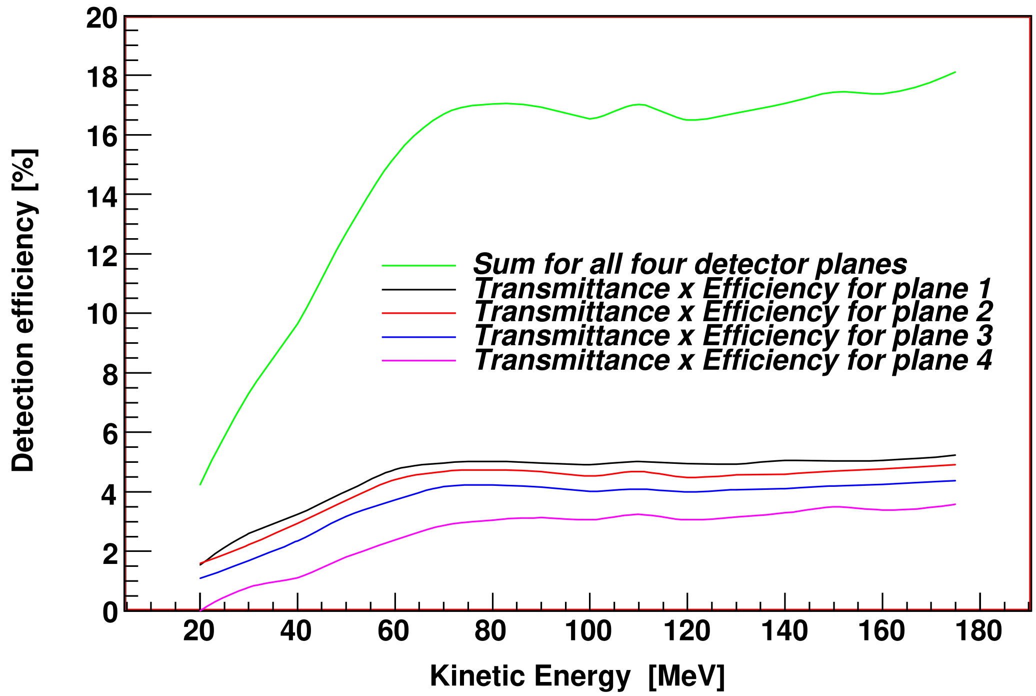

Fig. 4.4: Detection efficiency versus kinetic energy plots for the Neutron Detector.

following.

1. Plane 1: Product of efficiency of one bar in plane 1 and the transmittance of air, lead wall and plastic of thickness 7.55 cm (plastic from the BigBite bars + veto paddles). The veto thickness is taken as 4 cm for this purpose due to the overlap of two veto paddles, each 2 cm thick, in the middle.

2. Plane 2: Product of efficiency of one bar in plane 2 and the transmittance of air, lead wall and plastic of thickness 17.55 cm (plastic from the BigBite bars + veto paddles + a bar in plane 1).

3. Plane 3: Product of efficiency of one bar in plane 3 and the transmittance of air, lead wall and plastic of thickness 27.55 cm (plastic from the BigBite bars + veto paddles + a bar in plane 1+ a bar in plane 2).

4. Plane 4: Product of efficiency of one bar in plane 4 and the transmittance of air, lead wall and plastic of thickness 37.55 cm (plastic from the BigBite bars + veto paddles + a bar in plane 1+ a bar in plane 2 + a bar in plane 3).

The neutron-detection efficiency for the neutron detector is the sum of the values obtained in the four steps mentioned above.

4.5 Conclusion

Shown in Fig. 4.5 are the data points for the measured efficiency plotted with the smooth curves for the simulated efficiency calculated for the "effective" thresholds. The data for these plots are given in Table A.6 in Appendix A.2. The blue data points, and the green data points were obtained from the 2-pass (2.345 GeV), and 4-pass (4.6275 GeV) liquid deuterium runs, respectively. Similarly the blue, and the green simulated curves correspond to the 2-pass, and 4-pass liquid deuterium runs, respectively.

The determination of the effective threshold values for the efficiency look-up table generated from the Monte-Carlo code was guided by the blue data points: the effective thresholds for the blue curve were chosen to describe these points well. The effective theresholds for the green curve were obtained by taking half of the threshold values used for the blue curve.

The four (green) data points for the green curve checked the consistency of simulation with the calibration data, which had only modest statistics at 4.6275 GeV. Based on this analysis, we can describe the average neutron-detection efficiency as 16.5± 2.8 % for the high energy (4.6275 GeV) data[3].

[3]The 4-pass data on liquid deuterium and carbon were taken at almost identical kinematic settings.

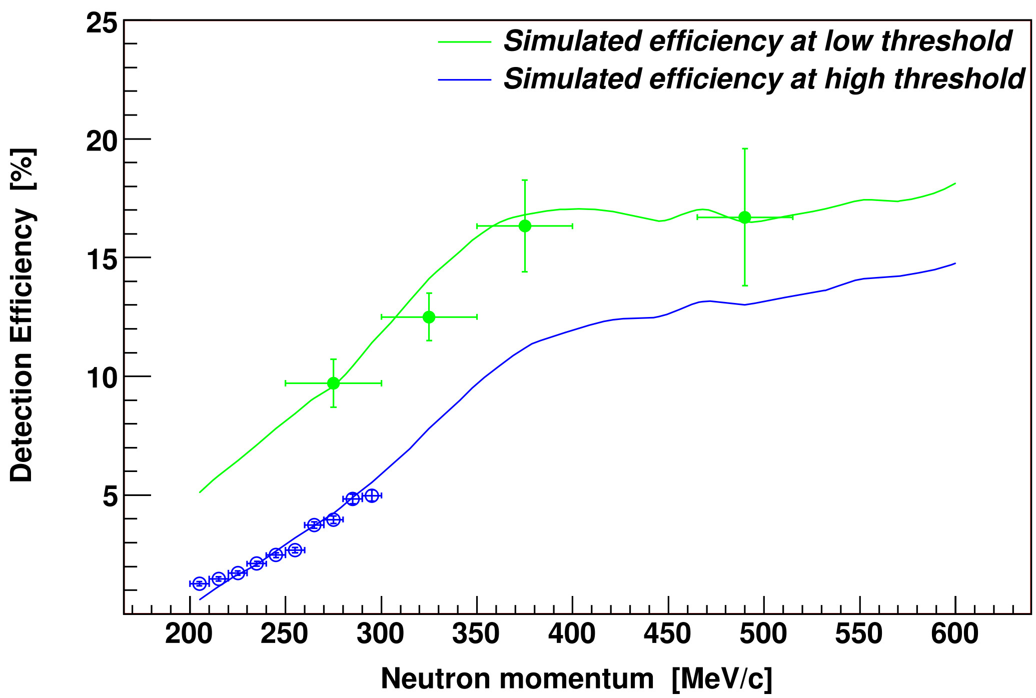

Fig. 4.5: Detection efficiency versus momentum plots. Data points are from the experiment while the smooth curves are from the simulation. The green curve is for the 4-pass (4.627 GeV) beam and the blue curve is for the 2-pass (2.345 GeV) beam.

Chapter 5

Data Analysis-I: The HRSs and BigBite

In this and the next chapter we describe the data analysis methods used in the present work. The data replay code used in this analysis was the C^{++}-based Hall A analyzer code [75] (henceforth called *analyzer*) which was based on CERN's ROOT-package [76]. We introduced the BigBite library into the *analyzer* in order to incorporate newly added detectors such as the BigBite detector and the neutron detector for this experiment.

In the HRSs, the particle tracks were measured in the focal plane. These particle trajectories were traced back to the target to obtain the interaction vertex (θ_{tgt}, ϕ_{tgt}, y_{tgt}, $\delta p/p$) through the use of the VDC matrix elements incorporated in database files of the *analyzer*. All physical quantities were described in terms of the laboratory coordinate system.

5.1 Particle Identification in the HRSs

5.1.1 The Left High-Resolution Spectrometer (HRSL)

The electron signal was very clean in the HRSL. Only a coincidence time cut and a spectrometer acceptance cut were required to identify electrons cleanly. For a simple cross check, we used the pion rejector to reject pions and the gas Cherenkov detector to identify electrons. The cuts for these detectors were not used for the present analysis because they did not change the strength of the signal or background.

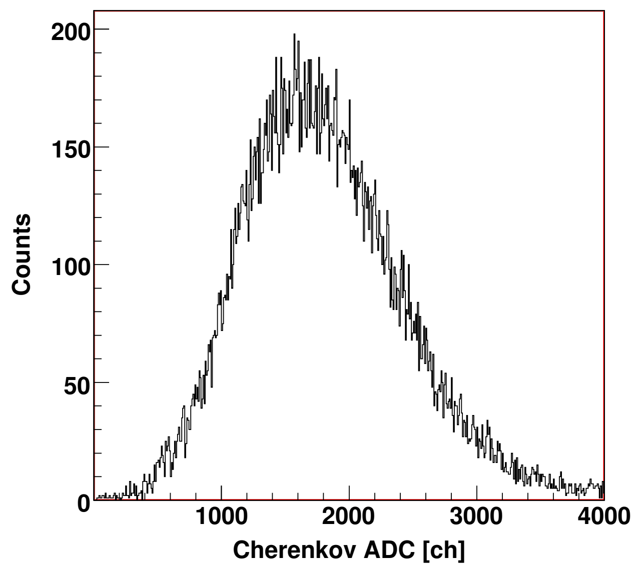

Fig. 5.1: The ADC sum for the gas Cherenkov detector in the HRSL.

Figure 5.1 shows the ADC signal from the CK3 production run kinematics in the form of the ADC sum of all ten mirrors of the gas Cherenkov detector. All signals were due to electrons. Had there been any pions detected in this detector, they would have appeared below the channel 500.

Figure 5.2 shows the pion rejector signal from the CK3 production run kinematics. A small cluster of events close to the front left corner are pions. This shows that the pion contamination was very small in the data. When combined with the other cuts used in the main physics analysis of triple-coincidence events, using or not using a pion rejector cut did not change anything in the triple-coincidence signal (or in the random background). For this reason, we did not use a pion rejector cut in the main analysis.

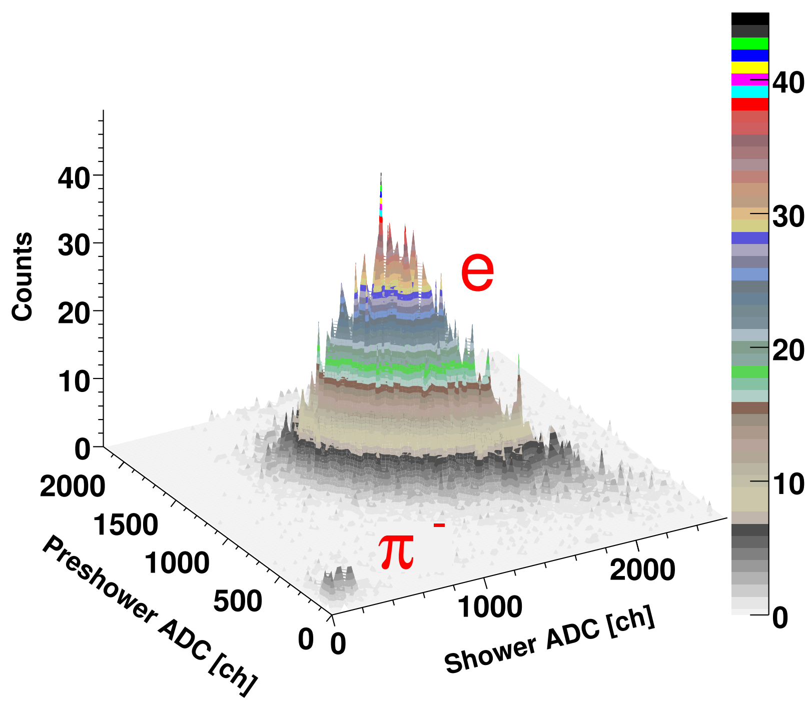

Fig. 5.2: The pion rejector (preshower and shower detectors) signal in the left high-resolution spectrometer, showing the separation of electrons from pions. The number of pions is negligible.

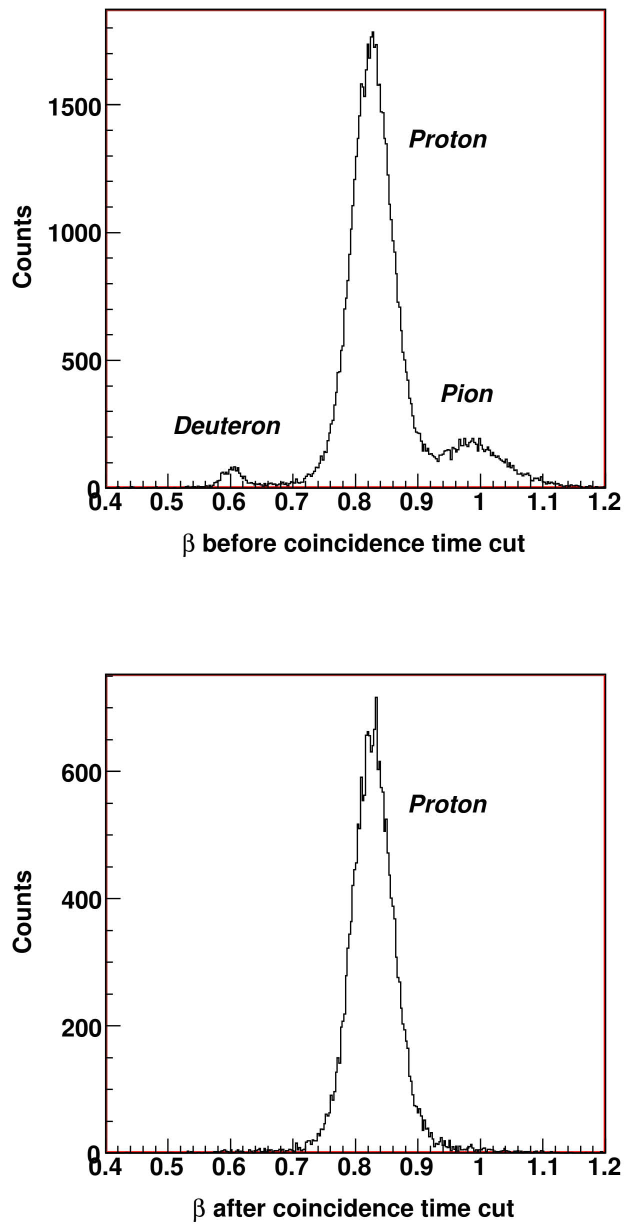

Fig. 5.3: Spectrum of β in the HRSR: with (bottom) and without (top) the coincidence time cut.

The Right High Resolution Spectrometer (HRSR)

The HRSR did not have any dedicated particle-identification detectors, so we had to identify protons using the time-of-filght between the two scintillator planes (S1 and S2). The time-of-flight was converted to β, the speed of a particle in units of c, the speed of light. As seen on the top part of Fig. 5.3, signals due to deuterons, protons and pions are clearly evident. A clean proton signal was obtained after applying the coincidence time cut (Sect.5.2) which removed the deuterons and pions (see the bottom part of Fig. 5.3). Thus after using the coincidence-time cut we did not have to use a β-cut in the physics anaysis. The β plot in Fig. 5.3 is from the CK3 kinematics. After using the coincidence-time cut, no pion or deuteron contamination was observed in other kinematics either.

5.2 Coincidence Time

The time-of-flight difference for coincident particles in the HRSL and the HRSR is called the coincidence time. A real coincidence event involves two particles emerging from the target at the same instant, thus producing a narrow peak in the time-of-flight spectrum (see Fig. 5.4). An accidental coincidence event is caused by two uncorrelated single-arm events which fall within the coincidence timing window contributing to the continuous flat background in the time-of-flight spectrum in Fig. 5.4.

The coincidence time for double-coincidence A$(e, e'p)$ events is the main basis of the analysis of the triple-coincidence A$(e, e'pn)$ reaction. For this reason we paid special attention to calibrating the timing of the scintillator paddles of the two scintillator planes in each HRS to get as narrow a coincidence time peak as possible. The optimization tools for the HRS coincidence time have been well established [77] due to the completion of numerous coincidence experiments in Hall A.

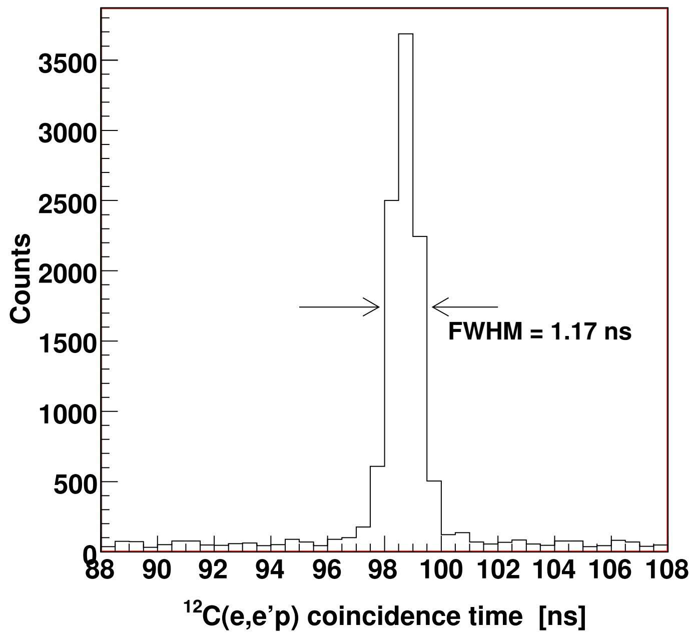

Fig. 5.4: Spectrum of the coincidence time for the CK3 kinematics. Note that the flat backgound is almost negligible.

The following were the important steps carried out to optimize the coincidence time resolution. The results of the optimization were quantified and included in the relevant data-bases of the analyzer.

- Align the time difference of the right and left TDCs to zero (ns) for all paddles in all planes by introducing scintillator timing offsets.

- Compute the particle speed in a paddle for particles with different masses. If the left (right) HRS is set for electron (proton) detection then one has to calculate electron (proton) speed through the scintillator plastic in the S1 and S2 planes of the left (right) HRS.

- Compute the timewalk for each paddle in each plane in each HRS. Since the timing signal comes from a fixed threshold discriminator, the time between the start of the signal and the time that the threshold is exceeded depends on the height of signal from the individual paddle.

We were able to establish the coincidence time resolution with full width at half maximum (FWHM) of 1.17 ns (σ was slightly less than 0.5 ns). This value was generally the same for all kinematics of the present experiment.

5.3 Software Cuts

Both HRSs had certain nominal acceptances for the in-plane angle (ϕ), out-of-plane angle (θ), and fractional momentum ($\frac{dp}{p}$). These values were $\pm$30 mr, $\pm$60 mr and $\pm$0.045, respectively [53]; Fig. 5.5 illustrates these ranges for data from the CK3 kinematics. For the coincidence time cut we used $\pm$2.5 ns about 99 ns (see Fig. 5.4). All these acceptance cuts and the coincidence time cut were a common set of cuts for all kinematics throughout the data analysis.

We also used some kinematics dependent cuts, such as cuts in missing momentum, missing energy, and some acceptance angles for the neutron detector determined by using the missing momentum. The later two cuts, as shown in Fig. 5.6, were used to remove events with pions and Δ's. Choosing the missing energy less than 250 MeV, or choosing the in-plane angle (calculated by using the missing momentum) smaller than -88.0° gave identical results for the CK3 kinematics as depicted on the bottom panel of Fig. 5.6. This is also shown in Fig. 5.7. In this figure using the $\Phi_{pmiss} < -88°$ cut gives the red trace (top panel) in the missing energy spectrum, while using missing energy < 250 MeV gave the blue trace (bottom panel) in the Φ_{pmiss} spectrum. The strength of the signal in both the red and the blue traces was identical. The vertical dotted lines in Fig 5.7 show where the missing energy (250 MeV) and the Φ_{pmiss} ($-88°$) cuts would lie. It takes about 30

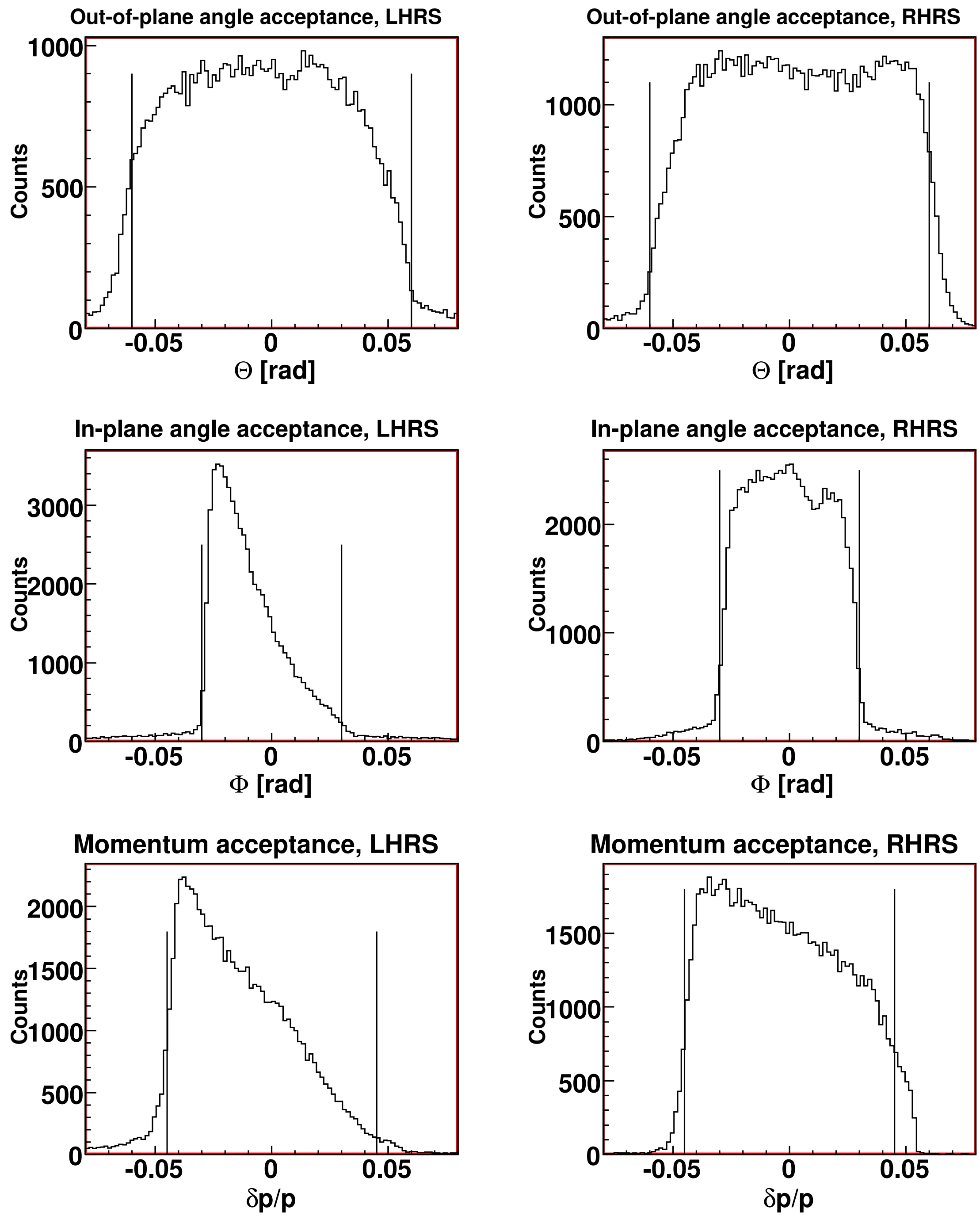

Fig. 5.5: Nominal acceptance of the HRSs. The left column is for the HRSL and the right column is for the HRSR. The two vertical lines in each plot are the acceptance cuts. The events outside these lines were not included in further analysis.

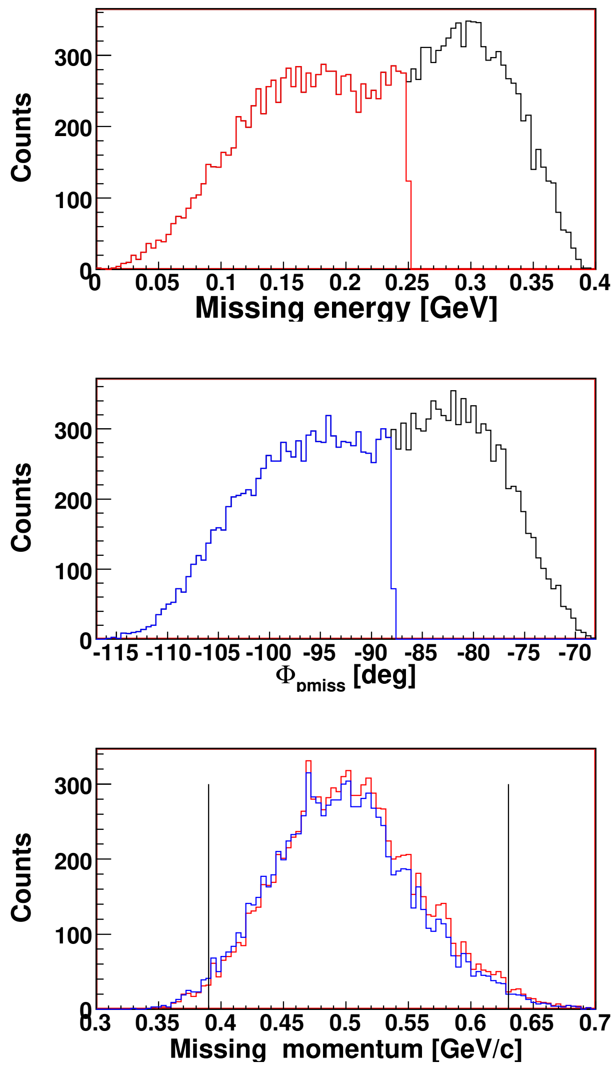

Fig. 5.6: Two redundant cuts to remove events with pions and Δ's in CK3 kinematics. In the top plot, the red trace shows a missing energy cut which gives the same number of physics events as given by the blue trace in the middle plot. The middle plot is the in-plane acceptance angle for the neutron detector calculated by using the missing momentum. The third plot shows the missing momentum spectrum using the red and blue contributions (as matched by color coding) from the upper two plots. The black traces shown in the upper two plots correspond to pion and Δ contribution in the data. The two vertical lines in the third plot enclose the events used in the analysis of the data from CK3 kinematics.

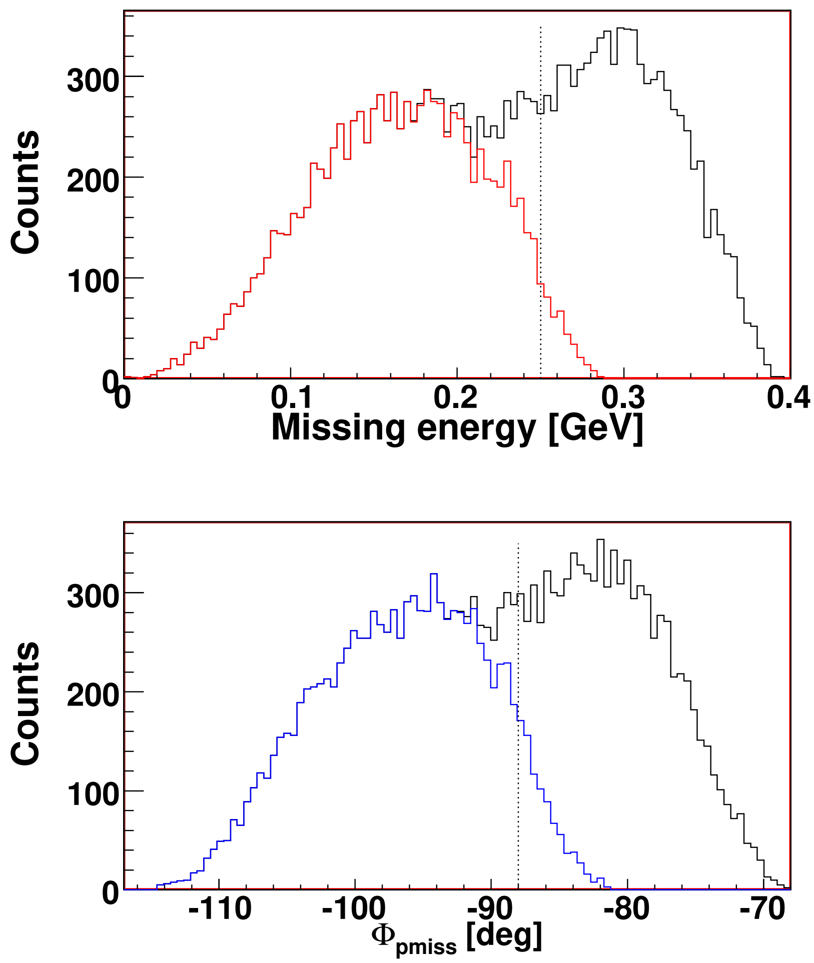

Fig. 5.7: Shown on the top is a missing-energy plot. The red trace uses the $\Phi_{pmiss} < -88°$ cut. The vertical dotted line passes through the missing energy value 250 MeV. The bottom plot is a Φ_{pmiss} plot and the blue trace uses missing energy cut < 250 MeV. The vertical dotted line passes through the Φ_{pmiss} value -88°. Both red and blue traces contain identical signal strength and the integral of either one of such strengths was used in the analysis.

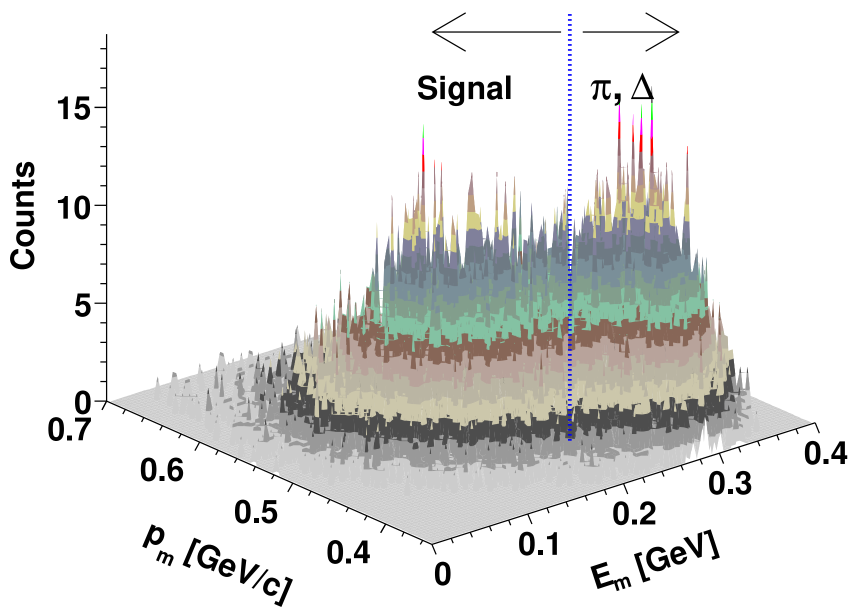

Fig. 5.8: Missing momentum versus missing energy for the ^{12}C$(e, e'p)$ reaction. The vertical dotted line (at missing energy = 0.25 GeV) separetes the events with pions and Δ's.

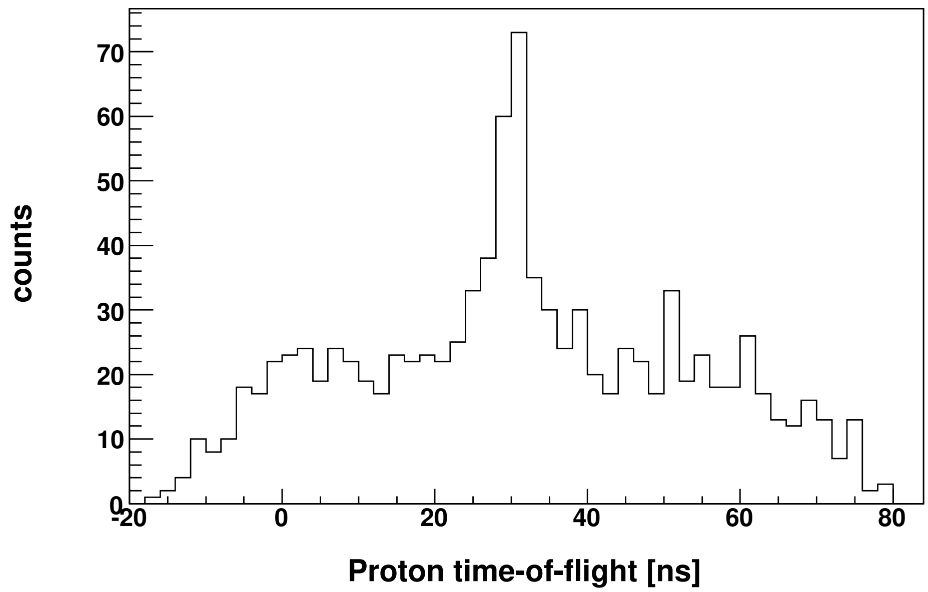

Fig. 5.9: The time-of-flight spectrum for particles detected with the BigBite detector. The peak around 30 ns is for triple-coincidence protons from the ^{12}C$(e, e'pp)$ reaction.

to 80 MeV to remove two nucleons simultaneously from a carbon nucleus and an extra 140 MeV to create the lightest pion. Hence the upper limit of missing energy cut as 250 MeV would be a reasonable value in order to reject pions and Δ particles.

As a final illustration, a missing momentum versus missing energy plot for the reaction ^{12}C$(e, e'p)$ is shown in Fig. 5.8. This figure also shows how pions and Δ's were visible and could be seperated from the signal. The vertical dotted line (at missing energy $= 0.25$ GeV) separates the desired signal from pion and Δ production.

5.4 Detection of Recoiling Protons

Various methods of momentum reconstruction have been applied [69] for the proton tracks observed in the BigBite detector. Of these methods, the time-of-flight from the target to the E-plane of the BigBite detctor was found to be the most effective way to reconstruct the proton signal. Shown in Fig. 5.9 is a typical time-of-flight plot for recoiling protons from the ^{12}C$(e, e'pp)$ reaction . The pronuounced peak at about 30 ns is due to the protons detected by BigBite in triple-coincidence in the CK3 kinematics. This shows direct evidence of short-range correlations for p-p pairs in the reaction ^{12}C$(e, e'pp)$. See [69] for further details about the study of NN short-range correlations via ^{12}C$(e, e'pp)$ reaction based on experiment E01-015.

Chapter 6

Data Analysis-II: Neutron Analysis

The primary focus of the research for this dissertation is detection of the recoiling neutrons, and the search for NN short-range correlations of such neutrons with the struck-protons from the $^{12}\mathrm{C}(e, e'pn)$ reaction. In this section we describe how we calibrated the neutron detector and used it to identify the recoiling neutrons and measure their momenta.

6.1 Detector Calibration

Since neutrons are neutral particles, there are two aspects to their detection that require considerable care. First, neutrons are not detected directly; we detect secondary charged particles from their interactions with the H and C nuclei in the scintillator bars. This means that the amount of energy deposited in a scintillator bar, and the scintillation light produced, does not give a direct measure of the energy (or momentum) of the neutron. Rather, a monoenergetic flux of neutrons will produce a spectrum of light production, the maximum output corresponding to when a neutron has transferred all of its energy to a proton. This will happen only in a head on collision (180° scattering in the center-of-mass system) with the proton in an ^{1}H atom. The fraction of the light production spectrum that we capture depends on the minimum light output that our electronics or software will accept from the phototubes (PMTs). This fraction in turn is reflected directly in the detection efficiency of a scintillator bar. Therefore, determination of the efficiency is essential to obtaining meaningful physics results.

Second, we use plastic scintillator for neutron detectors because the time scale of the scintillation-light production, on the order of 1 ns, allows us to determine the time-of-flight (TOF) of a neutron from the target to the detector, and hence the velocity, momentum, and kinetic energy of the neutron. But this "time-of-flight" technique requires accurate knowledge of the time origin ("time zero") for the TOF spectrum. Every cable and every electronics module (even including PMT transit times) that the signal from a PMT passes through introduces a delay in that signal, hence accurate determination of "time zero" is essential.

To calibrate "time zero" and the efficiency of the neutron detector, we utilized what is called the "associated particle" technique. In this technique, kinematics dictate that for every particle detected in a primary detector (the HRSs for this experiment) there must be, a priori, a particle passing through the neutron detector. We used two reactions in this manner to calibrate the neutron detector: $^1\mathrm{H}(e,e')p$ (e-p elastic scattering), and the $^2\mathrm{H}(e,e'p)n$ reaction. The following sections describe how we used these two reactions to calibrate the neutron detector. This involved determining the gains and relative timing of the 176 PMTs for the 88 scintillator bars.

6.1.1 TDC Alignment

The most important thing about neutron detection using the time-of-flight method was to make sure that each scintillator bar in the neutron detector had TDC-signals from both PMTs. To ensure this, we took a few $^1\mathrm{H}(e,e')p$ elastic-hydrogen runs (LH kinematics) making sure that the neutron detector was fully illuminated by the recoiling protons; the scattered electrons went to HRSL. Using data from such runs, we aligned the TDC spectra for each PMT by introducing an offset in the raw TDC value, these offsets were placed in the data base of the analysis code. The accuracy of the alignment of individual TDCs was not important, since the time-of-flight measurement of the neutrons was not directly related to these offsets. The reason is that the sum of left and right TDCs went into the time-of-flight expression. We had also to align the later quantity independent of the individual TDC alignment. Hence we alligned each TDC to appear in a small time window of a few nanoseconds. As an example, Fig. 6.1 shows the result of such alignment for the right TDCs of plane four (all other planes show the similar result); all TDC spectra are confined to a window of about 60 channels which corresponds to a time window of 30 ns (a channel was equal to 0.5 ns for the neutron detector TDCs).

6.1.2 Bar-Length Alignment

The difference between the left and right TDCs is related to the length of a scintillator bar (the y-position in a bar). Each bar in the neutron detector was one meter long. The purpose[1] of the alignment was to observe the y-position as one meter by introducing appropriate offsets and scale parameters to the TDC difference of the left and right PMTs, and to place all histograms in the same position (preferably a zero position). These offsets and scale parameters were then recorded in the data base of the analysis code.

Ideally the y-position is given [78] as

$$y = \frac{v}{2}(T_L - T_R) \tag{6.1}$$

where v is light speed in the scintillator material and T_L (T_R) is the left (right) TDC

[1] We need y-position to calculate the distance between the target and the neutron-hit position in the scintillator bar. This distance is necessary to reconstruct the neutron momentum from the neutron TOF.

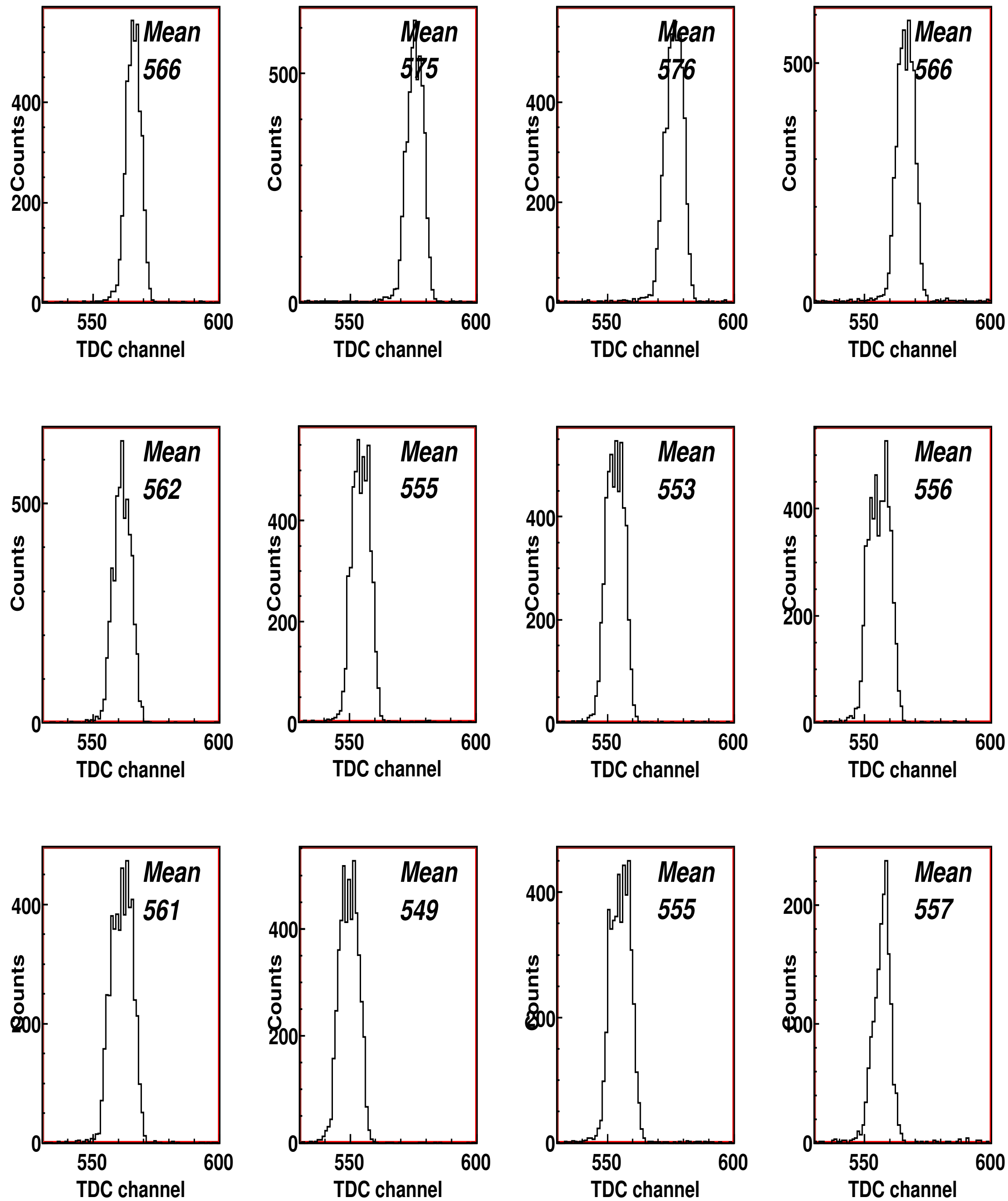

Fig. 6.1: Alignment of the neutron counter TDCs. Shown are the right TDCs of the fourth plane of the neutron detector. Data from elastic hydrogen runs were used where the protons from the ${}^{1}\mathrm{H}(e,e')p$ reaction went to the neutron detector. The TDC peaks all fall within a window of 60 channels or 30 ns. The spectra for all other TDCs were similar.

value. But due to various connecting wires and delays this equation turns out to be

$$y = S(\frac{v}{2}(T_L - T_R) + C) \tag{6.2}$$

where C is a position-offset and S is a position-scale parameter. The parameter C makes $(\frac{v}{2}(T_L - T_R) + C)$ centered at zero and the parameter S either expands or contracts $(\frac{v}{2}(T_L - T_R) + C)$ to make the y-position spectrum equal to the bar length (1.0 m in this case).

When calibrating or measuring the position spectrum, v (the speed of light in material $= c/n$) is never the correct value. It would be, if all scintillation photons travelled straight to the PMT. But most of them are actually reflected at some point, giving a longer path length. In essence, the product of S and v gives the speed for a "light pulse" involving many photons, some direct and some reflected.

For y-positon alignment we could use any production runs since the TDC alignment had already been done using elastic hydrogen runs. An example of such alignment is shown in Fig. 6.2 and it can be observed from the figure that each histogram is constrained to $\pm$ 50 cm, the physical length of the bar.

6.2 Neutron Identification

The pulse-height and timing of a neutron signal in a scintillator bar are not sufficient to distinguish neutrons from charged particles. Neutrons do not produce signals in a scintillator themselves; they scatter off of protons or react with a nucleus yielding energetic protons or light ions. So an event in a scintillator bar can be identified as a neutron candidate by the absence of any signal in the scintillators that are between the neutron source (the target) and scintillator bar where the event occured. For the first plane of scintillator bars, events in the veto layer served to

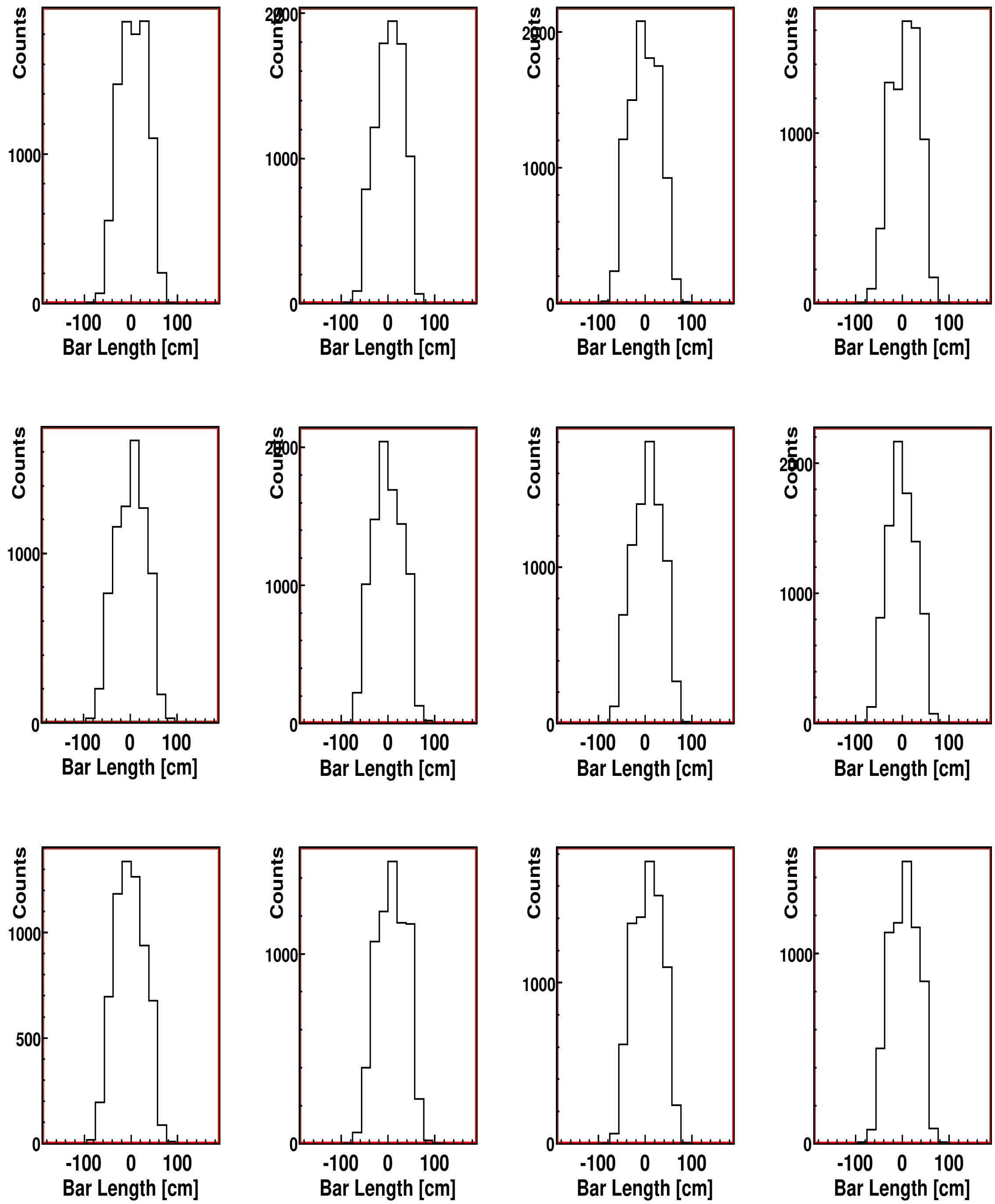

Fig. 6.2: The y-position spectra of the scintillator bars of the fourth plane. Note that each is centered at zero, and is 100 cm long, after calibration and alignment. Spectra for the other planes of the neutron detector were similar.

identify non-neutron events. In the subsequent planes, the planes of bars closer to the target constituted the "veto".

Because of high rates in the scintillator bars and veto paddles, the segmentation and timing capabilities were used to minimize accidental vetos. For each scintillator bar, all bars in the next closer plane to the target that shadow some part or all of the scintillator bar are deemed to be the "blocking bars" for that bar (see Fig. 6.3). There were two to four blocking bars for a single bar. If an event occurs in one of these blocking bars at the "same time" as the candidate neutron event, then the event is vetoed. An event is defined to be at the "same time" as another event if they occur within ±20 ns of each other.

While photons, being neutral, could also be identified as a neutron candidates, mis-identification of a photon as a neutron was unlikely in the present set-up. Photons would typically produce e^+-e^- showers in the shielding in front of the neutron detector. If some part of the shower got through the shielding, it would produce signals in the veto detectors, vetoing any events in the bars. Photons should also be easily identified as having $\beta = 1$ or $\frac{1}{v} = \frac{1}{c} = 3.3$ ns/m.

In summary, a neutron was defined as requiring an event in a bar in a plane, with no events in the two to four contiguous bars in front of it in an adjacent plane, within a time window of ±20 ns, the reference of the time window being the time of the candidate neutron event.

6.3 Time-of-Flight

Neutron time-of-flight (TOF) is the time required for the neutron to travel from the target to the point of neutron detection (about 6 m from the target). This TOF can be measured for one scintillator bar, for one plane, and for the whole neutron

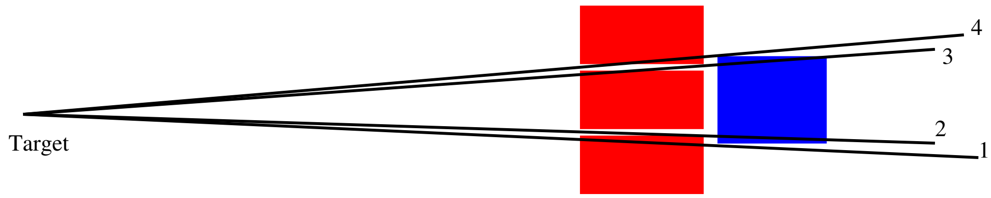

Fig. 6.3: A schematic diagram showing how the scintillator bars immediately in front of a hit-bar are used as a veto. Three red blocks represent veto counters for the scintillator bar (blue). Lines passing through the four corners of side face of the scintillator bar represent a generic acceptance of the scintillator bar. Any particle within this acceptance can hit the scintillator bar.

detector.

Instead of analyzing the neutron TOF, we analyzed the difference between the measured TOF and the predicted TOF for each neutron counter. The predicted TOF was

$$t = \frac{10}{3} d \sqrt{1 + (\frac{m}{p_m})^2} \tag{6.3}$$

which was obtained by using missing-momentum information from the A$(e, e'p)$ reaction. Here the TOF t is in nanoseconds, d is the distance of scintillator bar from the target, m is mass of neutron and p_m is the magnitude of the missing momentum for the reaction A$(e, e'p)$. The factor $\frac{10}{3}$ is $\frac{1}{c}$ where c is the speed of light in vacuum (expressed in meters per nanosecond). For the ^{2}H$(e, e'p)n$ reaction, as discussed previously, we know, a priori, from the HRS data, the momentum and hence the TOF of each detected neutron.

As a result of neutron counter calibrations we were able to observe that the peak of this TOF difference was perfectly aligned at the position about 362 ns for each bar in all planes. This is shown in Fig. 6.4 for individual bars in plane four. Though this figure is only from plane four, each plane showed similar behavior. This alignment showed that the calibration was correct. Liquid deuterium data at 2.345

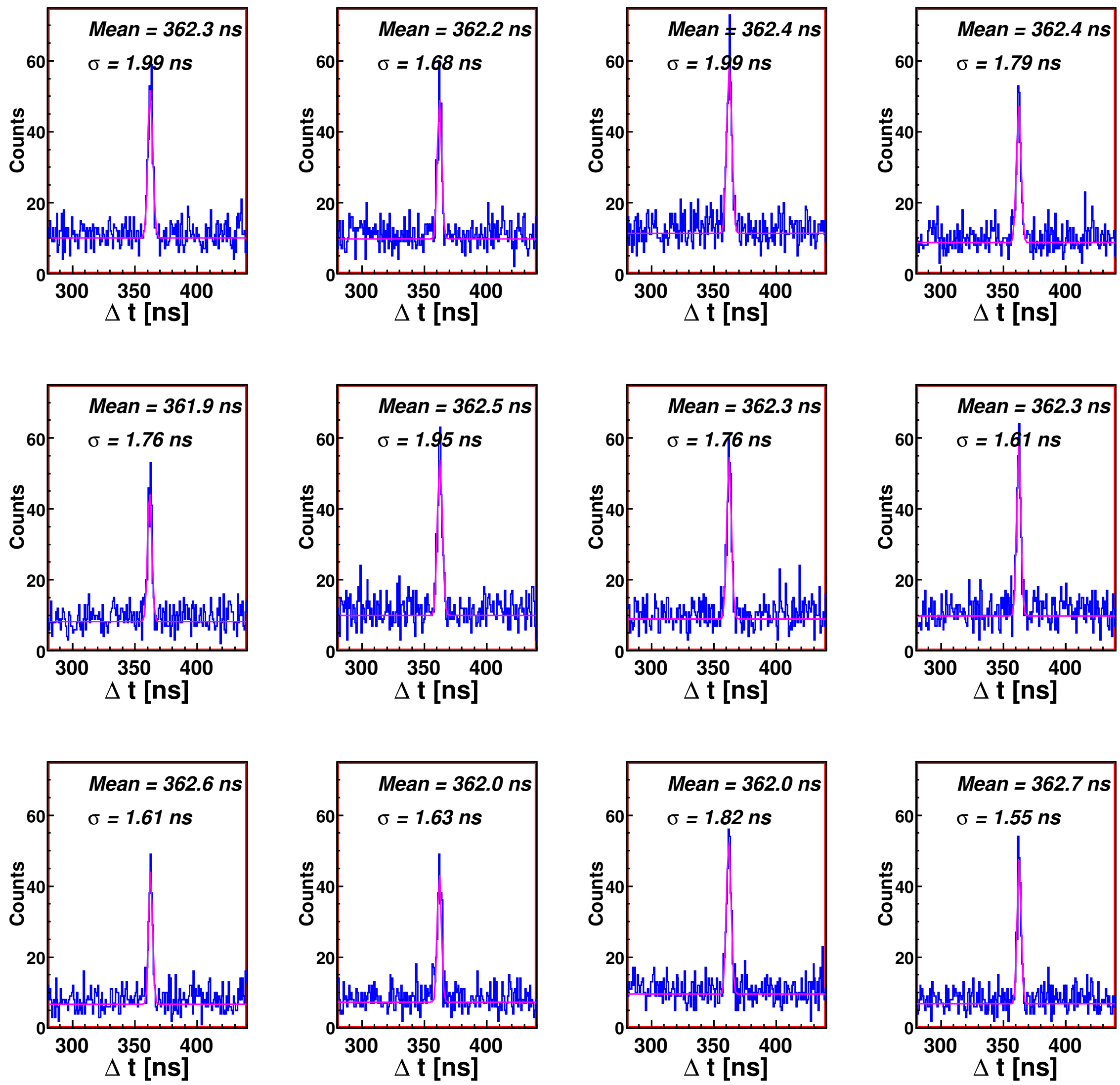

Fig. 6.4: The difference between the expected and observed time-of-flight (Δt) for individual scintillator bars using the low-energy liquid-deuterium data. Data are for the twelve bars in plane four of the neutron detector.

GeV were used for this analysis. Only with this data, were we able to observe the TOF peak in each bar. Finally, Fig. 6.5 is the TOF difference for individual planes, and Fig. 6.6 is the TOF difference for the entire neutron detector for the same data set.

The calibration constant (362 ns) was actually the zero for the time-of-flight scale for the neutron detector. This was due to the various delay cables and electronics used in the timing circuits for TDCs.

From the high-energy (4.6275 GeV) liquid-deuterium data this calibration constant was observed to be 365 ns, see Fig. 6.7. This figure was obtained from the neutron detector as a whole (unlike the case of the low-energy data where the calibration constants for individual bars were also determined). Individual scintillator bars had insufficient statistics to determine individual calibration constants for the high-energy data. The slight deviation of the high-energy calibration constant from that of the low-energy data set for the same target could be due to the low statistics. Also, a point to note is that in the case of low-energy liquid-deuterium data, the electrons and protons were detected by the HRSR and HRSL respectively; this role was interchanged for the high-energy data set. This could be one of the reasons for a small shift in the calibration constant. We took the 362 ns calibration constant as a statistically reliable one, and the 365 ns value from the high-energy data as a consistency check.

6.3.1 The Time-Of-Flight for the Liquid-Deuterium Data

Figure 6.8 is a TOF plot for the low-energy liquid-deuterium data. The TOF from target to the neutron detector was typically about 76 ns (the mean value from a Gaussian fit). The figure in the inset shows the TOF calculated using Eqn.(6.3) and provides confidence that the measured TOF was reasonable. The signal shown on

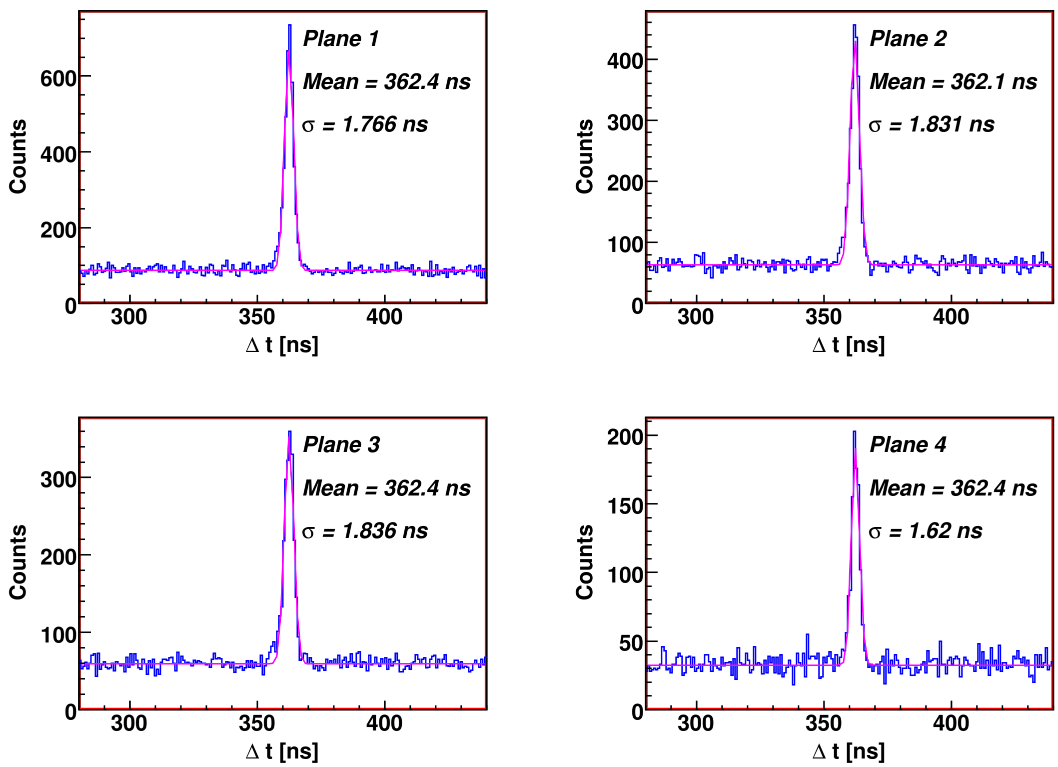

Fig. 6.5: The difference between expected and observed time-of-flight for each plane using the low-energy liquid-deuterium data.

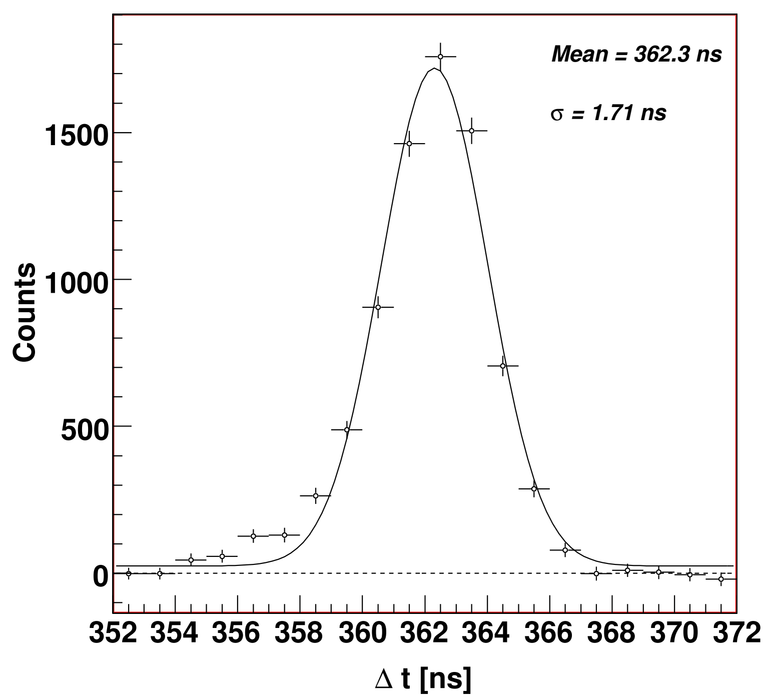

Fig. 6.6: The difference between the expected and the observed time-of-flight for the neutron detector using the low-energy liquid-deuterium data. The signal is after background subtraction. The smooth trace is a fit to the data; σ for this plot is 1.71 ns and the peak position is 362.4 ns.

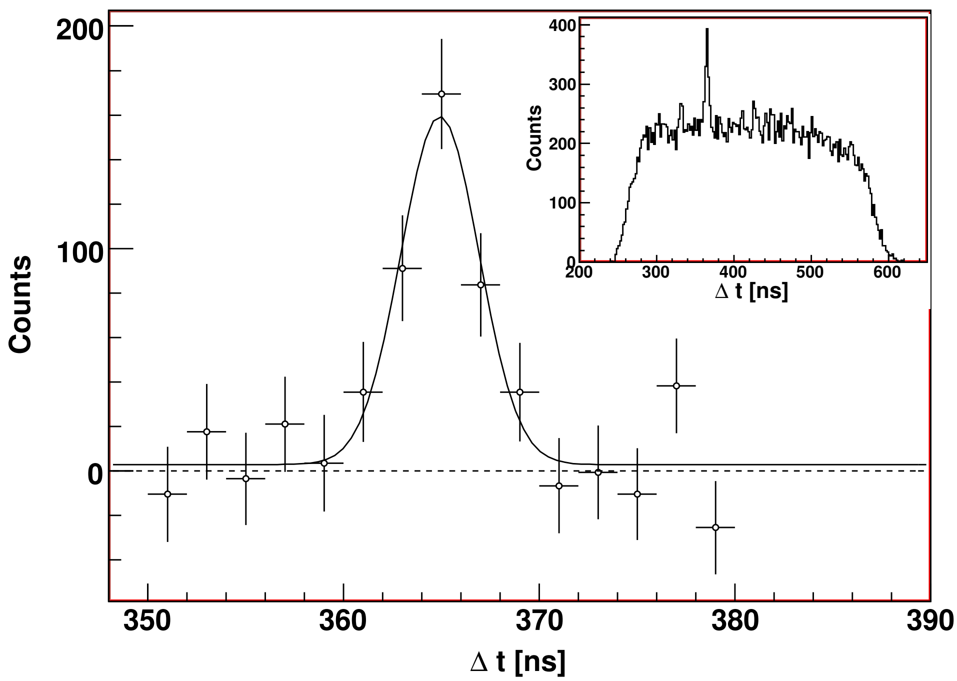

Fig. 6.7: The difference between the expected and the observed time-of-flight using the high-energy liquid-deuterium data at low missing momentum. The smooth trace is a fit to the data. The data have been background subtracted. The inset shows the data before the background subtraction. The peak position is 365 ns.

the lower panel of Fig 6.8 is background subtracted data. The signal-to-background ratio for this set, shown in the upper panel, was about 1:1.

For the high-energy liquid-deuterium data, at high missing momentum, the TOF spectrum is shown in Fig. 6.9. The typical value of 45 ns (the mean value from a Gaussian fit) is consistent with the higher neutron momentum for the higher-energy data.

6.3.2 TOF Resolution

It is clear from Fig. 6.4 that the time resolution of a scintillator bar is a little less than 2 ns. This behaviour was observed not only for individual scintillator bars but also for each plane (see Fig. 6.5), and was also true for the neutron detector as a whole (see Fig. 6.6). In any event, the time resolution (Δt) was about 1.71 ns. This is a reasonable value considering the flight-path uncertainty [74]. For neutrons, the TOF resolution is limited by the transit time of a neutron across the thickness of the scintillator bar, because we don't know where the neutron interacted along its path through the scintillator material. The time resolution could also be described in terms of the fractional flight-path uncertainty, which is ratio of the scintillator thickness to the flight path. Since each scintillator bar was 0.1 m thick along the neutron direction, and was placed at about 6 m, 0.1 /6 (or 1 part in 60) was the flight-path uncertainty. This leads to an irreducible TOF resolution of 1.27 ns (i. e. $76/60 = 1.27$) for a typical TOF value of 76 ns for the low-energy liquid-deuterium data.

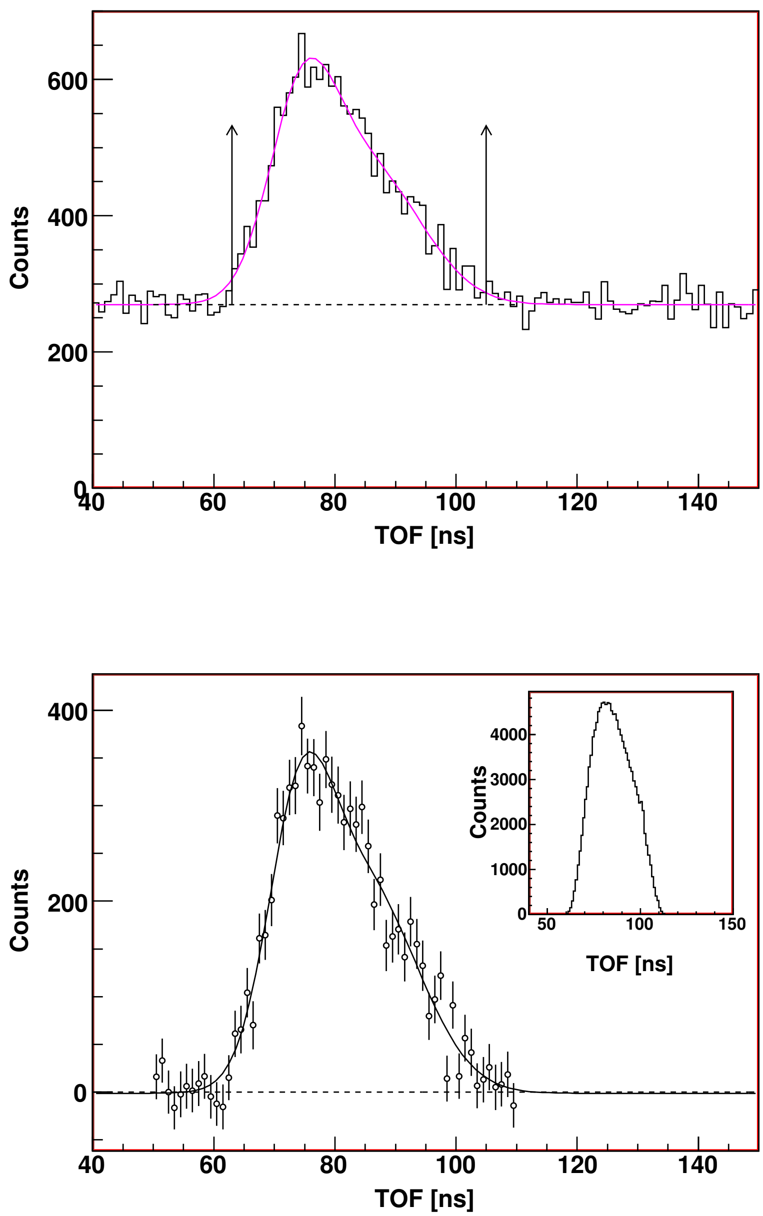

Fig. 6.8: The measured TOF spectrum for the low-energy liquid-deuterium data. The upper plot shows the signal plus the background. The signal falls between the two vertical arrows and the dashed line represents the background level. The magenta line is a fit to the data. The lower plot shows the signal after background subtraction. The smooth line is a fit to the data. The TOF is typically 76 ns (the mean value from a Gaussian fit). The inset shows the TOF calculated using missing-momentum information and gives confidence that the measured TOF signal is at the right place.

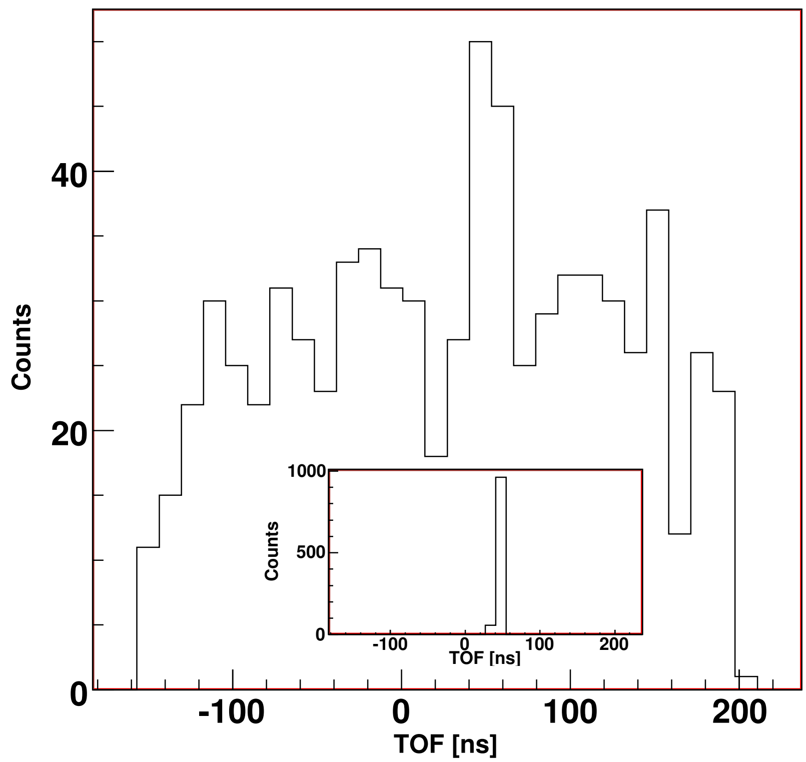

Fig. 6.9: The measured TOF spectrum for the high-energy liquid-deuterium data, at high missing momentum. The TOF is typically 45 ns. The inset shows the TOF calculated using missing-momentum information and gives confidence that the measured TOF signal is at the right place.

6.4 Momentum Reconstruction

It is useful to construct the momentum of detected neutrons using TOF information. Replacing p_m in Eqn.6.3 by simply p_n, the reconstructed momentum of the neutron, we get the following relation:

$$p_n = \frac{m}{\sqrt{(0.3\frac{t}{d})^2 - 1}} \tag{6.4}$$

Figure 6.10 shows this reconstructed momentum from the low-energy (2.345 GeV) liquid-deuterium calibration data. The reconstructed neutron momentum ranged from 200 to 320 MeV/c for this data set. The events are for the TOF peak (above the background level) in Fig. 6.8.

6.4.1 Momentum Resolution

The time-of-flight resolution can be used to find the momentum resolution as follows. The standard expression for β is

$$\beta = \frac{d}{ct} = \frac{p}{(m^2 + p^2)^{1/2}} \tag{6.5}$$

where a particle of mass m in GeV/c^2 with momentum p in GeV/c travels a distance d in a time t (also called time-of-flight). From this one can express the time-of-flight in terms of momentum

$$t = \frac{d(m^2 + p^2)^{1/2}}{cp} \tag{6.6}$$

or momentum in terms of time-of-flight

$$p = \sqrt{\frac{md^2}{c^2t^2 - d^2}}. \tag{6.7}$$

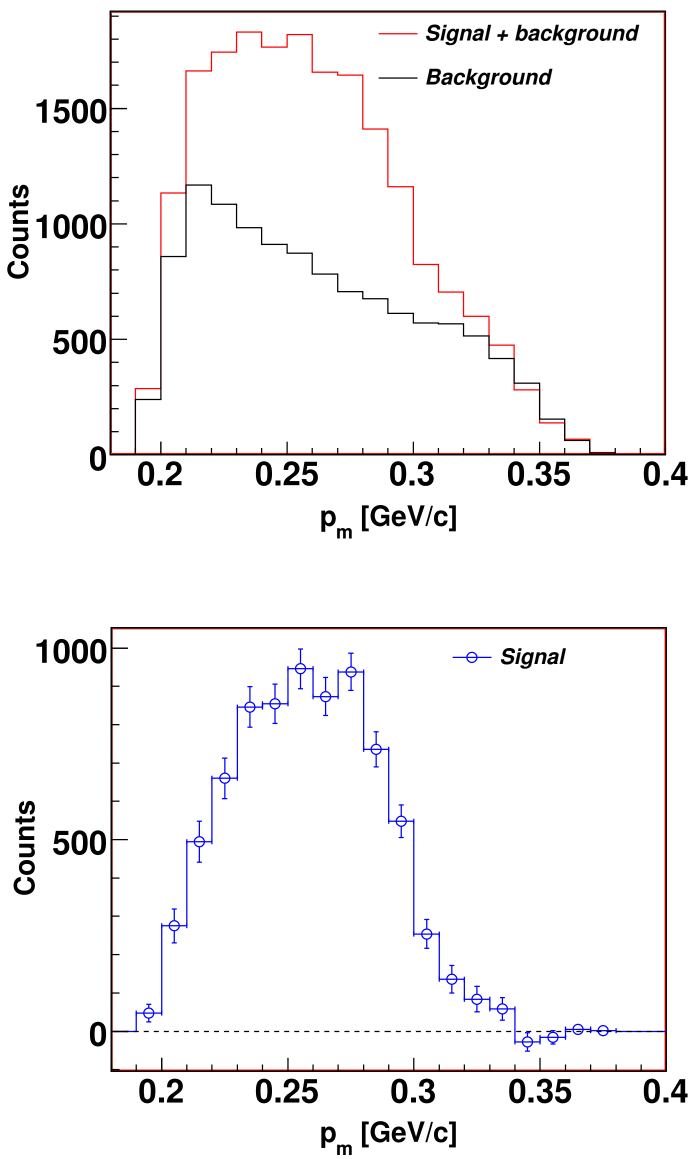

Fig. 6.10: The spectrum of neutron momenta reconstructed from time-of-flight information, using the low-energy (2.345 GeV) liquid-deuterium calibration data.

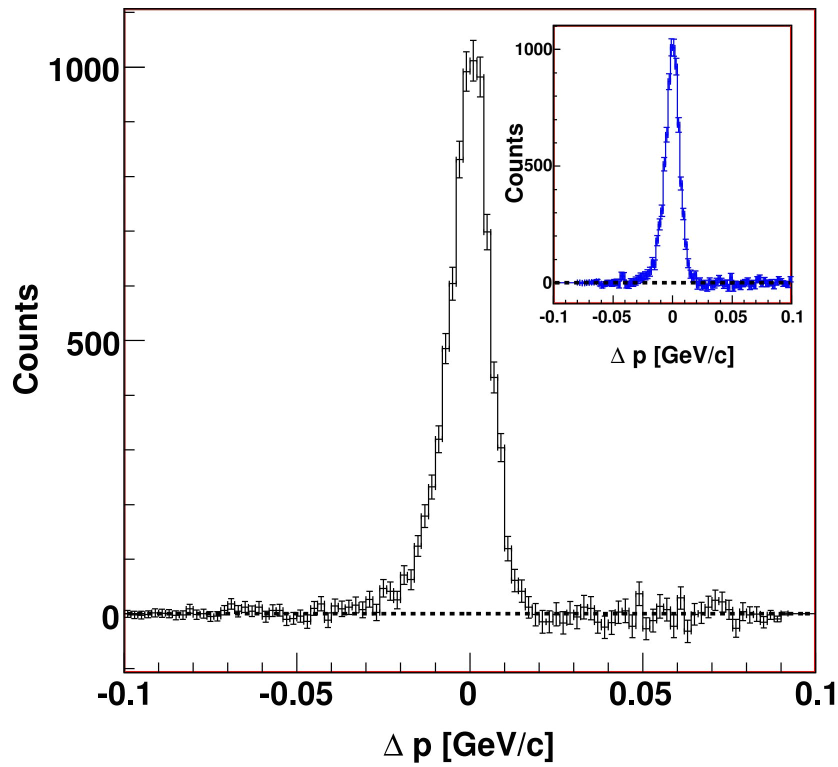

Fig. 6.11: The momentum resolution (Δp) obtained by plotting the difference in measured momentum and expected momentum for the low-energy liquid-deuterium data. The σ for this plot is 6 MeV/c. The inset is the momentum resolution (Δp) obtained by plotting Eqn.(6.12). The σ for this plot is also 6 MeV/c.

Now from relativistic dynamics, the momentum can be expressed as

$$p = \frac{mv}{\sqrt{(1 - \beta^2)}} = \frac{cm\beta}{\sqrt{(1 - \beta^2)}} \tag{6.8}$$

after differentiation we get

$$\frac{\partial p}{\partial \beta} = \frac{cm}{(1 - \beta^2)^{1/2}} + \frac{cm\beta^2}{(1 - \beta)^{3/2}} = \frac{cm}{(1 - \beta^2)^{3/2}}. \tag{6.9}$$

Hence from equations (6.8) and (6.9) we can obtain

$$\frac{\Delta p}{p} \;=\; \frac{\Delta\beta}{\beta(1 \;-\; \beta^2)}. \tag{6.10}$$

From equation (6.5) for a fixed distance d

$$\frac{\Delta\beta}{\beta} = \frac{\Delta t}{t} = \frac{c\beta\Delta t}{d}. \tag{6.11}$$

From (6.5), (6.10) and (6.11) we get

$$\Delta p = \frac{cp^2(m^2 + p^2)^{1/2}\Delta t}{m^2 d}, \tag{6.12}$$

which gives us the momentum resolution Δp once the time-of-flight resolution Δt is known. For $^2\mathrm{H}(e, e'p)n$ data, the $(e, e'p)$ reaction is "kinematically complete" by itself, hence the momentum of the detected neutron is known, a priori, independent of the actual measurement of the neutron. Thus comparison of the a priori neutron momentum determined from the $(e, e'p)$ reconstruction, and the measured neutron meomentum gives us another measure of the neutron momentum resolution. Shown in Fig. 6.11 is the momentum resolution determined in this fashion, while the inset in this figure is obtained using Eqn.(6.12). These plots were from the low-energy liquid-deuterium data. Both results agreed well, and σ was about 6 MeV/c in both cases[2]. This σ gives $\frac{\Delta p}{p} \sim 6$ % for the FWHM for 240 MeV/c, a typical momentum from this data set.

6.5 Event Rate

The data for the highest missing-momentum (523 MeV/c) kinematics (CK3) were taken at a beam current of 40 μA. Fig. 6.12 shows the event rate observed in

[2]The energy resolution (σ) for the same data set was about 2 MeV.

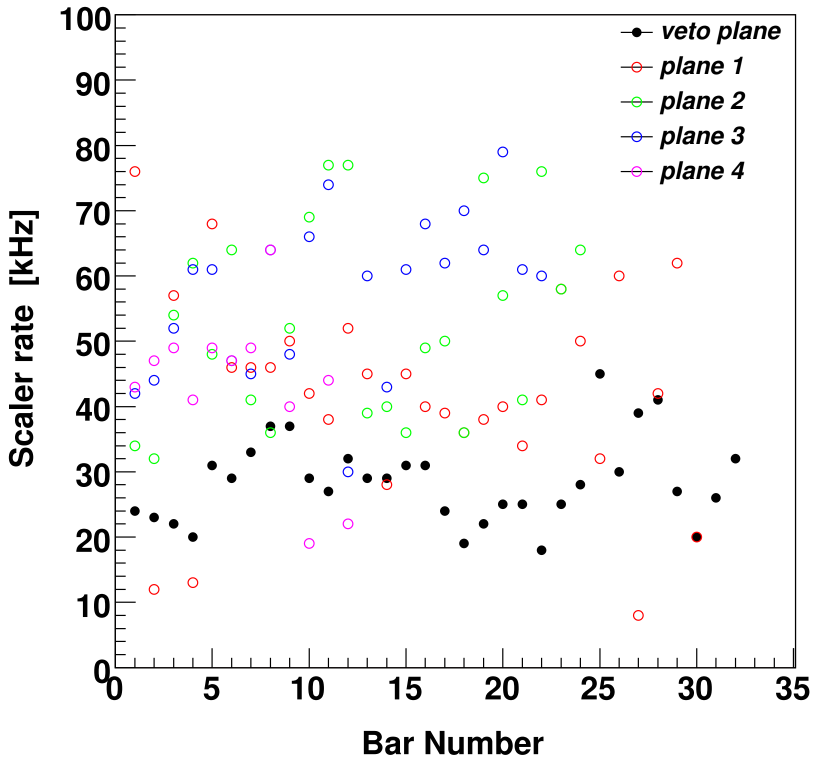

Fig. 6.12: Event rates in the neutron detector at a beam current of 40 μA.

the neutron detector. The rate was on average about 50 kHz in any scintillator bar and about 30 kHz in any veto counter at this beam current.

The event rate goes up as a function of beam current. We ran quite safely at currents as high as 60 μA as a test for the production data but the beam trip rate was unexpectedly high. A "beam trip" occurs when the accelerator stops working briefly when one of its componets experiences electrical overload. The higher the beam current, the more frequent are beam trips. Though the experiment was designed to run at 100 μA, the beam current of 40 μA kept the beam trip rate less than 20 times per hour.

6.6 Simulation

6.6.1 GEANT4

The GEANT4 (GEometry ANd Tracking) computer program developed at CERN [79] is a C^{++}-based Monte-Carlo simulation code for many applications, including (but not limited to) nuclear physics, high energy physics, accelerator physics, and medical physics. We developed a GEANT4 simulation for the neutron detector and the BigBite detector. Though we did not use it quantitatively in the present analysis, it was instrumental for understanding the kinematic setup of the experiment and the shielding of the neutron detector. Figure 6.13 shows typical particle tracks through the detector system for particles with 500 MeV/c momentum. The neutrons or the γ-rays are green tracks, the protons are blue tracks, and the electrons are red tracks. Though we did not distinguish between the neutrons and the γ-rays in the figure, in our actual analysis we had techniques for distinguishing between them, and we did not see any significant γ-rays passing through the lead wall. As can be seen from the figure, the lead wall was semi-transperant to neutrons (green tracks), while it blocked all the protons (blue tracks). Also evident from the bottom figure, is that the BigBite magnet bent the charged particles while not affecting the neutrals.

6.6.2 MCEEP

The neutron detector had finite acceptance. If all of the correlated n-p pairs in ^{12}C were at rest in the laboratory frame of reference, then the momenta of the proton and neutron would be back-to-back in the laboratory. The kinematics for the reaction would then be the same as the $^{2}\mathrm{H}(e,e'p)n$ reaction, where every $(e,e'p)$ event has a neutron entering the neutron detector acceptance. But for ^{12}C, a corre-

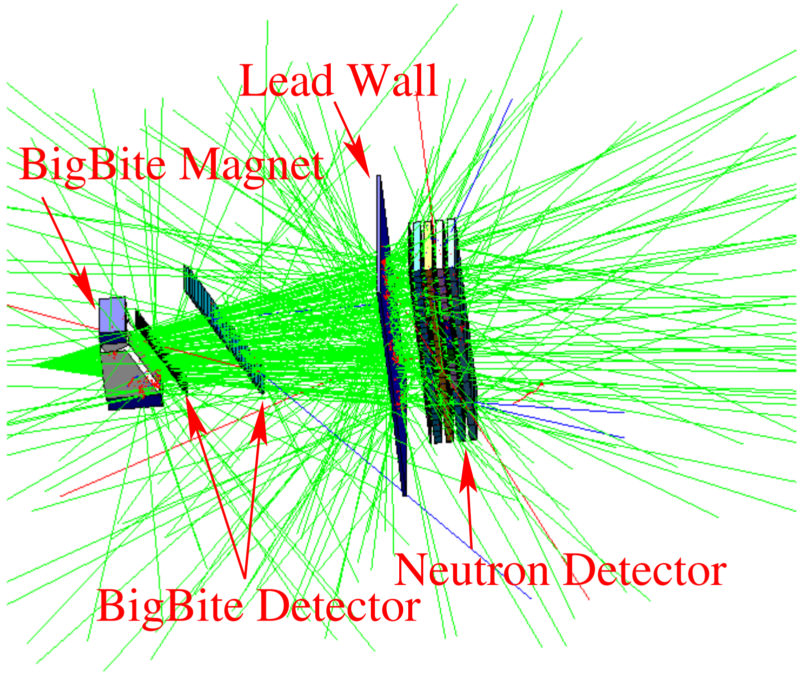

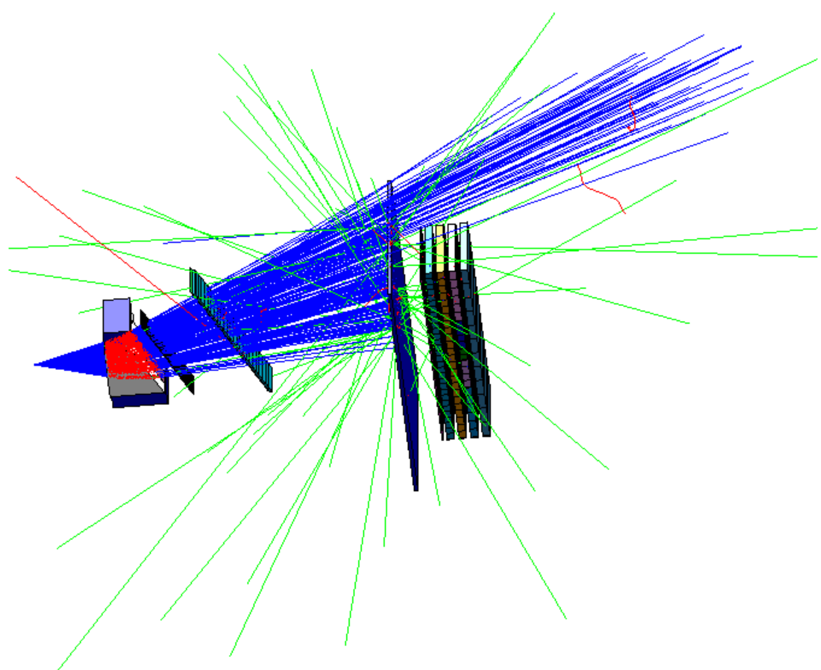

Fig. 6.13: Neutrons (top) and protons (bottom) emerging from the target in the GEANT4 simulation for the E01-015 experiment. Particle momenta were 500 MeV/c. Neutrons (and γ-rays), protons, and electrons are represented by green, blue, and red tracks, respectively.

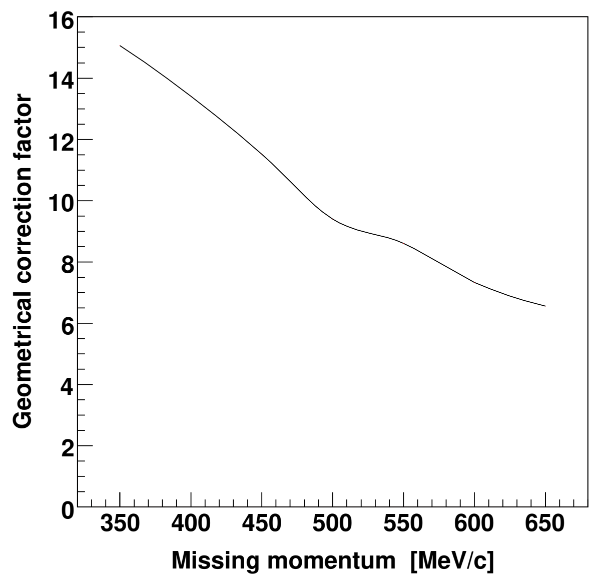

Fig. 6.14: Plot showing the extrapolation factor as a function of momentum for the phase space correction. This plot assumes a center-of-mass momentum of 136 MeV/c.

lated pair can be in motion in the laboratory frame, hence the proton and neutron momenta may not be back-to-back in the laboratory, and the neutron may miss the acceptance of the neutron detector, even though the scattered electron and knocked out proton are detected in the HRSs. We therefore had to find a correction factor for the fraction of neutrons missing the detector acceptance.

We estimated the fraction of neutrons that were outside the neutron detctor acceptance using the MCEEP package. MCEEP [80] is a Fortran-based Monte-Carlo simulation package developed in a collaborative effort for the Jefferson Laboratory Hall A spectrometers for A$(e, e'p)$ experiments. There were two kinds of MCEEP packages available based on different approaches; both gave identical results. One simulated a moving deuteron in a carbon nucleus[81] and the other simulated a moving deuteron[82]. In both cases we assigned a desired center-of-mass momentum to a n-p pair, and observed its center-of-mass motion for various neutron momenta.

The geometrical correction factor is the ratio of triple-coincidence neutrons without and with the neutron detector acceptance.

Figure 6.14 shows the extrapolation (geometrical correction) factor as a function of missing momentum that we had to use to convert the raw cross section ratio of $^{12}\mathrm{C}(e,e'pn)/^{12}\mathrm{C}(e,e'p)$ events to the corrected cross section ratio. For example at 510 MeV/c we had to multiply the raw cross section ratio of $^{12}\mathrm{C}(e,e'pn)/^{12}\mathrm{C}(e,e'p)$ events by a factor of 9.0 in order to get the corrected cross section ratio[3]. The plot is for a center-of-mass-momentum of 136 MeV/c for the n-p pair [83].

[3]The uncertainty in the geometrical correction factor is about 2%.

Chapter 7

Results and Discussion

7.1 ^{12}C$(e, e'pn)$ Result

The main findings from the production data at the highest missing-momentum (523 MeV/c) kinematics (CK3) will be presented here. The double-coincidence ^{12}C$(e, e'p)$ events were very pristine with almost zero background, as can be observed from the Fig. 7.1. The top plot in this figure shows the HRS coincidence time versus the recoil-neutron time-of-flight (TOF), and the bottom plot shows the HRS coincidence time versus the recoil-proton TOF. Along the TOF axis on both plots appears a ridge of background while there is no such ridge along the coincidence time of the HRSs. The NIKHEF result taken from the reference [36] for such quantities is shown in Fig. 7.2 where the double-coincidence (^{12}C$(e, e'p)$) time appears to have a large background (long ridge).

Shown in Fig. 7.3 is the TOF spectrum for recoil neutrons. The TOF peak is around 45 ns which is as expected for a neutron of about 500 MeV/c at a flight path of six meters. This TOF peak indicates the direct observation of short-range correlations since it corresponds, by choice of detector placement and setting, to the observation of coincident neutron-proton pairs of roughly equal and opposite momenta. The signal-to-background ratio for this TOF peak is about 1:6. We measured various kinematic varibles using the signal from this TOF spectrum. These variables will be discussed in the following.

Confirming the back-to-back nature of the momenta of nucleons of the correlated pair was another intriguing aspect of this investigation. We used Eqn. (2.12)

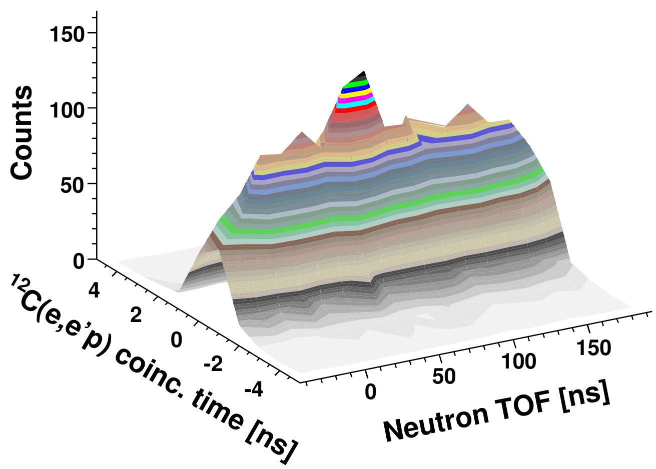

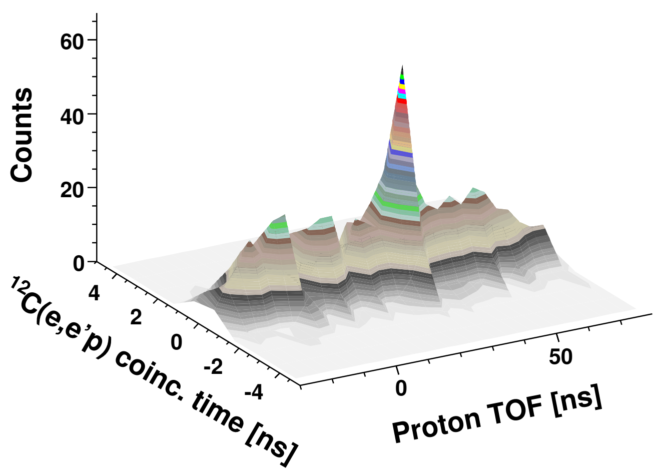

Fig. 7.1: Two dimensional spectra for the ^{12}C(e,e$'p$) coincidence time versus time-of-flight plots for recoiling neutrons (top) and recoiling protons (bottom) from the ^{12}C(e,e$'pN$) reaction. Both of these plots are for triple-coincident events.

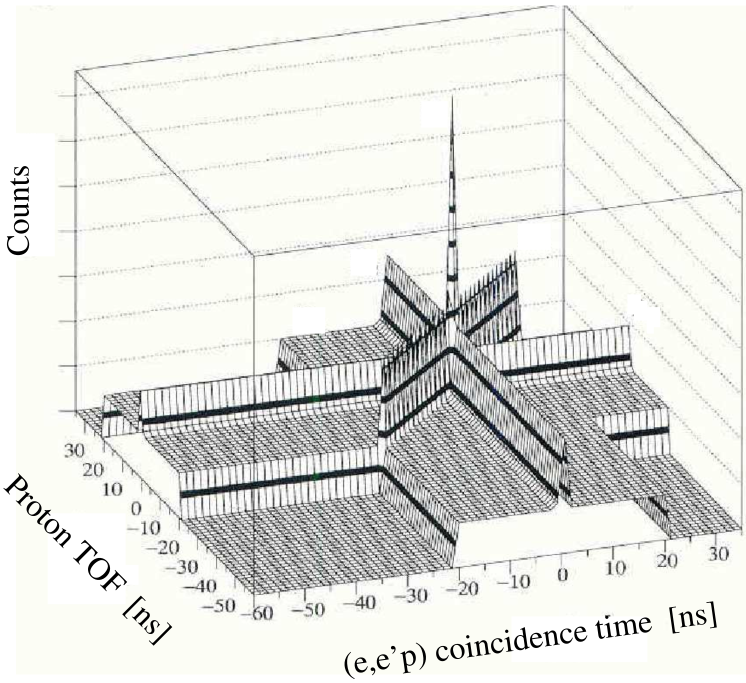

Fig. 7.2: NIKHEF result for a triple-coincidence TOF. Shown is the recoil-proton TOF for the ^{12}C(e,e$'pp$) reaction versus the ^{12}C(e,e$'p$) coincidence time. This figure is taken from [36].

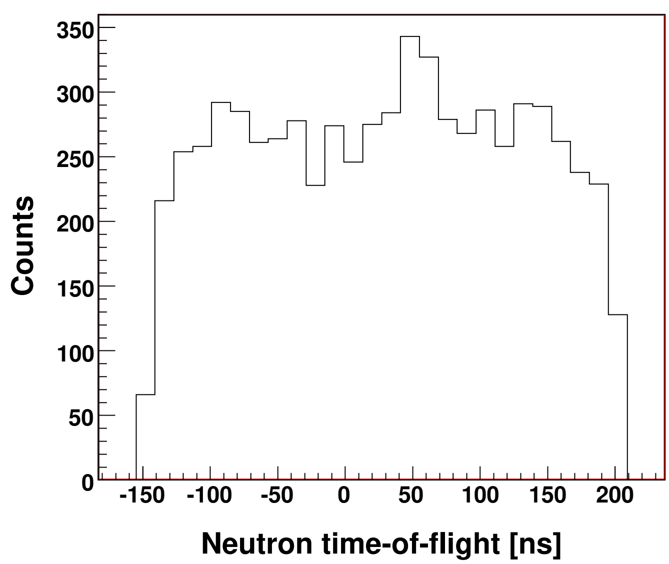

Fig. 7.3: Time-of-flight neutron spectrum from the production runs for the ^{12}C$(e, e'pn)$ reaction in the CK3 kinematics.

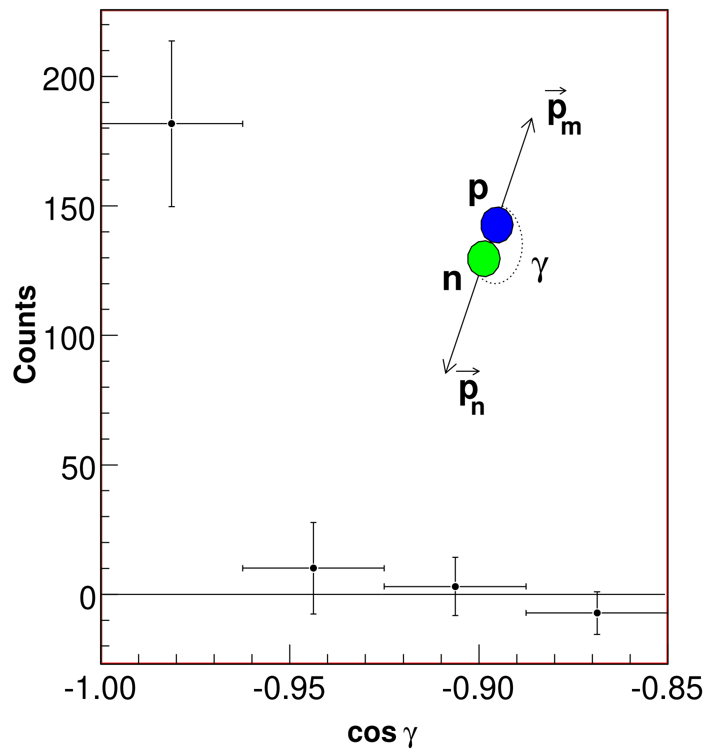

Fig. 7.4: Spectrum of the cosine of the angle between the missing momentum and the recoil-neutron momentum. The one-bin-signal between -0.96 to -1.0 shows that the proton and neutron in the pair in their initial states were back-to-back. The inset shows a cartoon of the back-to-back momenta of the members of the pair. Data are for the CK3 kinematics, after background subtraction (see Fig. 7.3)

to extract the angle between the momentum of the recoil neutron and the momentum of struck proton (before it was struck by the virtual photon) of the correlated n-p pair. Fig. 7.4 clearly demonstrates that the correlated neutron-proton pairs were observed to be nicely back-to-back. In this figure, almost all strength of the signal lies in the bin where the cosine of the angle between these two vectors is about -1 meaning an angle of 180° between these vectors.

The reconstructed momentum spectrum of the neutrons is shown in Fig 7.5. The upper panel shows neutron momenta reconstructed from the neutron TOF.

The lower panel shows neutron momenta computed from the $(e, e'p)$ missing momentum, i.e. assuming that the n-p pair was stationary in the laboratory frame of reference. We attribute the difference between these two spectra to the c.m. motion of the pair which is clearly not zero (as assumed in the bottom panel). The final result for the cross-section ratios discussed below was independent of the momentum reconstruction.

The missing energy for the $^{12}\text{C}(e, e'pn)$ reaction, calculated using Eqn.(2.10) (also called E_{2m} or double missing energy), is shown in Fig. 7.6. One has to have recoil-neutron momentum information in order to produce such a plot. The upper plot was produced using the neutron momentum derived from the measured TOF. For the lower plot, the neutron momentum was assumed to be equal to the missing momentum of the $^{12}\text{C}(e, e'p)$ reaction. Though we do not see any structure on these plots, the distribution is within an expected region [36] of about 30 to 80 MeV for the emission of a nucleon-nucleon pair.

Another point of interest was to look at the center-of-mass momentum and the relative momentum of the correlated n-p pair. The center-of-mass momentum is also interpreted, by momentum conservation, as the momentum of the $A-2$ residual nucleus. The relative momentum of the n-p pair given by

$$\vec{p}_{rel} = 0.5(\vec{p}_n - \vec{p}_p) \tag{7.1}$$

can also be interpreted as the momentum of the recoiling neutron. Figure 7.7 shows such momenta. The mean center-of-mass momentum is about 80 MeV/c and is a very small quantity when compared to the relative momentum of the n-p pair ($\sim$ 500 MeV/c).

For quantitative results, we measured cross-section ratios for various reaction

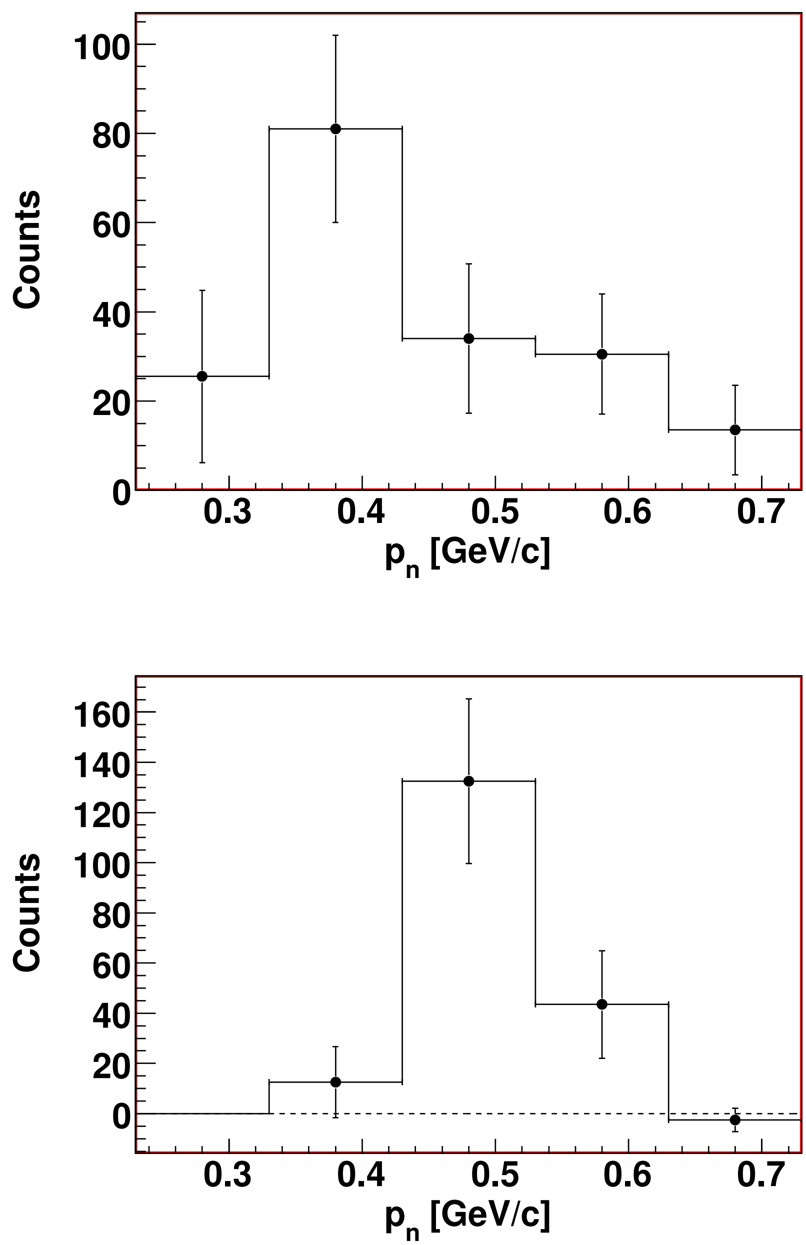

Fig. 7.5: Recoil-neutron momentum reconstruction spectra. The upper plot was reconstructed from the neutron time-of-flight. The lower plot came from the assumption that the neutron momentum was equal to the missing momentum.

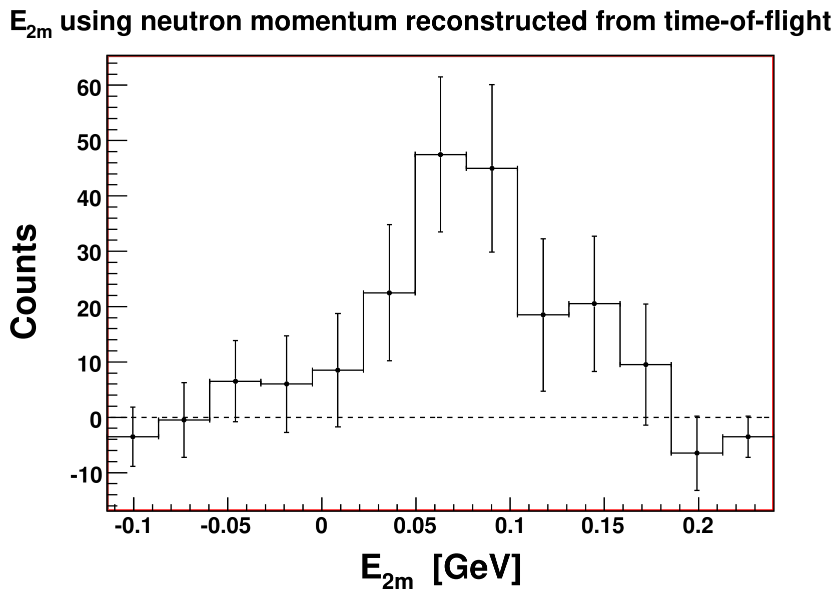

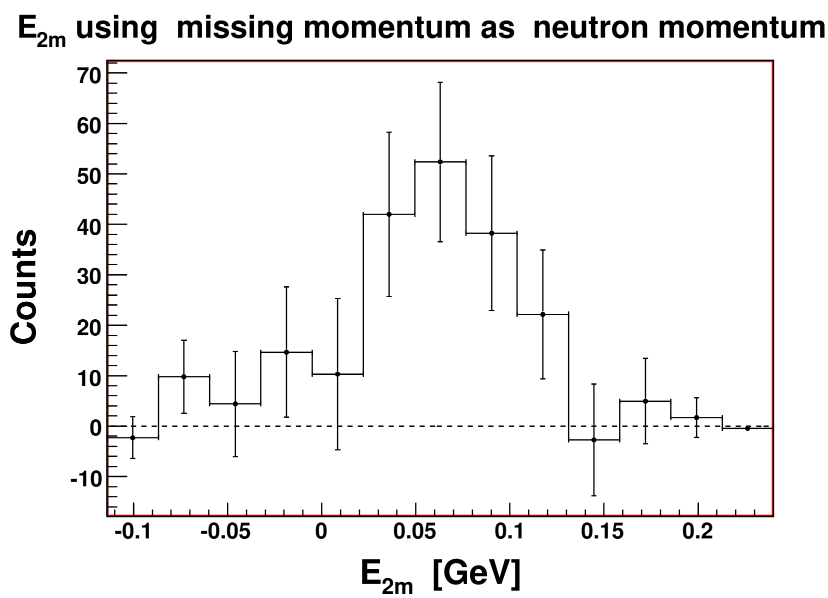

Fig. 7.6: Missing energy (E_{2m}) plot for the ^{12}C$(e, e'pn)$ reaction in the CK3 kinematics. For the upper plot the neutron momentum was reconstructed from its time-of-flight, while for the lower plot, we assumed that the recoil-neutron momentum was equal in magnitude to the missing momentum.

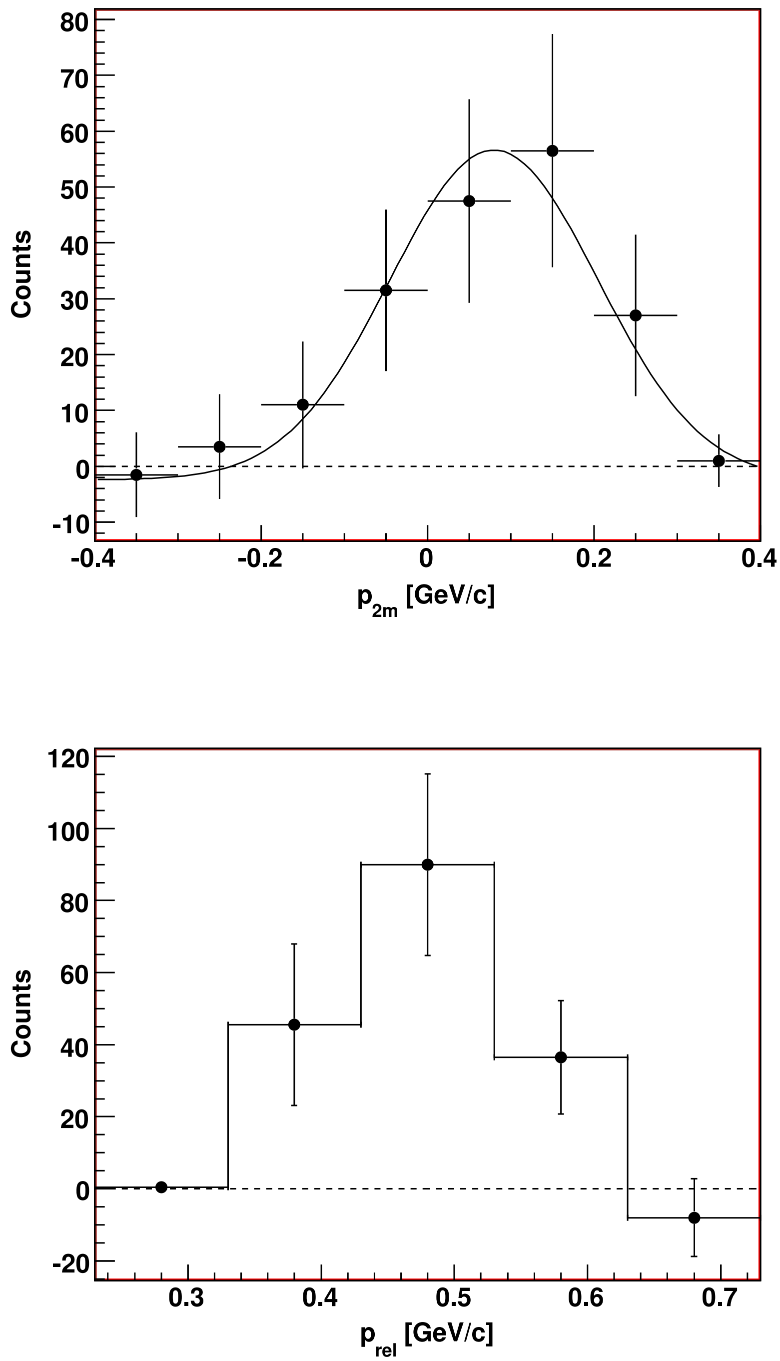

Fig. 7.7: The magnitude of center-of-mass momentum and the magnitude of relative momentum of the $^{12}C(e, e'pn)$ reaction. The center-of-mass momentum in the upper panel is about 80 MeV/c (the mean value of a Gaussian fit); the smooth curve is the Gaussian fit to the center-of-mass momentum. The relative momentum of the n-p pair is shown in the lower panel.

channels such as ^{12}C$(e, e'pn)$ to ^{12}C$(e, e'p)$, ^{12}C$(e, e'pp)$ to ^{12}C$(e, e'p)$, and finally ^{12}C$(e, e'pn)$ to ^{12}C$(e, e'pp)$. Extracting such ratios is advantageous because many of the sources of uncertainty may be identical to both reactions and therefore cancel in the ratio. This can be a nice tool when the amount of data is statistically small.

In Fig. 7.8 on the left we show the measured cross-section ratios for the ^{12}C$(e, e'pn)$ to ^{12}C$(e, e'p)$ and ^{12}C$(e, e'pp)$ to ^{12}C$(e, e'p)$ channels. On the right are extrapolated cross-section ratios (obtained by multiplying the measured cross-section ratio by the extrapolation factor of 9.0 as discussed in Sect. 6.6.2) for the acceptance correction for the same channels. In addition, the right pannel contains, for comparision, the result for the extrapolated cross-section ratio for ^{12}C(p, ppn) to ^{12}C(p, pp) channel (magenta color) measured at Brookhaven National Laboratory by the Eva-collaboration, as published in reference [1]. The agreement of the extrapolated cross-section ratios obained from these two experiments using completely different techneques and different probes shows that the outcome is technique-independent as well as probe-independent.

Finally the super ratio $\frac{^{12}C(e,e'pn)}{^{12}C(e,e'p)}$ to $\frac{^{12}C(e,e'pp)}{^{12}C(e,e'p)}$, or simply $\frac{^{12}C(e,e'pn)}{^{12}C(e,e'pp)}$ is shown in Fig. 7.9. The possibility of pair formation is 2Z(A-Z) for n-p pairs and 2Z(Z-1) for p-p pairs[1]. The virtual photon can couple to either one of the protons in the p-p pair; whichever proton absorbs the virtual photon is knocked out and is detected in the HRHs, while the recoil partner proton is detected in the BigBite detector. Hence all events related to p-p pairs were observed in the experiment. This was not the situation in the case of n-p pairs. When the virtual photon coupled to a proton of the n-p pair, this proton was detected in the right HRS and the recoil neutron was detected in the neutron detector. On the other hand, when the virtual

[1] Assuming p and n can form p-n and n-p pairs; p and p can form p-p and p-p pairs. Order matters.

photon coupled to the neutron of the n-p pair, the struck neutron went undetected and hence the recoiling proton was also undetected since it did not form a triple-coincidence event, and such an event would not be recorded in the datastream. For this reason, only half of the possible 2Z(A-Z) n-p pairs were detected even though all the pairs were there. In essence we measured only Z(A-Z) n-p pairs out of 2Z(A-Z) pairs and all 2Z(Z-1) p-p pairs. For the ^{12}C nucleus a possible n-p to p-p ratio would have been $72/60 = 1.2$ and only half of this value would have been measured in the present experiment. Based on this reasoning, in order to get the true ratio from the measured value, we should multiply the measured ratio by 2. Of course, zero to infinity is a possible range for the n-p to p-p ratio since zero (infinity) is a possible value when the numerator (denominator) is zero. The intriguing aspect of this experiment was that the n-p to p-p ratio was found to be much larger than 1.2.

7.2 Summary

- We detected a modest number of recoiling neutrons in the $^{12}\mathrm{C}(e, e'pn)$ reaction that were correlated with struck-proton partners.

- The momenta of the recoiling neutrons and the coincident protons were observed to be essentially back-to-back in the laboratory frame of reference.

- We observed large relative momenta and small center-of-mass momenta for the n-p pairs.

- Though no structures were observed in the double missing energy spectrum due to limited statistics, we observed its continuous distribution in the expected region.

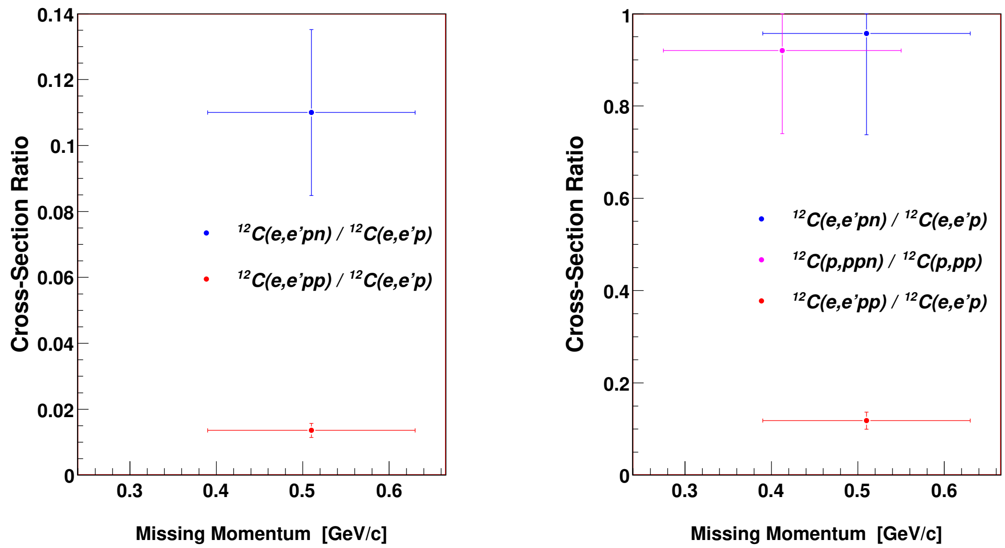

Fig. 7.8: The left plot is the measured cross-section ratio for $^{12}\mathrm{C}(e,e'pn)/^{12}\mathrm{C}(e,e'p)$ and $^{12}\mathrm{C}(e,e'pp)/^{12}\mathrm{C}(e,e'p)$. The right plot is extrapolated cross-section ratios using acceptance corrections, where the magenta is for $^{12}\mathrm{C}(p,ppn)/^{12}\mathrm{C}(p,pp)$ from reference [1] while the blue and red are for $^{12}\mathrm{C}(e,e'pn)/^{12}\mathrm{C}(e,e'p)$ and $^{12}\mathrm{C}(e,e'pp)/^{12}\mathrm{C}(e,e'p)$, respectively.

- We observed that there are many more n-p pairs than p-p pairs. The measured cross-section ratio $\frac{^{12}C(e,e'pn)}{^{12}C(e,e'p)}$ was 11.0 $\pm$ 2.5 % for n-p pairs and the measured cross-section ratio $\frac{^{12}C(e,e'pp)}{^{12}C(e,e'p)}$ was only 1.4 $\pm$ 0.2 % for p-p pairs.

- The measured value for the super ratio $\frac{^{12}C(e,e'pn)}{^{12}C(e,e'p)}$ to $\frac{^{12}C(e,e'pp)}{^{12}C(e,e'p)}$, or simply $\frac{^{12}C(e,e'pn)}{^{12}C(e,e'pp)}$ was 8.1 $\pm$ 2.2.

Taking into account the kinematical restriction of the measurement (the need for a multiplication factor of 2 as explained in Sect.7.1), this super ratio becomes 16.1 $\pm$ 4.5. In addition, due to single charge-exchange reactions, like np –> pp, more p-p pairs can be generated. The correction for the effect of single charge-exchange reactions was found to be 11% [69]. After this correction, the n-p to p-p ratio becomes 17.9 $\pm$4.5.

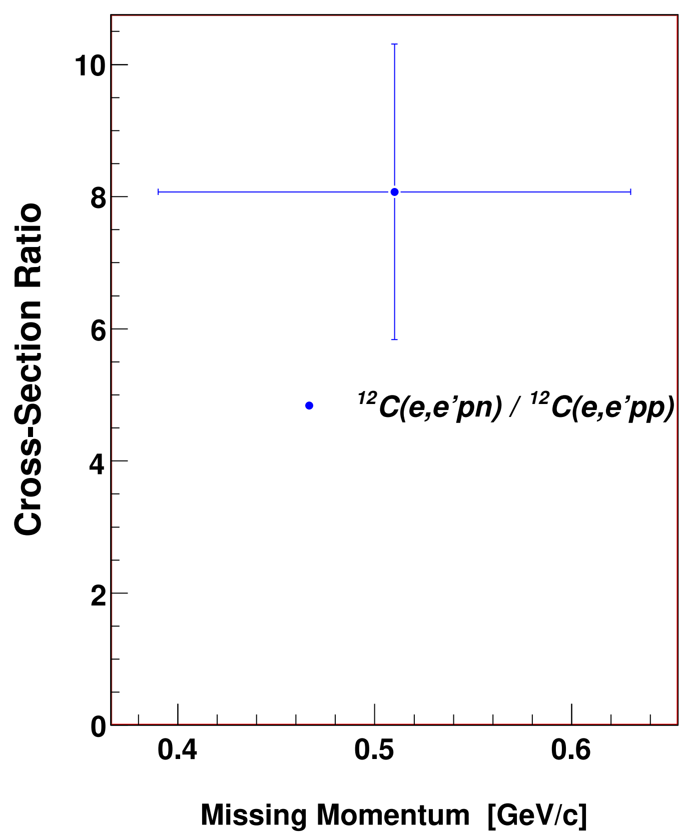

Fig. 7.9: The cross-section ratio for the $^{12}\mathrm{C}(e,e'pn)/^{12}\mathrm{C}(e,e'pp)$ reactions.

The finding that the n-p to p-p short-range correlated pair ratio as 17.9 $\pm$ 4.5 compared to a naively expected value of 1.2 was the outstanding discovery of this SRC experiment. This large ratio could have far-reaching implications for modeling and understanding cold dense nuclear matter such as neutron stars [5].

A theoretical calculation, according to the reference [84], which includes central, tensor, and spin-isospin correlations, assumes that tensor correlations play a key role in producing more n-p pairs than p-p pairs.

Based upon this investigation and other results of E01-015 experiment, there is a newly approved experiment, E07-006 [67], that will investigate short-range correlations using the ^{4}He$(e, e'pN)$ reaction in the missing momentum range from 400 to 875 MeV/c, using a setup similar to E01-015.

7.3 Conclusion

Correlations in nuclei are generally classified into two types: long-range correlations due to the long-range, attractive part of the nucleon-nucleon interaction, and short-range correlations due to the short-range, repulsive part of the nucleon-nucleon interaction. We investigated electron-induced two-nucleon emission from carbon with the goal of being sensitive to and studying short-range correlations using the ^{12}C$(e, e'pN)$ reaction in a triple-coincidence measurement. The kinematic coverage was such that $Q^2 = 2$ (GeV/c)^2, $x_B = 1.2$, and the missing momentum of the ^{12}C(e,e$'$p) reaction ranged from 250 to 650 MeV/c. Two existing high-resolution spectrometers were used to detect the scattered electrons and and the struck protons in the ^{12}C(e,e$'$pn) reaction . On the other hand, the recoiling neutrons in the same reaction were detected using the time-of-flight method by the large neutron detector designed and constructed specially for this experiment. Since short-range correlations can be emulated by various two-body effects such as meson-exchange currents, isobar currents and final-state interactions, we chose anti-parallel kinematics with high Q^2 at $x_B > 1$ to minimize them.

We performed the analysis of the $^{12}C(e, e'pn)$ reaction, and made direct observation of short-range correlated n-p pairs. From our analysis we conclude that there are 17.9±4.5 times more n-p short-range correlated pairs than p-p short-range correlated pairs.

Bibliography

[1] E. Piasetzky et al., Phys. Rev. Lett. **97**, 162504 (2006).

[2] R. V. Reid, Ann. of Phys **50**, 411 (1968).

[3] G. E. Brown and M. Rho, Phys. Today **Feb**, 24 (1983).

[4] E. J. Moniz et al., Phys. Rev. Lett. **26**, 445 (1971).

[5] M. M. Sargsian et al., J. Phys. **G29**, R1 (2003).

[6] F. Benmokhtar, Ph. D. Thesis, Rutgers, The State university of New Jersey (2004).

[7] F. Benmokhtar et al., Phys. Rev. Lett. **94**, 082305 (2004).

[8] D. Rohe et al., Phys. Rev. Lett. **93**, 182501 (2004).

[9] L. J. H. M. Kester et al., Phys. Rev. lett. **74**, 1712 (1995).

[10] A. Zondervan et al., Nucl. Phys. **A 587**, 697 (1995).

[11] C. J. G. Onderwater et al., Phys. Rev. Lett. **78**, 4893 (1997).

[12] C. J. G. Onderwater et al., Phys. Rev. Lett. **81**, 2213 (1998).

[13] G. Rosner, Prog. Part. Nucl. Phys **44**, 99 (2000).

[14] D. G. Middleton et al., arXive:nucl-ex **0701053**, v1 (2007).

[15] B. Zhang, Ph. D. Thesis, Massachusetts Institute of Technology (2003).

[16] R. Niyazov, Ph. D. Thesis, Old Dominion University (2003).

[17] R. A. Niyzov et al., Phys. Rev. Lett. **92**, 052303 (2004).

[18] A. Tang, Ph. D. Thesis, Kent State University (2002).

[19] J. L. S. Aclander, Ph. D. Thesis, Tel-Aviv University, Israel (2001).

[20] A. Tang et al., Phys. Rev. Lett. **90**, 042301 (2003).

[21] O. Benhar and V. R. Pandharipande, Nucl. Phys. **A 473**, 234 (1987).

[22] O. Benhar et al., Nucl. Phys. **A 505**, 267 (1989).

[23] S. C. Pieper et al., Phys. Rev. **C 46**, 1741 (1992).

[24] J. Ryckebusch et al., Nucl. Phys. **A 624**, 581 (1997).

[25] B. Povh, K. Rith, C. Scholz, and F. Zetsche, PARTICLE AND NUCLEI, An Introduction to the Physical Concepts, 3rd Ed., Springer-Verlag, (1999).

[26] A. Accardi et al., arXiv:nucl-th/0701024v2 (2007).

[27] L. Lapikas, Nucl. Phys. **A553**, 297c (1993).

[28] C. Ciofi degli Atti, and S. Simula, Phys. Rev. **C 53**, 1689 (1996).

[29] P. Grabmayr, Prog. Part. Nucl. Phys. **29**, 251 (1992).

[30] W. H. Dickhoff and C. Barbieri, Prog. Part. Nucl. Phys. **52**, 377 (2004).

[31] O. Benhar et al., Phys. Lett. **B 177**, 135 (1986).

[32] K. Gottfried, Nucl. Phys. **5**, 557 (1957).

[33] L. I. Frankfurt and M. I. Strikman, Phys. Rep. **76**, 215 (1981).

[34] L. Frankfurt and M. Strikman, Phys. Rep. **160**, 235 (1988).

[35] S. C. Pieper, R. B. Wiringa, and V. R. Pandharipande, Phys. Rev. **C 46**, 1741 (1992).

[36] L. J. H. M. Kester, Ph. D. Thesis, Free University Amsterdam (1993).

[37] J. Ryckebusch et al., Nucl. Instr. and Meth. **624**, 581 (1997).

[38] S. Janssen et al., Nucl. Phys. **A 672**, 285 (2000).

[39] C. C. degli Atti and D. Treleani, Phys. Rev. **C 60**, 024602 (1999).

[40] O. Benhar and V. R. Pandharipande, Phys. Rev. **C 47**, 2218 (1993).

[41] O. Benhar, V. R. Pandharipande and S. C. Pieper, Rev. Mod. Phys. **65**, 817 (1993).

[42] R. Schiavilla, A. Fabrocini, and V. R. Pandharipande, Nucl. Phys. **A 473**, 290 (1987).

[43] J. Carlson, R. Schiavilla, Rev. Mod. Phys. **70**, 743 (1998).

[44] D. B. Day et al., Phys. Rev. Lett. **59**, 427 (1987).

[45] J. Arrington et al., Phys. Rev. Lett. **82**, 2056 (1999).

[46] C. Ciofi degli Atti, and G. B. West, Phys. Lett. **B 458**, 447 (1999).

[47] O. Benhar, Phys. Rev. Lett. **83**, 3130 (1999).

[48] K. S. Egiyan et al., Phys. Rev. Lett. **96**, 082501 (2006).

[49] P. Monaghan, Ph. D. Thesis, Massachusetts Institute of Technology (2007).

[50] P. K. A. de Witt Huberts, Nucl. Part. Phys. **16**, 507 (1990).

[51] T. de Forest Jr., Nucl. Phys. **A 392**, 232 (1983).

[52] W.Bertozzi, E. Piasetzky, J. Watson, and S. Wood, Studying Short-Range Correlations in Nuclei at the Repulsive Core Limit via the Triple Coincidence (e,e'pN), Jefferson Lab Hall A Proposal **E01-015**, (2000).

[53] J.Alcorn, at al., Nucl. Instr. and Meth. **A 522**, 294 (2004).

[54] D.J.J. de Lange, at al., Nucl. Instr. and Meth. **A 406**, 182 (1998).

[55] D.J.J. de Lange, at al., Nucl. Instr. and Meth. **A 412**, 254 (1998).

[56] Jefferson Lab Hall A webpage, http://www.jlab.org/help/Ghelp/halla3d.html .

[57] K. G. Fissum, at al., Nucl. Instr. and Meth. **A 474**, 108 (2001).

[58] W. R. Leo, Techniques for Nuclear and Particle Physics Experiments, A How-to Approach, 2nd Ed., Springer-Verlag (1994).

[59] M. Iodice, at al., Nucl. Instr. and Meth. **A 411**, 223 (1998).

[60] G. Cates, K. McCormic, B. Reitz, and B. Wojtsekhowski, Measurement of the Neutron Electric Form Factor G_E^n at High Q^2, Jefferson Lab Hall A Proposal **E02-013**, (2001).

[61] J. Annand, D. Higinbotham, R. Lindgren, V. Nelyubin, and B. Norum, Precisioin Measurement of the Electroproduction of Π^0 Near Threshold: A Test of Chiral QCD Dynamics , Jefferson Lab Hall A Proposal **E04-007**, (2003).

[62] G. Cates, V. Nelyubin, and P. Reimer, High Resolution Study of the Resonance in nK^+ System, Jefferson Lab Hall A Proposal **E05-009**, (2004).

[63] S. Gilad, D. Higinbotham, W. Korsch, B. Norum, and S. Sirca, Measurements of A_x and A_z Asymmetries in the Quasi-elastic $^3He(e,e'd)$ Reaction , Jefferson Lab Hall A Proposal **E05-102**, (2005).

[64] J. P. Chen, X. Jiang, J. c. Peng, Measurement of Single Target-Spin Asymmetry in Semi-Inclusive $\vec{n}(e,e'\Pi^-)$ Reaction on a Transversely Polarized ^3He Target, Jefferson Lab Hall A Proposal **E06-010**, (2005).

[65] S. Choi, X. Jiang, Z. E. Meziani, and B. Swatzky, Precision Measurements of the Neutron d_2: Towards the Electric χ_E and Magnetic χ_B Color Polarizabilities, Jefferson Lab Hall A Proposal **E06-014**, (2005).

[66] W. Bertozzi, G. Cates, K. Grimm, N. Liyanage, Z. E. Meziani, G.Rosner, B. Wojtsekhowski, and Z. Zhang, Measurement of neutron asymmetry A_1n in the valence quark region using 8.8 GeV and 6.6 GeV beam energies and BigBite spectrometer in Hall A, Jefferson Lab Hall A Proposal **E12-06-122**, (2006).

[67] S. Gilad, D. W. Higinbotham, B. Moffit, E. Piasetzky, J. Watson, Studying the Internal Small-Distance Structure of Nuclei via the Triple Coincidence (e,e'pN), Jefferson Lab Hall A Proposal 07-006 (2007).

[68] R. Shneor, M. Sc. Thesis, Tel-Aviv University, Israel (2003).

[69] R. Shneor, Ph. D. Thesis, Tel-Aviv University, Israel (2007).

[70] $Hall\ A\ Survey\ report\ (report\ numbers\ A969\ and\ A987)\ for\ the\ experiment\ E01015$, $http://hallaweb.jlab.org/news/minutes/Survey\_Reports/Survey\_Reports.html$ (2005).

[71] P. Monaghan, Survey Report posted on $http://hallaweb.jlab.org/experiment/E01-015/$, Massachusetts Institute of Technology .

[72] R. A. Cecil, B. D. Anderson, and R. Madey, Nucl. Instr. and Meth. **161**, 439 (1979).

[73] V. McLane et al., Neutron Cross Section, Curves, Volume 2, Academic Press (1999).

[74] J. W. Watson, Private communication .

[75] Jefferson Lab Hall A analyzer, http://hallaweb.jlab.org/root/index.html .

[76] ROOT - An Object-Oriented Data Analysis Framework, http://root.cern.ch .

[77] N. Liyanage, Ph. D. Thesis, Massachusetts Institute of Technology (1999).

[78] R. Madey et al., Nucl. Instr. and Meth. **214**, 401 (1983).

[79] GEANT4 simulation, http://geant4.web.cern.ch/geant4/ .

[80] P. E. Ulmer, MCEEP: Monte Carlo for electro-nuclear coincidence experiments, http://hallaweb.jlab.org/publications/Technotes/technote.html (1991).

[81] S. Wood, Private communication .

[82] R. Shenor, Private communication .

[83] R.Shneor et al., arXiv:nucl-ex/0703023 (2007).

[84] R. Schiavilla et al., Phys. Rev. Lett. **98**, 132501 (2007).

[85] J. F. Janni, At. Data Nucl. Data Tables **27**, 147 (1982).

Appendix A

Neutron Detection Efficiency Determination

In this Appendix we describe how the effective threshold was determined, which is central for calculating the efficiency of the neutron detector.

A.1 The Threshold Determination

We used e-p elastic scattering (LH kinematics) to provide a proton flux of known energy passing through the neutron detector. In this kinematics, all protons entering the neutron detector were passing protons, which were not completely stopped. For these passing protons, the energy loss in the scintillator E_{loss} is in a regime where the light production in MeVee is equal to E_{loss} in MeV. In the hydrogen elastic runs, scattered electrons went to the HRSL and the recoiling protons went to the neutron detector. Neither the BigBite magnet nor the BigBite detector package were between the target and the neutron detector. The neutron detector was sitting 15 m from the target, 50° right of the beamline (while viewing the beam dump from the target). Hence the energy loss of proton occured only in the target chamber materials and the materials (such as air and plastic scintillator bars) between the target and the scintillator bar. In order to calculate the proton energy loss, we used proton energy loss tables from [85]. Figure A.1 is a typical ADC plot for one PMT of one bar from the elastic hydrogen run. The arrow indicates the peak channel, for

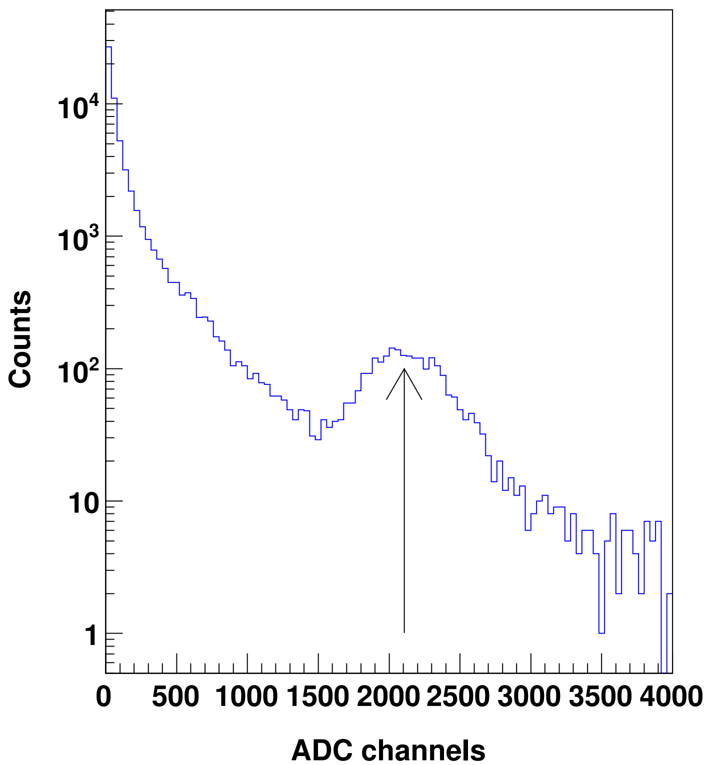

Fig. A.1: Typical ADC spectrum from the hydrogen elastic run from one phototube of one scintillator bar. The arrow indicates the peak channel selected.

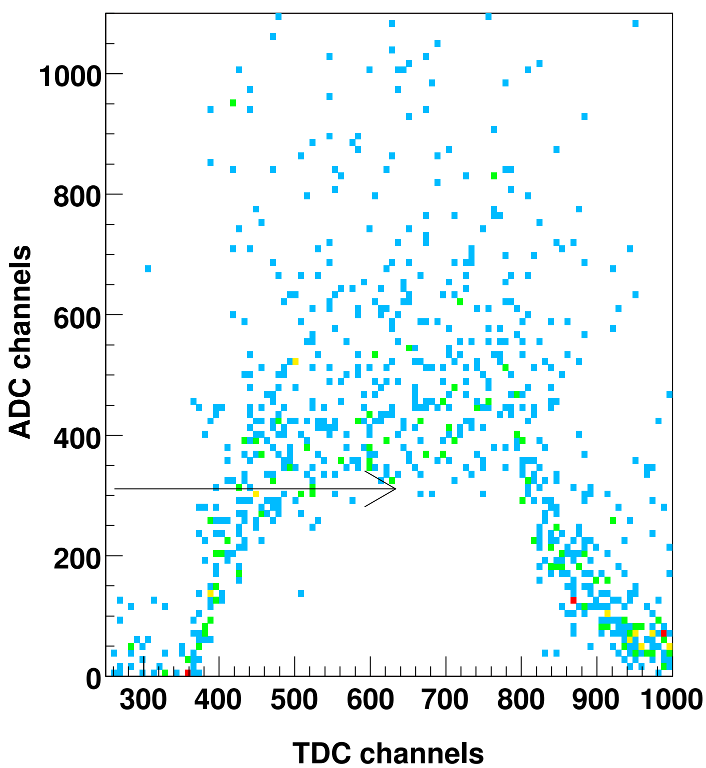

Fig. A.2: Typical ADC versus TDC spectrum from the ^{12}C production runs from one phototube of one scintillator bar in the neutron detector. The ADC channel indicated by the arrow is the threshold.

which we know E_{loss}. The hydrogen elastic data give us a point of known energy deposition and hence light output for each phototube. The next step is to determine the electronic threshold for each phototube. This was accomplished by using the ^{12}C production data and observing the minimum ADC output. Figure A.2 is a scatter plot of the ADC versus the TDC signals for production runs. Here one can clearly see the ADC threshold in the TDC window: the ADC channel corresponding to that threshold value (Fig. A.2) was then recorded. Note that all ADC values were "pedestal subtracted" so the ADC scale has a true zero.

The proton elestic peaks (Fig. A.1) and ADC thresholds (Fig. A.2) were then combined with the calculated E_{loss} for the protons to determine the ADC threshold in MeVee for each phototube:

$$Threshold = \frac{ADC_{Threshold}}{ADC\ peak} Eloss \tag{A.1}$$

The threshold value was determined for all individual scintillator bars and finally, an average value for each plane was calculated.

A.2 The Efficiency Data

In this section, we present the complete set of the efficiencies that were used for data analysis. Table A.1 shows the data plotted in Fig. 4.2. The simulation code needs the height, length and thickness of a scintillator bar in its input file. Though the length and the thickness of all scintillator bars were alike, the third plane had bars of mixed heights. We used an average height of 12.5 cm in the input file of the simulation code for a scintillator bar in the third plane.

The removal cross section (i.e., non elastic cross section) in barns for the relevant elements and materials are given in Table A.2. Here the non-elastic cross section for Pb, Fe and C were directly read from [73] and that for air was obtained from [74]. The removal cross section for plastic was calculated from information for C and H, assuming that the plastic is made up of C and H only with the H to C ratio equal to 1.104. Note that the removal cross section for H was taken as the two thirds of the total cross section.

The table A.3 shows the transmittance data for the relevant materials. Note that the following thicknesses for materials between the target and the front face of the plane one of the neutron detector were used: air 600 cm, lead in the lead wall 5.08 cm, iron in the lead wall 4 cm, scintillator plastic in the three planes of the BigBite detectors 3.55 cm, the two overlaping veto bars 4 cm. Also note that every scintillator bar in the neutron detector had a thickness of 10 cm.

The number density (n), length (L) and n∗L for the relevant subtances were:

Lead: $n = 0.03300{*}10^{24}\ cm^{-3}$, $L = 5.08\ cm$, $nL = 0.16774{*}10^{24}\ cm^{-2}$,

Iron: $n = 0.08460{*}10^{24}\ cm^{-3}$, $L = 4.00\ cm$, $nL = 0.33853{*}10^{24}\ cm^{-2}$,

Plastic: $n = 0.99784{*}10^{23}\ cm^{-3}$, $L = 7.55\ cm$, $nL = 0.75336{*}10^{24}\ cm^{-2}$,

Air: $n = 0.00270{*}10^{22}\ cm^{-3}$, $L = 600.0\ cm$, $nL = 0.01620{*}10^{24}\ cm^{-2}$.

Kinetic Energy (MeV)	**Efficiency (%) of a Neutron bar in the**			
	First Plane	Second Plane	Third Plane	Fourth Plane
20.0	4.948	7.636	8.154	0.078
30.0	7.039	8.225	8.5	5.355
40.0	8.093	9.509	9.804	5.972
50.0	9.567	10.924	11.44	7.899
60.0	10.324	11.459	11.64	8.62
70.0	10.147	11.024	11.283	8.958
80.0	10.049	10.667	10.827	8.982
90.0	9.754	10.337	10.505	9.072
100.0	9.555	10.007	10.175	8.893
110.0	9.649	10.172	10.223	9.095
120.0	9.342	9.654	9.759	8.663
130.0	9.134	9.547	9.709	8.674
140.0	9.104	9.439	9.567	8.57
150.0	9.0	9.448	9.552	8.732
160.0	8.87	9.355	9.451	8.47
175.0	9.033	9.451	9.51	8.754

Table A.1: Efficiency of different scintillator bars at different neutron kinetic energies for the “effective thresholds”.

Kinetic Energy (MeV)	**Removal Cross section (barns)**					
	Pb	Fe	C	H	Plastic	Air
20.0	2.6	1.25	0.50	0.33	0.41	0.201
30.0	2.5	1.00	0.42	0.20	0.305	0.249
40.0	2.4	0.95	0.36	0.15	0.25	0.232
50.0	2.3	0.9	0.32	0.11	0.21	0.197
60.0	2.2	0.8	0.26	0.09	0.171	0.160
70.0	2.0	0.78	0.22	0.07	0.142	0.137
80.0	1.9	0.76	0.21	0.06	0.13	0.114
90.0	1.85	0.74	0.22	0.05	0.131	0.091
100.0	1.8	0.73	0.23	0.047	0.135	0.077
110.0	1.75	0.71	0.23	0.043	0.133	0.066
120.0	1.7	0.70	0.24	0.04	0.135	0.056
130.0	1.65	0.68	0.23	0.039	0.13	0.050
140.0	1.6	0.66	0.22	0.037	0.124	0.048
150.0	1.55	0.65	0.21	0.033	0.117	0.048
160.0	1.52	0.65	0.20	0.031	0.116	0.048
175.0	1.5	0.60	0.19	0.030	0.116	0.048

Table A.2: Removal cross section for Pb, Fe, C, H, plastic, and air at various neutron kinetic energies.

Kinetic Energy (MeV)	**Transmittance**						
	Pb	Fe	Air	Plastic #1	Plastic #2	Plastic #3	Plastic #4
20.0	0.65	0.655	0.997	0.73	0.49	0.32	0.22
30.0	0.66	0.713	0.996	0.795	0.59	0.43	0.32
40.0	0.67	0.725	0.996	0.83	0.65	0.50	0.39
50.0	0.68	0.737	0.997	0.85	0.69	0.56	0.46
60.0	0.69	0.763	0.997	0.88	0.74	0.62	0.53
70.0	0.715	0.77	0.998	0.90	0.78	0.68	0.59
80.0	0.727	0.77	0.998	0.91	0.80	0.70	0.61
90.0	0.73	0.78	0.999	0.91	0.80	0.70	0.61
100.0	0.74	0.78	0.999	0.90	0.79	0.69	0.60
110.0	0.746	0.786	0.999	0.90	0.79	0.69	0.61
120.0	0.75	0.79	0.999	0.90	0.79	0.69	0.60
130.0	0.76	0.79	0.999	0.91	0.80	0.70	0.61
140.0	0.765	0.80	0.999	0.91	0.80	0.71	0.63
150.0	0.77	0.80	0.999	0.92	0.81	0.72	0.65
160.0	0.775	0.80	0.999	0.92	0.82	0.73	0.65
175.0	0.78	0.816	0.999	0.92	0.82	0.73	0.65

Table A.3: Transmittance for Pb, Fe, air, 7.55 cm thick plastic (Plastic#1), 17.55 cm thick plastic (Plastic#2), 27.55 cm thick plastic (Plastic#3), and 37.55 cm thick plastic (Plastic#4) at various neutron kinetic energies.

Kinetic Energy (MeV)	**Transmittance of different Combination of materials**			
	Combination #1	Combination #2	Combination #3	Combination #4
20.0	0.31	0.21	0.134	0.092
30.0	0.37	0.27	0.198	0.147
40.0	0.40	0.31	0.24	0.187
50.0	0.42	0.34	0.277	0.228
60.0	0.46	0.385	0.320	0.276
70.0	0.49	0.426	0.370	0.320
80.0	0.50	0.444	0.390	0.340
90.0	0.51	0.452	0.396	0.345
100.0	0.515	0.453	0.395	0.344
110.0	0.52	0.46	0.40	0.356
120.0	0.53	0.465	0.410	0.353
130.0	0.54	0.478	0.420	0.364
140.0	0.555	0.487	0.430	0.384
150.0	0.56	0.497	0.440	0.40
160.0	0.57	0.51	0.45	0.40
175.0	0.58	0.52	0.45	0.41

Table A.4: Transmittance for different combinations of materials for various neutron kinetic energies. Combination#1 is Pb, Fe, Air and 7.55 cm thick plastic. Combination#2 is Pb, Fe, Air and 17.55 cm thick plastic. Combination#3 is Pb, Fe, Air, and 27.55 cm thick plastic. Combination#4 is Pb, Fe, Air, and 37.55 cm thick plastic [Table for Fig. 4.3]. These correspond to scintillator bars in planes 1 through 4 in the neutron detector.

Kinetic Energy	**Detection Efficiency (%)**				
(MeV)	Plane 1	Plane 2	Plane 3	Plane 4	Sum of all
20.0	1.534	1.603	1.092	0.007	4.236
30.0	2.604	2.22	1.683	0.787	7.294
40.0	3.237	2.947	2.353	1.116	9.653
50.0	4.018	3.714	3.169	1.801	12.702
60.0	4.749	4.411	3.725	2.379	15.264
70.0	4.972	4.685	4.174	2.866	16.697
80.0	5.024	4.736	4.222	3.054	17.036
90.0	4.974	4.672	4.16	3.129	16.935
100.0	4.921	4.533	4.019	3.059	16.532
110.0	5.017	4.679	4.089	3.238	17.023
120.0	4.951	4.489	4.001	3.058	16.499
130.0	4.932	4.563	4.078	3.157	16.73
140.0	5.052	4.596	4.114	3.291	17.053
150.0	5.04	4.695	4.203	3.492	17.433
160.0	5.056	4.771	4.253	3.39	17.38
175.0	5.239	4.914	4.374	3.589	18.116

Table A.5: The detection efficiency of different planes at various neutron kinetic energies. The last column is the sum of the data of all previous four columns. Note that the detection efficiency is the product of efficiency and transmittance as defined in the text [Table for Fig. 4.4].

Momentum (MeV/c)	**Neutron Detector Efficiency [%]**					
	Simulation		**Experiment**			
			high threshold		low threshold	
	high threshold	low threshold	data	error	data	error
205	0.60	5.12	1.26881	0.0946605		
215	1.16	5.83	1.47837	0.0930946		
225	1.66	6.46	1.7166	0.0952313		
235	2.08	7.10	2.11332	0.099589		
245	2.65	7.81	2.47378	0.105883		
255	3.21	8.44	2.68602	0.112209		
265	3.71	9.08	3.74183	0.1369		
275	4.24	9.57	3.97423	0.156028	9.71	1.0
285	4.91	10.42	4.84183	0.19496		
295	5.54	11.41	4.98196	0.234465		
305	6.25	12.26				
315	6.96	13.18				
325	7.81	14.10			12.5	1.0
341	8.997	15.264				
347.5	9.50	15.72				
369	10.879	16.697				
375	11.2	16.8			16.32	1.93
396	11.843	17.036				
421	12.376	16.935				
445	12.508	16.532				
468	13.14	17.023				
490	13.02	16.499			16.7	2.87597
511	13.33	16.73				
532	13.626	17.053				
552	14.119	17.433				
571	14.218	17.38				
600	14.753	18.116				

Table A.6: Final result for the neutron detector efficiency [Table for Fig. 4.5].

Appendix B

E01-015 Collaboration List

The E01-015 experiment collaborators (in alphabatical order) along with their respective home insititurions are listed below (76 people from 27 different institutions).

B. Anderson[1], K. Aniol[2], J. Annand[3], J. Arrington[4], H. Benaoum[5], F. Benmokhtar[6], P. Bertin[7], W. Bertozzi[8], W. Boeglin[9], J. -P. Chen[10], S.Choi[11], E. Chudakov[10], E. Cisbani[13], B. Craver[14], C. W. de Jager[10], R. Feuerbach[10], S. Frullani[13], F. Garibaldi[13], O. Gayou[8], S. Gilad[8], R. Gilman[6,10], O. Glamazdin[15], J. Gomez[10], O. Hansen[10], D. Higinbotham[10], T. Holmstrom[16], H. Ibrahim[17], R. Igarashi[18], E. Jans[19], X. Jiang[6], Y. Jiang[20], L. Kaufman[21], A. Kelleher[16], A. Kolarkar[22], E. Kuchina[6], G. Kumbartzki[6], J. LeRose[10], R. Lindgren[14], N. Liyanage[14], D. Margaziotis[2], P. Markowitz[9], S. Marrone[13], M. Mazouz[23], R. Michaels[10], B. Moffit[16], P. Monaghan[8], S. nanda[10], C. Perdrisat[16], E. Piasetzky[24], M. Potokar[25], V. Punjabi[26], Y. Qiang[8], J. Reinhold[9], B. Reitz[10], G. Ron[24], A. Saha[10], B. Sawatzky[12], A. Shahinyan[11], R. Shneor[24], S. Sirca[25], K. Slifer[12], P. Solvignon[12], R. Subedi[1], V. Sulkosky[16], N. Thompson, P. Ulmer[17], G. Urciuoli, E. Voutier[23], K. Wang[14], J. Watson[1], L. Weinstein[17], B. Wojtsekhowski[10], S. Wood[10], H. Yao[11], X. Zheng[4], L. Zhu[27]

(The Jefferson Laboratory E01-015 and Hall A Collaborations)

[1]Kent State University, Kent, Ohio 44242, USA

[2]California State University, Los Angeles, Los Angeles, California 90032, USA

[3]University of Glasgow, Glasgow G12 8QQ, Scotland, UK

[4]Argonne National Laboratory, Argonne, Illinois, 60439, USA

[5]Syracuse University, Syracuse, New York 13244, USA

[6]Rutgers, The State University of New Jersey, Piscataway, New Jersey 08855, USA

[7]Universite Blaise Pascal/CNRS-IN2P3, F-63177 Aubi'ere, France

[8]Massachusetts Institute of Technology, Cambridge, Massachusetts 02139, USA

[9]Florida International University, Miami, Florida 33199, USA

[10]Thomas Jefferson National Accelerator Facility, Newport News, Virginia 23606, USA

[11]Yerevan Physics Institute, Yerevan 375036, Armenia

[12]Temple University, Philadelphia, Pennsylvania 19122, USA

[13]INFN, Sezione Sanitá and Istituto Superiore di Sanitá, Laboratorio di Fisica, I-00161 Rome, Italy

[14]University of Virginia, Charlottesville, Virginia 22904, USA

[15] Kharkov Institute of Physics and Technology, Kharkov 310108, Ukraine

[16]College of William and Mary, Williamsburg, Virginia 23187, USA

[17]Old Dominion University, Norfolk, Virginia 23508, USA

[18]Department of Physics and Engineering Physics, University of Saskatchewan, Saskatoon, Saskatchewan, Canada S7N 5E2

[19]Nationaal Instituut voor Kernfysica en Hoge-Energiefysica (NIKHEF)

[20]CCAST (World Laboratory), P.O. Box 8730, Beijing 100080, China

[21]University of Massachusetts Amherst, Amherst, Massachusetts 01003, USA

[22]University of Kentucky, Lexington, Kentucky 40506, USA

[23]Laboratoire de Physique Subatomique et de Cosmologie, 38026 Grenoble, France

[24]Tel Aviv University, Tel Aviv 69978, Israel

[25]Institute "Jozef Stefan", University of Ljubljana, Jamova 39, 1000 Ljubljana, Slovenia

[26] Norfolk State University, Norfolk, Virginia 23504, USA

[27]University of Illinois at Urbana-Champaign, Urbana, Illinois 61801, USA